

University of Innsbruck
Faculty of Mathematics,
Computer Science and Physics
Institute for Experimental Physics



Master's Thesis
submitted in partial fulfillment
of the requirements for the degree of
Master of Science (MSc)

**Frequency comb Raman spectroscopy
for quantum logic**

from
Elyas Mattivi
(Matr.-Nr.: 11908124)

Carried out under the supervision of Dr. Philipp Schindler at the
Quantum Optics and Spectroscopy group

February, 2025

Abstract

Molecular quantum states arise from electronic, vibrational, and rotational energy levels, with rotational states forming distinct energy structures studied in rotational spectroscopy. This technique measures the absorption or emission of radiation as molecules transition between rotational levels, typically using microwave or terahertz radiation. While microwave radiation directly probes these transitions, terahertz radiation uses Raman transitions, involving two lasers with a frequency difference matching the energy gap of the target transition, with a third level far off-resonant. Optical frequency combs, ultrafast lasers primarily used in metrology, can coherently drive such transitions when the energy falls within their bandwidth. The research group where this work was conducted plans to use this system to manipulate rotational states of molecular ions, enabling spectroscopy and molecular error correction experiments.

The state-of-the-art setup of this research group features a linear ion trap with optical access for lasers capable of ablating, ionizing, and cooling trapped calcium-40 ions. It also enables the use of a $4^2S_{1/2} \leftrightarrow 3^2D_{5/2}$ transition as a qubit manifold, along with its readout. Additionally, techniques for generating calcium-based molecules have been implemented. The primary goal of this work was to integrate a commercial optical frequency comb into the setup while implementing self-phase modulation to extend its bandwidth and expanding the range of accessible energy differences for Raman transitions in quantum systems. Additionally, dispersion compensation was applied to bring the comb closer to the Fourier limit, improving the efficiency of Raman transitions.

Proof-of-principle spectroscopy measurements were performed by driving Raman transitions between the $3^2D_{5/2} (m_{5/2} = -1/2)$ and $3^2D_{3/2} (m_{3/2})$ states of a calcium-40 ion, where $m_{3/2}$ was either $-1/2$ or $+3/2$. These transitions were chosen since they have a similar transition frequency as targeted molecular ions. As a result of the performed measurements, the Landé g -factor of the $3^2D_{3/2}$ state was evaluated to be $g_{3/2} = 0.79945(2)$.

The comb system is capable of manipulating the rotational states of molecules such as CaH^+ and CaOH^+ , which will be part of future quantum logic experiments of our group.

Contents

1	Introduction	1
2	Fundamentals of optical frequency combs and light-atom interaction	5
2.1	Optical frequency comb theory	5
2.1.1	Modeling and properties	5
2.1.2	Dispersion	8
2.1.3	Self-phase modulation	13
2.1.4	Generation, stabilization, and applications	18
2.2	Light-atom interaction	20
2.2.1	Calcium-40 ion theory and two-level system	20
2.2.2	Two-photon Raman transition	28
2.2.3	Optical frequency comb Raman transition	31
2.2.4	Ramsey interferometry and spin echo	35
3	Experimental setup and optical frequency comb characterization	40
3.1	Optical setup	40
3.2	Characterization of the optical frequency comb	44
4	Spectroscopy results	49
4.1	Alignment using induced AC-Stark shift	50
4.2	Measurements of Raman transitions and calcium-40 D _{3/2} Landé g-factor	51
4.3	Ramsey interferometry	58
5	Discussion and outlook	60
A	Fourier transform of a pulsed laser	63
B	AC-3 unit repair	65
C	Comparison of Landé g-factor extraction methods	66
D	Additional data	68
D.1	Polarization-dependent spectra	68
D.2	2D Rabi spectroscopy scan	70
D.3	Dispersion measurements	71
	Bibliography	73

Introduction

Quantum computing refers to the harnessing of quantum bits (qubits) as carriers of information to perform computations through quantum superposition and entanglement [1–4]. Once fully developed, this technology is expected to offer significant computational advantages in specific areas compared to classical computers [5–7].

Qubits, the fundamental units of quantum computers, are typically formed from two discrete energy states of a quantum system. These states arise due to energy quantization, meaning the quantum system can only occupy specific states dictated by the Schrödinger equation [8, ch. 2.2.2]. Their behavior can be modeled using the mathematical framework of the Hilbert space. According to the superposition principle, a quantum system can exist in, or populate, a combination of multiple energy states simultaneously [8, ch. 2.2.1]. Population can also be transferred between different states. Such a transition occurs when the quantum system interacts with its environment and absorbs or emits energy, often in the form of photons, causing its population to shift from one state to another. This process, known as driving transitions, enables controlled state manipulation in quantum computing.

Commonly used qubit platforms for quantum computing include atomic ions [9], superconducting circuits [10], NV-centers [11], quantum dots [12], and photons [13]. At the Quantum Optics and Spectroscopy Group [14] at the University of Innsbruck, atomic ions are the most extensively studied platform [15–22], where qubits are encoded in the energy states of their electrons. This work was conducted within QCosmo [23], a subgroup focused on investigating the physics and exploiting the computational capabilities of molecular ions rather than atomic ions [24–26].

The Hilbert space of molecular ions is significantly larger than that of atomic ions due to additional spatial degrees of freedom, three for each atom in the molecule. These extra degrees of freedom give rise to complex quantized energy structures beyond electronic states due to molecular vibrations and rotations [27, ch. 10.4]. This complexity could make molecules a promising platform for more robust qubits, as qubit state information can be redundantly stored in other states to enhance protection against noise and errors. However, this same complexity has made molecular ions less studied in quantum computing compared to atomic ions [28]. Consequently, many experimental techniques for controlling molecular ions are still in development.

Despite the challenges, significant progress has been made in various areas. Long storage times of quantum information have been demonstrated [29, 30], and the technique of quantum logic spectroscopy has been applied to molecules [31, 32], where quantum logic

spectroscopy refers to the mapping of quantum information from a molecular ion to a fully controllable atomic ion via their shared quantized motion, which is caused by a trapping potential and their Coulomb repulsion. Additionally, techniques for preparing molecules in pure energy states have been developed [33], entanglement (a quantum correlation linking particle states [8, ch. 2.2.8]) has been demonstrated [34–36], and rotational quantum states have been tracked over long periods of time in thermal environments [37]. Recent theoretical work includes strategies for robust qubit encoding in molecular rotational states [38], as well as methods to protect such encoding against spontaneous photon emission and black-body radiation errors in specific molecules [39]. These works enabled a proposal for the experimental implementation of molecular quantum error correction [26].

QCosmo aims to build on this past research by developing techniques to prepare, control, and characterize polyatomic molecules at the quantum level. A key goal is achieving precise control over rotational energy states, enabling controlled population transfer. Rotational states are distinguished by their energy magnitudes, which differ from vibrational and electronic states. These energies correspond to frequencies typically ranging from 10 GHz to 10 THz [40, 41]. One approach to transfer population between rotational states is to drive the transition directly using a free-space electromagnetic field whose frequency is resonant with the transition frequency [42]. However, such fields are hard to integrate as they are typically in the microwave and not in the optical frequency range.

Optical fields can also drive such transitions using Raman transitions [43]. The basic principle is based on a three-state quantum system and two single-frequency lasers whose frequency difference matches the energy gap between two target states. For effective population transfer, the lasers must remain off-resonant with respect to the third state. This ensures population transfer between the first two states without populating the third. However, this approach lacks flexibility. Lasers engineered for a specific Raman transition between two rotational states may not be suitable for other rotational transitions, as their frequency difference may no longer match the original energy gap.

A more flexible approach to this problem is provided by optical frequency combs, a type of pulsed laser with a broader spectral bandwidth than single-frequency lasers. Their working principle will be discussed in this thesis, but the core idea is that they can be viewed as a superposition of many single-frequency lasers with distinct, regularly spaced center frequencies. To drive a transition with a specific energy difference, the corresponding frequency must fall within the comb’s bandwidth so that two of its single-frequency components can induce a Raman transition. Previous work has demonstrated the use of optical frequency combs for driving transitions between D -states in calcium-40 ions [44] and rotational transitions in calcium monohydride ions (CaH^+) [45].

One of the goals of this work was to integrate a commercial optical frequency comb into the QCosmo setup to enable future experiments to control the rotational energy states of molecular ions such as CaH^+ and CaOH^+ . Before the experimental phase of this work began, the QCosmo setup consisted of the following components: A linear Paul trap [46] designed to confine calcium-40 ions and other molecules within a harmonic potential using radio-frequency and direct-current electrodes [47]. The trap is located in an ultra-high vacuum chamber (10^{-10} mBar) to minimize collisions of the ions with

background gas. Additionally, several single-frequency lasers are aligned to the trap, serving distinct functions:

- A laser with 532 nm center frequency: Ablates calcium-40 from a target into the vacuum [48].
- 422 nm and 375 nm: Ionize the resulting atomic cloud by removing one electron in a two photon process [49].
- 397 nm and 866 nm: Perform Doppler cooling, bringing trapped ions close to Doppler limited temperature [50].
- 729 nm and 854 nm: Enable resolved-sideband cooling, driving the ions toward their motional ground state within the harmonic potential [51–53].

Once the desired number of ions is trapped, they can be detected using either a camera or a photomultiplier tube by observing fluorescence from a cycling transition within the ions' electronic states [54]. A cycling transition refers to an excitation that consistently decays back to its original state via spontaneous emission. This process enables state detection by distinguishing whether the ions are in the $4^2S_{1/2}$ state (observed fluorescence due to repeated spontaneous emission) or in a different state (no fluorescence). Additionally, control over a qubit transition has been achieved with high-fidelity readout and long coherence times. The qubit states are encoded in the $4^2S_{1/2}$ and $3^2D_{5/2}$ states and manipulated using a 729 nm single-frequency laser.

This work builds on the existing setup and demonstrates the integration of a commercial optical frequency comb. For efficient population transfer, the drivable energy differences of a quantum state must fall within the comb's spectral bandwidth. As such, it is beneficial to have as high of a bandwidth as possible. To extend this bandwidth, a nonlinear optical effect known as self-phase modulation was used, where the nonlinearity arises from a material's refractive index depending on the laser's intensity. However, this process introduces spectral phase variations across the bandwidth, a phenomenon known as dispersion. Dispersion can arise due to a material's refractive index depending on the laser's wavelength. Due to destructive interference between different spectral components, dispersion reduces the efficiency of driving transitions. To mitigate this, this work also implements so-called dispersion compensation.

The theoretical framework for describing optical frequency combs, dispersion, and self-phase modulation is presented in chapter 2. This chapter also covers relevant light-atom interactions between the optical frequency comb and a single trapped calcium-40 ion, with a focus on Raman transitions and Ramsey interferometry. Chapter 3 details the experimental implementation of these concepts in an optical setup. Specifically, it describes the generation of the optical frequency comb, power amplification, self-phase modulation, dispersion compensation, and the alignment of the light to ensure spatial overlap with a trapped ion. It also characterizes the temporal and spectral amplitudes and phases of the optical frequency comb at various stages of the optical setup.

Using this optical frequency comb setup, this work demonstrates coherent state manipulation of a calcium-40 ion via comb Raman transitions between the electronic states

$3^2D_{5/2} (m_{5/2} = -1/2)$ and $3^2D_{3/2} (m_{3/2})$, where $m_{3/2}$ was either $-1/2$ or $+3/2$. Additionally, the collected data was used to estimate the Landé g -factor of the $3^2D_{3/2}$ state with higher precision than its theoretical value. It was estimated by constructing a likelihood function and extracting the most likely value. This value was measured as no known publication reported on this Landé g -factor till now. The extracted result, stated in equation (4.2), has a relative precision uncertainty of $2.5 \cdot 10^{-5}$. However, systematic errors have not been investigated. These results are presented in chapter 4.

Finally, chapter 5 concludes with a comparison of the results from this work with similar studies from other groups and suggests potential improvements and expansions to the optical frequency comb setup. It also provides an outlook on how this setup will be used in the future to study rotational transitions in molecular ions.

Fundamentals of optical frequency combs and light-atom interaction

This chapter focuses on establishing the foundational principles that support this work. It will cover the theoretical description of optical frequency combs (section 2.1.1), how they are affected by dispersion (section 2.1.2), and how they are influenced by self-phase modulation (section 2.1.3). A brief overview of how optical frequency combs are generated, stabilized, and their applications is presented (section 2.1.4). Moreover, the interaction of light and matter is discussed by first introducing the calcium-40 ion and modeling it as a two-level system (section 2.2.1). A relevant generalization for this work is the three-level system together with continuous-wave Raman transitions (section 2.2.2) which can ultimately be expanded to optical frequency comb Raman transitions with the ion (section 2.2.3). Finally, Ramsey and spin echo techniques to characterize certain types of noise in the system are also discussed (section 2.2.4).

2.1 Optical frequency comb theory

Optical frequency combs are a type of ultrafast pulsed laser that provide a comb-like structure in the frequency domain. They have two distinct properties that differentiate them from ultrafast pulsed lasers: the stabilization of the repetition rate ω_{rep} and the carrier-envelope offset frequency ω_{CEO} . Optical frequency combs have been extensively reviewed (see, for example, [55–57]) as they are an important tool for today’s technologies, enabling, for example, the most precise measurements of the second [58, 59]. In this section, it is explained how ω_{rep} and ω_{CEO} emerge by modeling an optical frequency comb in time and frequency domain. Further, we explore what roles the optical phenomenon of dispersion and the nonlinear self-phase modulation effect play. The section concludes with a more practical aspect of optical frequency combs: how they are generated, what their applications are, and how ω_{rep} and ω_{CEO} are stabilized.

2.1.1 Modeling and properties

To understand how optical frequency combs work and how they interact with certain systems such as a trapped ion, it is useful to model them mathematically and derive their properties from there. We will look at a temporal and spectral description of an optical frequency comb while introducing key quantities, such as the repetition rate and the carrier-envelope offset frequency.

2.1 Optical frequency comb theory

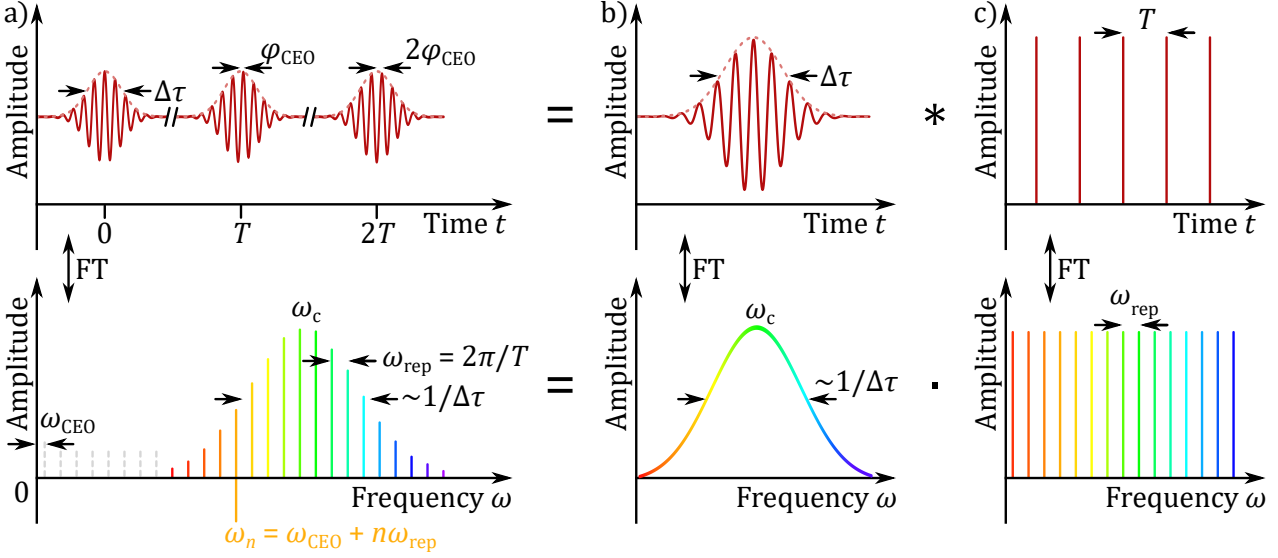


Figure 2.1: **Temporal and spectral representation of an optical frequency comb.**

The top half represents the time domain of an optical frequency comb and the bottom half the frequency domain. They are connected via the Fourier transform (FT). In the time domain, convolving (denoted as $*$, see appendix A) a single pulse (b) with a temporal Dirac comb (c) results in a pulsetrain (a). In the frequency domain, the typical spectral structure of an optical frequency comb (a) is found by multiplying a spectral envelope (b) by a spectral Dirac comb (c). The drawing is based on equations (2.1) and (2.2).

The top part of figure 2.1a shows the electric field of a pulsetrain in the time domain. It can be modeled using an envelope function $E_{\text{single}}(t)$, which repeats with period T , multiplied by a waveform function with amplitude $\cos(\phi(t))$. The electric field can be modeled by

$$E(t) = \cos(\phi(t)) \sum_{n=-\infty}^{\infty} E_{\text{single}}(t - nT). \quad (2.1)$$

We can simplify the analysis of this model by assuming a single-frequency laser such that its temporal phase term takes the form of $\phi(t) = \omega_c t - \phi_0$, where ω_c represents the carrier frequency of an optical laser pulse. This assumption is not strictly necessary but enables an intuitive derivation of the properties of the optical frequency comb. The effects of a general $\phi(t)$ will be discussed qualitatively towards the end of this section.

To extract the relevant properties of the model of the optical frequency comb, we can analyze it in the Fourier domain. Thus, we can apply the Fourier transform \mathcal{F} on this expression. The derivation of the Fourier transform $\tilde{E}(\omega) := \mathcal{F}\{E(t)\}(\omega)$ specific to the field model described above can be found in Appendix A. Ignoring negative frequencies as they do not provide additional information for real temporal fields, the frequency domain representation of the electric field model is

$$\tilde{E}(\omega) \propto \mathcal{F}\{E_{\text{single}}(t)\}(\omega - \omega_c) \text{III}_{2\pi/T}(\omega - \omega_c). \quad (2.2)$$

An example of this peculiar structure is depicted in the bottom part of figure 2.1a.

The symbol III is pronounced “sha” and represents the Dirac comb function, it is defined in terms of Dirac delta distributions $\delta(\omega)$ as

$$\text{III}_{2\pi/T}(\omega) := \sum_{n=-\infty}^{\infty} \delta\left(\omega - n\frac{2\pi}{T}\right)$$

and generates a regular comb-like array of delta functions. This function and its Fourier transform is illustrated in figure 2.1c.

The frequency domain of the electric field model describing a frequency comb has essentially two parts: (i) The global spectral envelope, which is defined by the Fourier transform of the single pulse envelope. This spectral envelope is centered around the carrier frequency ω_c and spans over all non-zero spectral components; thus it is called global. In this derivation, the width of the global spectral envelope is related to the width of the temporal envelope $\Delta\tau$ by being proportional to $1/\Delta\tau$. The proportionality factor is given by a quantity called time–bandwidth product [60]. This situation is depicted in figure 2.1b. (ii) The Dirac comb generates periodic peaks, also known as comb teeth, with separated by a distance called the repetition rate. The value of the repetition rate is

$$\omega_{\text{rep}} := \frac{2\pi}{T}.$$

This implies that such an electric field is everywhere zero in the Fourier domain except at the location of the comb teeth.

There will generally be an offset between the lowest frequency comb tooth and the absolute zero frequency. This is due to the fact that the Dirac comb in equation (2.2) is centered around the carrier frequency ω_c , and there does not necessarily exist an integer N such that $\omega_c - N\omega_{\text{rep}} = 0$. This offset is quantified by the carrier-envelope offset frequency ω_{CEO} or the carrier-envelope phase φ_{CEO} defined as

$$\begin{aligned} \omega_{\text{CEO}} &:= \omega_c \bmod \omega_{\text{rep}} & \text{and} & & \varphi_{\text{CEO}} &= 2\pi \frac{\omega_c \bmod \omega_{\text{rep}}}{\omega_{\text{rep}}} \\ &\Rightarrow \omega_{\text{CEO}} &= \omega_{\text{rep}} \frac{\varphi_{\text{CEO}}}{2\pi}. \end{aligned}$$

Using this offset we can localize the n -th comb tooth ω_n in the modeled electric field with respect to the origin via

$$\omega_n = \omega_{\text{CEO}} + n\omega_{\text{rep}}.$$

In the context of practical implementations of optical frequency combs, this equation only holds if both the repetition rate ω_{rep} and the carrier-envelope offset frequency ω_{CEO} are measured to be accurate and precise over time, typically with precision uncertainties on the order of mHz and Hz, respectively. The differences between a generic ultrafast laser and an optical frequency comb are exactly these highly stabilized values of ω_{rep} and ω_{CEO} . The way these are commonly stabilized is discussed in section 2.1.4.

The presented derivation assumed a linear temporal phase function $\phi(t) = \omega_c t - \phi_0$. We talk about a chirped waveform if its temporal phase function $\phi(t)$ is described by additional

2.1 Optical frequency comb theory

higher-order terms $\mathcal{O}(t^2)$ (chirp as in bird sounds, mimicking changing frequencies over time). A phase with a highest-order term of t^2 is said to be linearly chirped due to the instantaneous frequency $d\phi/dt$ being linear. If we allow for a general temporal phase term $\cos(\phi(t))$ in this derivation, then the relation of equation (2.2) becomes more complicated. This phase term would then encode additional spectral phase and global spectral amplitude information. Such a general spectral field takes the following form:

$$\tilde{E}(\omega) = \mathcal{F}\{\cos(\phi(t))\}(\omega) * (\mathcal{F}\{E_{\text{single}}(t)\}(\omega) \text{III}_{\omega_{\text{rep}}}(\omega)).$$

If we start from a Fourier description, we can reformulate this last equation by collecting amplitude, phase, and comb terms. We can then describe it as

$$\tilde{E}(\omega) = \tilde{E}_{\text{env}}(\omega - \omega_c) \text{III}_{\omega_{\text{rep}}}(\omega - \omega_{\text{CEO}}) e^{-i\varphi(\omega)}, \quad (2.3)$$

where \tilde{E}_{env} is a real valued envelope function centered around zero, the spectral phase term $\varphi(\omega)$ captures real and imaginary oscillations, and the Dirac comb is equal to $\text{III}_{\omega_{\text{rep}}}(\omega - \omega_{\text{CEO}}) = \text{III}_{\omega_{\text{rep}}}(\omega - \omega_c)$ due to its infinite extension and $\omega_{\text{CEO}} = \omega_c \bmod \omega_{\text{rep}}$. It should be noted that only positive frequencies are shown here, as the Dirac comb would be reflected around zero for negative frequencies. We can rewrite this expression by expanding the Dirac comb

$$\begin{aligned} \tilde{E}(\omega) &= \sum_{n=0}^{\infty} \tilde{E}_{\text{env}}(\omega - \omega_c) \delta(\omega - (\omega_{\text{CEO}} + n\omega_{\text{rep}})) e^{-i\varphi(\omega)} \\ &= \sum_{n=0}^{\infty} \tilde{E}_{\text{env},n} \delta(\omega - \omega_n) e^{-i\varphi_n}, \end{aligned}$$

where $\omega_n = \omega_{\text{CEO}} + n\omega_{\text{rep}}$ are the frequencies of the comb teeth, the amplitudes of the comb teeth are $\tilde{E}_{\text{env},n} = \tilde{E}_{\text{env}}(\omega_n - \omega_c)$, and $\varphi_n = \varphi(\omega_n)$ describe their phases. Taking the inverse Fourier transform of the previous expression (including negative frequencies) yields

$$\begin{aligned} E(t) &= \mathcal{F}^{-1}\{\tilde{E}(\omega)\}(t) \\ &= \sqrt{\frac{2}{\pi}} \sum_{n=0}^{\infty} \tilde{E}_{\text{env},n} \cos(\omega_n t - \varphi_n). \end{aligned} \quad (2.4)$$

This form leads to the interpretation that an optical frequency comb can be viewed as a superposition of single-frequency lasers, each with different amplitudes and phases but with regularly spaced frequencies. This equation also shows that temporal phases equate to spectral phases.

2.1.2 Dispersion

Optical media have a property called dispersion, which makes the phase velocity and group velocity of light passing through the medium frequency dependent. Such dispersion affects the temporal envelope of ultrafast lasers, can introduce temporal chirp (a non-linear temporal phase), and generates different spectral phases at different parts of the spectrum

[61, ch. 4]. These effects impact the performance of ultrafast lasers and could render them inefficient for intended applications. For example, in the experimental system of this work, we rely on the phase relation between two different spectral components for driving transitions on the calcium-40 ion. If this relation introduces destructive interference, then the effectiveness of driving such transitions is reduced. We will cover how to model and calculate dispersion by Taylor-expanding the spectral phase into different orders, show the effect of dominant low-order dispersion terms, and discuss strategies of how to compensate for unwanted dispersion.

Dispersion emerges when we analyze the spectral description of an optical frequency comb derived in equation (2.3). There, the spectral phase $\varphi(\omega)$ is responsible for the physical effects of dispersion. The spectral phase can be a complicated function depending on the details of the Fourier transform of the temporal single pulse envelope and the temporal phase term. It is common to express the spectral phase $\varphi(\omega)$ in terms of a Taylor expansion of the frequency variable around the carrier frequency

$$\varphi(\omega) = \sum_{j=0}^{\infty} \frac{D_j}{j!} (\omega - \omega_c)^j, \quad D_j = \frac{d^j \varphi}{d\omega^j}(\omega_c). \quad (2.5)$$

The coefficients of the expansion are called dispersion coefficients and have dedicated names and units :

$$\begin{aligned} D_0 : & \quad \text{Phase delay}, & [D_0] &= \text{rad}, \\ D_1 : & \quad \text{Group delay (GD)}, & [D_1] &= \text{fs}, \\ D_2 : & \quad \text{Group delay dispersion (GDD)}, & [D_2] &= \frac{\text{fs}^2}{\text{rad}}, \\ D_3 : & \quad \text{Third-order dispersion (TOD)}, & [D_3] &= \frac{\text{fs}^3}{\text{rad}^2}, \\ D_4 : & \quad \dots \end{aligned}$$

The time units of the dispersion coefficients are determined by the typical duration of the pulse, which is usually given in fs or ps. The radian angle units (rad) are often omitted, but it is important to specify them for clarity.

The phase delay D_0 generates a common temporal phase shift and relates to the propagation of the carrier phase itself. The group delay D_1 describes a temporal shift of the single pulse envelope function with respect to the origin. The group delay dispersion D_2 is responsible for the broadening of the temporal envelope and introducing a linear chirp in the temporal phase. Higher-order terms deform the temporal pulse envelope and phase non-trivially, like generating post- and pre-pulses. While D_0 only induces a phase shift, other even-order dispersion values affect the temporal shape symmetrically and introduce a chirp on the temporal phase, while odd-order values affect the shape asymmetrically and introduce no chirp. Examples of zero-, second-, and third-order dispersion on a Gaussian-shaped pulse are shown in figure 2.2. A light pulse traveling through a material with positive group velocity dispersion results in a shape as shown in the middle red plot

2.1 Optical frequency comb theory

in figure 2.2. While propagating through the medium, blue light is slowed more than red light due to the implied higher refractive index. This results in the chirp visible at the waveform of the temporal pulse. Based on this discussion, dispersion is said to arise when the temporal envelope is altered. This happens when the terms D_j for $j \geq 2$ are non-zero. Otherwise, a pulsed light field is said to be transform- or Fourier-limited.

For a more practical discussion: As we will see in section 2.2.3, dispersion influences the Raman Rabi rates in a coherent interaction between an ion and the optical frequency comb via Raman transitions due to interference effects. A laser phase shift induced by D_0 does not affect the interaction's effectiveness, while D_1 merely introduces a timing delay of the pulse, which also has no impact in a single-beam interaction. However, higher-order terms reduce the interaction's effectiveness.

Information about dispersion coefficients is often stated with a different convention. There, higher-order dispersion coefficients follow a different definition along with having different units. They are based on derivatives of the spectral phase with respect to the wavelength λ instead of the angular frequency $\omega = \omega(\lambda) = 2\pi c/\lambda$, where c is the speed of light in vacuum. The definitions and units are

$$D_j^\lambda = \left. \frac{d^{j-1}}{d\lambda^{j-1}} \frac{d\varphi}{d\omega}(\omega(\lambda)) \right|_{\lambda=\lambda_c} \quad [D_j^\lambda] = \frac{\text{ps}}{\text{nm}^{j-1}} \quad \text{for } j \geq 2,$$

where $\lambda_c = 2\pi c/\omega_c$. For the special case of $j = 2$ and $j = 3$ we get

$$D_2^\lambda = \left(-\frac{2\pi c}{\lambda_c^2} \right) D_2 \quad \text{and} \quad D_3^\lambda = \left(-\frac{2\pi c}{\lambda_c^2} \right)^2 \left(\frac{\lambda_c}{\pi c} D_2 + D_3 \right).$$

After having discussed how to calculate dispersion using two different conventions based on a field's spectral information, to control dispersion it is important to understand how dispersion accumulates when the field interacts with its environment. Dispersion is a property of a dynamic field, but such a field can accumulate more dispersion as it travels through a material or interacts with optical elements such as mirrors or gratings due to the objects' influence on the field's phase. If a field has an initial dispersion coefficient of $D_{j,i}$ and passes through a medium for which a corresponding material dispersion coefficient of $D_{j,m}$ can be associated (as we will see, $D_{j,m}$ is then a material property arising from the refractive index), then the field after passing through the medium has a final coefficient of

$$D_{j,f} = D_{j,i} + D_{j,m}.$$

Thus as a light pulse travels through any optical setup it can potentially accumulate spectral phase. In the context of dispersion arising from propagation through dispersive media we define normal dispersion to be $D_2 > 0$ ($D_2^\lambda < 0$) and anomalous dispersion to be $D_2 < 0$ ($D_2^\lambda > 0$) [61, ch. 4.1.2]. The following discussion covers how to calculate the material dispersion coefficients $D_{j,m}$ for solid media and briefly touches on how to calculate it for free-space optical elements such as mirrors and gratings.

If D_j represents the dispersion a field acquires while traveling through a material of

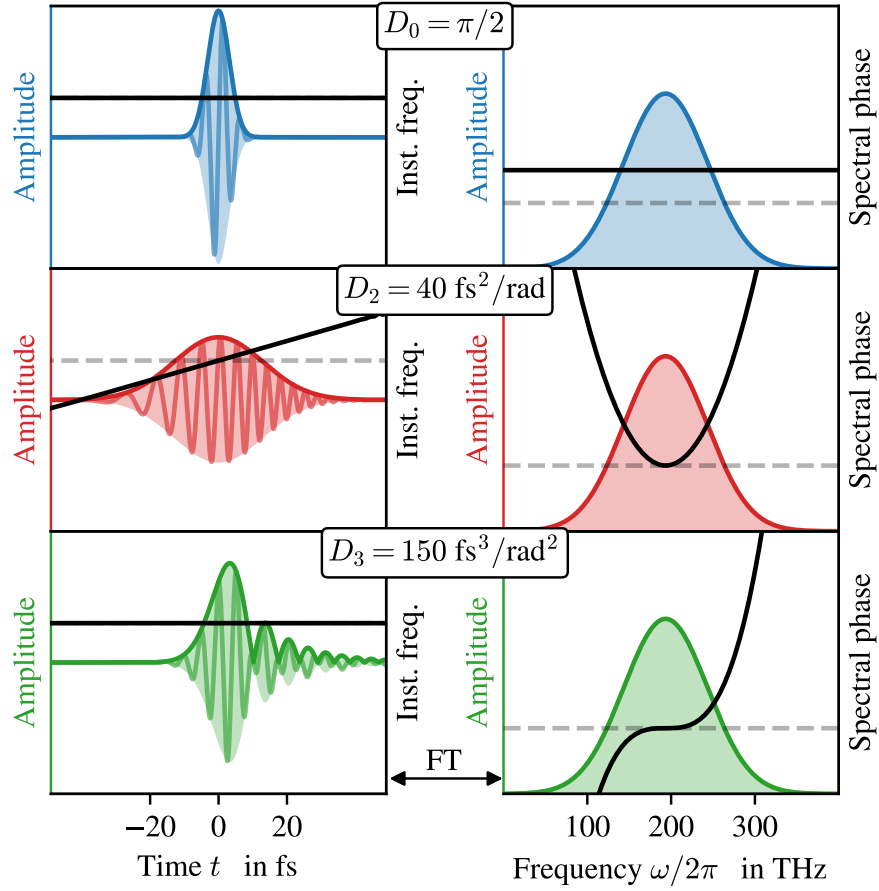


Figure 2.2: **Effects of different dispersion orders on a short pulse.** For this figure the spectral phase of a Fourier-limited Gaussian-shaped pulse (electric field) was altered to include only phase delay D_0 (top, blue), group delay dispersion D_2 (center, red), and only third-order dispersion D_3 (bottom, green). The dashed lines represent the carrier frequency for the instantaneous frequency (inst. freq.) graphs in the temporal plots and zero phase for the spectral plots. The colored parts of the temporal plots show both the amplitude envelope of the electric field and the real part of the electric field (waveform) to visualize frequency chirp. The drawn graphs are based on equations (2.3) and (2.5). FT: Fourier transformation.

length L , then the dispersion per unit length associated with the material is defined as

$$\beta_j = \frac{D_j}{L}, \quad [\beta_j] = \frac{\text{fs}^j}{\text{mm rad}^{j-1}},$$

or

$$\beta_j^\lambda = \frac{D_j^\lambda}{L}, \quad [\beta_j^\lambda] = \frac{\text{ps}}{\text{km nm}^{j-1}}.$$

The dispersion coefficients per unit length in a material is determined by the refractive index $n(\omega)$. To understand how, it is useful to split the spectral phase φ in a angular

2.1 Optical frequency comb theory

wavenumber term k multiplied by the material length L ,

$$\varphi(\omega) = k(\omega)L.$$

Under certain assumptions, especially linear, homogeneous, and isotropic materials, the wavenumber follows the dispersion relation [62, ch. 5.5]

$$k(\omega) = \beta(\omega) + i\alpha(\omega) = \frac{\omega}{c} \sqrt{\epsilon(\omega)}, \quad (2.6)$$

where ϵ is the relative permittivity, or dielectric constant. The parameter α quantifies absorption inside a medium and relates to the extinction coefficient, and the parameter β relates to the refractive index n via

$$\beta(\omega) = \frac{\omega}{c} \operatorname{Re} \left\{ \sqrt{\epsilon(\omega)} \right\} = \frac{\omega}{c} n(\omega).$$

The dispersion coefficients per unit length β_j are then the Taylor series expansion coefficients of $\beta(\omega)$, assuming negligible $\alpha(\omega)$ typical for transparent media. Using the so-called group refractive index

$$n_g(\omega) = \frac{d}{d\omega}(\omega n(\omega)) = n(\omega) + \omega \frac{dn}{d\omega}(\omega)$$

and the phase and group velocities respectively defined as

$$v_{\text{ph}}(\omega) = \frac{c}{n(\omega)}, \quad v_g(\omega) = \frac{c}{n_g(\omega)},$$

we can calculate the dispersion coefficients per unit length via

$$\begin{aligned} \beta_0 &= \frac{\omega_c}{v_{\text{ph}}(\omega_c)}, \\ \beta_1 &= \frac{1}{v_g(\omega_c)}, \\ \beta_j &= \frac{d^{j-1}}{d\omega^{j-1}} \left(\frac{1}{v_g(\omega)} \right) \Big|_{\omega=\omega_c} \quad \text{or} \quad \beta_j^\lambda = \frac{d^{j-1}}{d\lambda^{j-1}} \left(\frac{1}{v_g(\omega(\lambda))} \right) \Big|_{\lambda=\lambda_c} \quad \text{for } j \geq 2. \end{aligned}$$

The term β_2 is named group velocity dispersion (GVD), the term β_2^λ is often referred to as a dispersion parameter, and β_3^λ is called the dispersion slope.

This last part illustrated how to calculate dispersion coefficients D_j for light fields that propagate through materials. However, dispersion is also introduced through dispersive optical elements, such as mirrors and grating pairs (a pair of gratings which transmit the first order beam parallel to the incoming beam often used for pulse compression [61, ch. 4.3]). Dispersion can be introduced by mirrors, especially those with multiple layers, such as Bragg mirrors, due to the multiple reflecting interfaces and phase shifts accumulated when partially traveling through the layers. Their dispersion can, for example, be evaluated using the transfer-matrix method [63] by comparing the spectral phase φ_r of the reflected beam with the spectral phase φ_{in} of the incident beam. The added phase is then $\varphi_{\text{add}} = \varphi_r - \varphi_{\text{in}}$. For optical elements similar in concept to grating pairs, we

can track the path length difference $\Delta L(\omega - \omega_c)$ that different frequencies travel through compared to the carrier frequency. Then the added spectral phase is $\varphi_{\text{add}} = 2\pi\Delta L/\lambda$ plus other potential contributions, such as grating surface effects. In both cases, we can then derive the accumulated dispersion coefficients from the added spectral phase φ_{add} using equation (2.5). Typical group delay dispersion D_2 values for regular Bragg mirrors can be as low as 0.1 fs^2 , while the D_2 induced by a grating pair can be adjusted through the system parameters but can typically be set between -1000 fs^2 and $-100'000 \text{ fs}^2$.

From this discussion, it becomes clear that we can design optical systems with which we can manipulate the dispersion coefficients of our optical frequency comb. Dispersion coefficients can be either positive or negative and can be tailored to shape a light field with a specific amount of dispersion. In this work, we approximately compensate for any dispersion within the optical frequency comb to maximize the Raman Rabi rates (see section 2.2.3). Examples of optical systems that are used in our setup to control the dispersion coefficients are normal optical fibers, dispersion-compensating optical fibers [64], chirped fiber Bragg gratings (CFBG) [65], and chirped volume Bragg gratings (CVBG) [66]. Other elements that could be used are transparent media [61, ch. 4.1.2], grating pairs [61, ch. 4.3], prism pairs [61, ch. 4.4], chirped mirrors [61, ch. 4.6.3], and time delay stages [67, 68].

An important example for dispersion control is a technique called chirped pulse amplification [69], where non-zero group delay dispersion is introduced on purpose. If we want to amplify an ultrafast laser directly, the problem arises that the gain medium inside the amplifier is easily damaged due to the high peak intensities of such a laser compared to continuous-wave lasers. In chirped pulse amplification, a controlled amount of group delay dispersion D_2 is introduced to achieve a longer pulse length and thus a lower peak intensity. This allows the amplifier to safely increase the power of the laser. After amplification, an inverse group delay dispersion of $-D_2$ brings the ultrafast laser close to its original pulse length. Typical values for D_2 for femtosecond lasers and watt-level power are on the order of 0.1 to 10 ps^2 .

The relationship between the dispersion coefficients and the spectral bandwidth determines whether or not dispersion in the optical frequency comb is significant and whether or not it can be regarded as Fourier-limited. Additionally, appropriately comparing the relative magnitudes between different dispersion coefficients can tell us which of the terms is dominant. Such comparisons can be performed by considering the spectral bandwidth $\Delta\omega$ using $(\Delta\omega/2)^j D_j/j!$, which essentially is a comparison between terms in a polynomial. For example, to determine if the group delay dispersion in the light field is significant, compare $(\Delta\omega/2)^2 D_2/2!$ to 1. To assess if the group delay dispersion dominates over third-order dispersion, compare $(\Delta\omega/2)^2 D_2/2!$ to $(\Delta\omega/2)^3 D_3/3!$. Commonly, a treatment of the group delay dispersion D_2 is sufficient.

2.1.3 Self-phase modulation

Dispersion is a linear effect as it arises from the frequency-dependent refractive index and acts linearly on the electric field, meaning each frequency component propagates independently without mixing. In contrast, nonlinear optical effects introduce intensity-

2.1 Optical frequency comb theory

dependent changes, leading to spectral broadening and frequency mixing, with self-phase modulation (SPM) being one of the most important among them. An interesting duality between dispersion and SPM is the following: Dispersion control techniques can be used to manipulate the spectral phase of a pulsed light field to change its temporal envelope while leaving the spectral envelope unchanged. On the other hand, SPM can be used to manipulate the temporal phase of a pulsed light field while leaving its temporal envelope unchanged, thereby changing its spectral envelope [70]. Combining dispersion control and SPM allows us to broaden the spectral bandwidth using SPM and cancel out accumulated dispersion using dispersion compensation methods. This leads to the creation of a Fourier-limited pulse with shorter temporal length and a larger bandwidth. This method is beneficial in our applications, as increasing the bandwidth of the optical frequency comb will allow us to drive higher-energy Raman transitions in qubit systems, see section 2.2.3. This section will cover how to model SPM and model its effects.

Self-phase modulation is a phenomenon that arises from the intensity dependence of the refractive index of a material due to the optical Kerr effect [71, ch. 6.2.2]. The refractive index is typically modeled as

$$n(I) = n_0 + n_2 I,$$

where I is the intensity of the light field, the term $n_0 = n_0(\omega)$ is the linear refractive index, and n_2 is the second-order nonlinear refractive index of the medium. The intensity is defined according to the temporal electric field E as

$$I(t, z) = |E(t, z)|^2, \quad [E] = \sqrt{\frac{\text{W}}{\text{m}^2}},$$

where in this section the electric field E is modeled to have units of root intensity.

In practice, the second-order nonlinear refractive index n_2 is often expressed in terms of the nonlinear coefficient, or Kerr-nonlinearity coefficient, γ , but can also be evaluated from the third-order nonlinear susceptibility $\chi^{(3)}$ of the material [72]. The relations defining these connections follow

$$n_2 = \gamma A_{\text{eff}} \frac{c}{\omega_c} = \frac{3 \text{Re} \{ \chi^{(3)} \}}{8 n_0(\omega_c)},$$

$$[n_2] = \frac{\text{m}^2}{\text{W}}, \quad [\gamma] = \frac{1}{\text{W m}}, \quad [\chi^{(3)}] = \frac{\text{m}^2}{\text{W}},$$

where ω_c is the carrier angular frequency, the speed of light in vacuum is c , and A_{eff} is the effective mode area. The nonlinear coefficient γ accounts for both the nonlinear refractive index and the effective mode area of the light field. In our case, the latter is connected to the effective area of single-mode fibers, which are commonly used to generate SPM.

A theoretical description of self-phase modulation can be done in either time- or frequency-domain. Numerically, a frequency description is more convenient as dispersion effects can be summarized with only one term. For this we need the Fourier transform of the temporal pulsed field

$$\tilde{E}(\omega, z) = \mathcal{F}_+ \{ E(t, z) \}(\omega),$$

where

$$\mathcal{F}_+\{A(t)\}(\omega) = (1 + \text{sgn}(\omega)) \frac{1}{2t_{\max}} \frac{1}{\sqrt{2\pi}} \int_{-t_{\max}}^{t_{\max}} A(t) e^{-i\omega t} dt,$$

with $\text{sgn}(\pm|\omega|) = \pm 1$, is unit-preserving ($[E] = [\tilde{E}]$) and eliminates negative frequencies. If an inverse Fourier transform matching equation (A.1) is applied to this spectral field, then a so-called analytic temporal field $E^A = \mathcal{F}^{-1}\{\tilde{E}\}$, which has the special property $E = \text{Re}\{E^A\}$, is retrieved (see Hilbert transform [73, ch. 4.3.7]). The endpoints of the integral allow for numerical calculations with finite summation terms. The endpoints can be motivated by considering a single pulse of a pulsetrain with repetition rate ω_{rep} . Since the pulse train is periodic, we set the endpoints to be $2t_{\max} = 2\pi/\omega_{\text{rep}}$ to match the time period of the repetition.

The here assumed differential equation describing the propagation through a nonlinear medium takes the form [74]

$$i \frac{\partial \tilde{E}}{\partial z}(\omega, z) + k(\omega) \tilde{E}(\omega, z) + n_2 \frac{\omega}{c} \mathcal{F}_+\{|E(t, z)|^2 E(t, z)\}(\omega) = 0 \quad (2.7)$$

and is called the simplified forward model for an analytic signal. ‘‘Simplified’’ indicates an approximate version of a more complex model (in fact, it is derived from a more general nonlinear wave equation), ‘‘forward model’’ means it describes the evolution of a signal as it propagates in time, and ‘‘analytic signal’’ refers to the propagation of a complex-valued representation E^A of a real signal E used to separate positive and negative frequency components. The wavenumber $k(\omega)$ in the equation is the same as introduced in equation (2.6) and contains all dispersion effects. The third term models SPM.

To get a feeling on the effects of SPM, it is useful to disregard dispersion effects ($n(\omega) = 1, \Rightarrow k(\omega) = \omega/c$), approximate $\omega \approx \omega_c$, and perform an analysis in the time domain. By applying the inverse Fourier transform \mathcal{F}^{-1} on equation (2.7), we retrieve

$$i \frac{\partial E^A}{\partial z}(t, z) + \frac{\omega_c}{c} E^A(t, z) + n_2 \frac{\omega_c}{c} |E^A(t, z)|^2 E^A(t, z) = 0. \quad (2.8)$$

Separating the temporal field into amplitude and phase by $E^A = \sqrt{I} e^{-i\phi}$, inserting this into the differential equation (2.8), and separating the real and imaginary parts results in

$$\frac{\partial I}{\partial z}(t, z) = 0, \quad \frac{\partial \phi}{\partial z}(t, z) = -\frac{\omega_c}{c} (1 + n_2 I(t, z)).$$

Thus, from the first equation we can conclude that for pure SPM the field intensity $I = I(t)$ is invariant under propagation in the z direction. From the second equation we find that the temporal phase varies as

$$\phi(t, z) = \int \frac{\partial \phi}{\partial z}(t, z) dz = \phi(t, 0) - \frac{\omega_c}{c} (1 + n_2 I(t)) z.$$

2.1 Optical frequency comb theory

This relation indicates that SPM is induced via the intensity I of the propagating field and the distance z this field propagates through the medium. From this, the naming of self-phase modulation also becomes clear. When a field propagates through such a nonlinear medium, its temporal phase ϕ changes according to the time-varying intensity of the field itself.

An interesting effect of SPM can be seen when inspecting the instantaneous frequency defined as $\omega_{\text{inst}} := \partial\phi/\partial t$. Assuming a Gaussian-shaped field amplitude $\sqrt{I(t)} = \sqrt{I_0}e^{-t^2/(2\Delta\tau^2)}$, where Δt characterizes the width of the field and $\sqrt{I_0}$ defines its amplitude, the instantaneous frequency then takes the form of

$$\omega_{\text{inst}}(t, z) := \frac{\partial\phi}{\partial t}(t, z) = \frac{\partial\phi}{\partial t}(t, 0) + \left(n_2 \frac{\omega_c}{c} \frac{2I_0}{\Delta\tau^2} z \right) t e^{-(t/\Delta\tau)^2}. \quad (2.9)$$

This shape can be seen on the left side of figure 2.3. We can see from the instantaneous frequency that due to SPM, new frequencies are being generated inside a temporal field. Higher frequencies are shifted towards the end of the pulse (positive times), while lower frequencies are shifted towards the beginning of the pulse (negative times). No shift occurs at the maximum of the pulse. Around the center, an approximate linear frequency shift can be observed (linear chirp). The newly generated frequencies effectively broaden the spectrum of the field in Fourier space. As a note, it is possible to analytically predict the characteristic features of this broadening [75].

The analysis so far has neglected dispersion. However, there will always be additional dispersion effects in real materials that induce SPM. If the incident field is Fourier-limited and the nonlinear material has normal dispersion ($D_2 > 0$), then low frequencies will have higher phase velocities than high frequencies. Since low frequencies are generated in front of the pulse and high ones in the back, the frequencies effectively spread and broaden the pulse in time. For initial anomalous dispersion ($D_2 < 0$), on the other hand, the low and high frequencies can converge, effectively compressing the pulse in time before broadening again [71, ch. 4.1.3].

To illustrate the effects of self-phase modulation without dispersion in the frequency domain, a numerical analysis is shown on the right side of figure 2.3. As the pulse is propagating through a distance z of the medium, the spectrum is broadened in a characteristic way. This induces a typical shape in the instantaneous frequency of the pulse, as described by equation (2.9), while the temporal shape remains nearly unaffected. The used simulation, however, includes an additional nonlinear effect called self-steepening [71, ch. 4.3.1], which leads towards a distortion of the temporal shape due to spectral broadening being stronger for higher frequencies. A characteristic oscillatory shape of the spectral amplitude emerges alongside the broadening of the spectral bandwidth. This oscillatory structure can be attributed to SPM-induced frequency chirp from equation (2.9). This can be illustrated as follows: For each generated frequency, there will always be two points inside the temporal pulse with the same instantaneous frequency but, in general, two different phases. These phases can interfere constructively or destructively. This interference gives rise to the multipeak structure of the spectrum.

SPM can be accompanied by other nonlinear processes such as stimulated Raman scattering [71, ch. 8] and four-wave mixing [71, ch. 10.1]. These can result in broadening

of the spectral bandwidth beyond the broadening rate of SPM. Such broadening is referred to as a supercontinuum or white-light continuum [76].

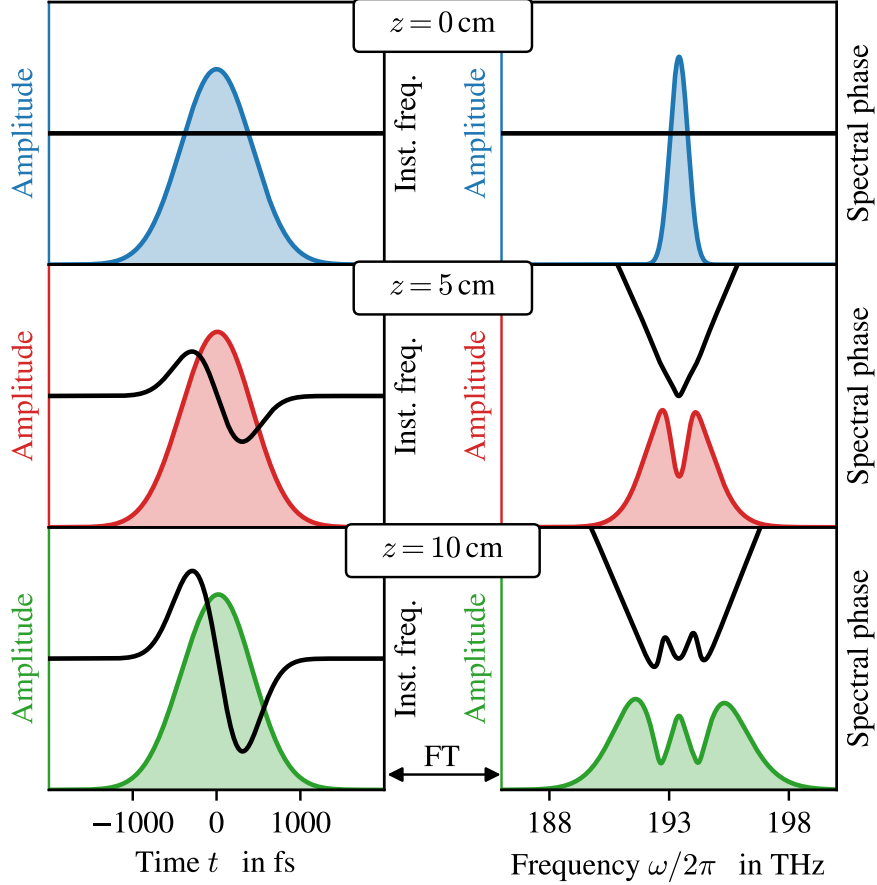


Figure 2.3: **Effects of self-phase modulation on a pulse.** A Fourier-limited Gaussian pulse with an average power of 1.5 W is simulated traveling through a nonlinear fiber of length z with a nonlinear coefficient $\gamma = 10.7 \text{ (W km)}^{-1}$ while disregarding dispersion. The drawn simulations are based on equation (2.7) if dispersion is disregarded. FT: Fourier transformation, inst. freq.: instantaneous frequency.

The simulator used for figure 2.3 has the project name py-fmas [74]. The code can be found in <https://github.com/omelchert/py-fmas>. It should be noted that the simulation takes the convention that the second-order nonlinear refractive index $n_{2,\text{py-fmas}}$ has units of $1/\text{W}$ instead of m^2/W because the simulation integrates over the effective mode area

$$n_{2,\text{py-fmas}} = \frac{n_2}{A_{\text{eff}}}.$$

As a consequence, the field amplitude passed into the simulation has units of root power $\sqrt{\text{W}}$ instead of root intensity $\sqrt{\text{W}/\text{m}^2}$, which can be obtained

$$E_{\text{py-fmas}}(t) = E(t) \sqrt{A_{\text{eff}}}.$$

2.1.4 Generation, stabilization, and applications

Shifting from the mathematical treatment to practical considerations, we now consider how an optical frequency comb is generated, how the repetition rate ω_{rep} and the carrier-envelope offset frequency ω_{CEO} are stabilized, and what some of their applications are.

Various techniques have been developed to generate optical frequency combs, with passive and active mode locking being the most predominant. Mode locking [61, ch. 2] refers to the phase locking of different longitudinal modes within a laser cavity. The basic principle of mode locking is that of an oscillator: The interaction between a pump laser and a gain medium generates initial photons, which, through stimulated emission and mode locking, evolve into a coherent optical frequency comb. The gain medium further amplifies these photons, while a partially transparent mirror serves as an output coupler.

To go further into detail, at the core of mode locking is the need to synchronize the phases of the longitudinal modes of the laser cavity. In a typical laser, the cavity supports many modes, each corresponding to a different frequency. When these modes oscillate independently, they can produce a continuous wave of light. However, mode locking ensures that these modes are not independent; instead, their phases are locked together in such a way that the combined output is not a continuous wave, but rather a train of ultrashort pulses. This synchronization is achieved through periodic modulation or nonlinear interactions within the cavity, which causes the electromagnetic waves to constructively interfere at regular intervals, generating pulses at a specific repetition rate. The pulse durations can reach a time scale of picoseconds or femtoseconds, leading to the creation of an optical frequency comb (a spectrum of discrete, evenly spaced frequencies).

In active mode locking the phase relationship between the longitudinal modes is controlled by an external modulator, such as an acousto-optic or electro-optic modulator, that periodically regulates the cavity losses or the round-trip phase shifts. In contrast, passive mode locking occurs without an external modulator. Instead, it relies on an intensity-dependent mechanism that favors the formation of short pulses over continuous waves. One approach, used in our frequency comb setup, exploits nonlinear polarization rotation [71, ch. 6]. By designing the system with polarization optics in such a way that beams experiencing nonlinear polarization rotation encounter minimal losses, high-intensity pulses are selectively amplified while low-intensity continuous waves are suppressed. Further details about this technique are provided in section 3.1. Because passive mode locking does not depend on the speed or efficiency of an external modulator, it can produce pulse trains with shorter pulse durations than active mode locking.

Once the train of ultrashort pulses is produced, an optical frequency comb can be generated by stabilizing the repetition rate and the carrier-envelope offset frequency. The repetition rate ω_{rep} is usually on the order of MHz to GHz and depends on the length of the cavity. An appropriate photodiode can be used to measure such frequencies by picking off a portion of the generated light. As the repetition rate of the signal is typically a radio-frequency it is straightforward to measure directly. Through a feedback loop (phase-locked loop [77]) into the optical frequency comb generator, a setpoint, and an error signal, one can then stabilize the repetition rate. This can be achieved by using piezoelectric actuators to drive the cavity mirrors.

Stabilizing the carrier-envelope offset frequency ω_{CEO} , on the other hand, is more

involved. Theodor Hänsch and John Hall were awarded with Nobel Prize in 2005 due to the invention of the basic scheme for this procedure [78–80]. The technique they developed is called the “ f - $2f$ ” self-referencing scheme and requires broadening the spectral bandwidth of the optical frequency comb via self-phase modulation (see section 2.1.3) to a white-light continuum such that the spectral bandwidth covers more than one octave. This means that inside the bandwidth there should be one frequency ω_n that, when doubled, still falls inside the bandwidth. This frequency is doubled using second harmonic generation (SHG), creating the frequency $2\omega_n$, and is then compared with the frequency ω_{2n} . In practice we split the optical frequency comb into two paths. One path is transformed into a white-light continuum, and the other passes through a nonlinear crystal, which can generate second harmonics. Overlapping these two beams and making them interfere creates a beat signal, where the lowest frequency will be

$$\begin{aligned} \text{“}f\text{-}2f\text{”} : \quad 2\omega_n - \omega_{2n} &= 2(\omega_{\text{CEO}} + n\omega_{\text{rep}}) - (\omega_{\text{CEO}} + 2n\omega_{\text{rep}}) \\ &= \omega_{\text{CEO}}, \end{aligned} \quad (2.10)$$

as depicted in figure 2.4. The carrier-envelope offset frequency is directly extracted from the beat frequency. It is typically in the MHz range and can be measured and stabilized using the same feedback method as the repetition rate.

Typical applications for optical frequency combs involve beat notes between themselves and other lasers as their core component. These allow linking optical frequencies to radio frequencies. Such techniques are used for high-accuracy metrology [81], laser frequency references and stabilization [56], dual-comb spectroscopy [82, 83], and more. In this work, the narrow peaks of an optical frequency comb will be used to drive Raman transitions in a quantum system whose energies fall within the spectral bandwidth as already demonstrated by [44] and [45]. For driving Raman transitions, it is important to have a stable repetition rate; however, the carrier-envelope offset frequency is irrelevant for this interaction, as only the frequency difference of two photons counts, and the carrier-envelope offset frequency thus cancels out.

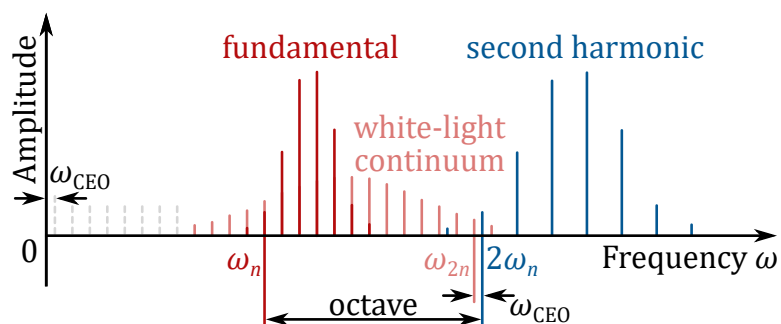


Figure 2.4: **Measurement technique of the carrier-envelope offset frequency.** By generating a white-light continuum out of an optical frequency comb that spans at least an octave and beating it with its second harmonic, it is possible to measure the carrier-envelope offset frequency ω_{CEO} as shown in the schematic. The drawing is based on equation (2.10).

2.2 Light-atom interaction

This section describes the interaction between an optical frequency comb and a trapped ion system, specifically for the example of a calcium-40 ion. For this, basic concepts around the calcium-40 ion, such as energy level structure, Zeeman substructure, and AC-Stark shifts, will be presented in section 2.2.1. Although not central for this thesis, two-photon Raman transitions in a three-level system using two continuous-wave lasers will be discussed in section 2.2.2. This concept of Raman transitions will be expanded in section 2.2.3 to enable the description of the used interaction between an optical frequency comb and an ion. Section 2.2.4 covers Ramsey interferometry used in our experiments.

2.2.1 Calcium-40 ion theory and two-level system

Calcium-40 ions ($^{40}\text{Ca}^+$) are a popular platform for quantum information processing platforms due to the relatively long lifetime of the D -level excited state (~ 1 s) for encoding a qubit state and their experimentally accessible transition frequencies using continuous-wave lasers [84]. The setup of the research group where this work was conducted is capable of readily trapping calcium-40 ions in a linear Paul trap. The aim of this section is to describe the calcium's interaction with a continuous-wave laser field to lay the foundation for a description using Raman transitions and then further involving an optical frequency comb. For the sake of simplicity, the ion will be modeled as a two-level system by picking two arbitrary real states and is assumed to rest in space without the need of any trapping potential and be in its motional ground state.

The ion can be described as a hydrogen-like quantum system due to there being only a single valence electron in its outermost shell. Additionally, it does not have any hyperfine structure. The Hamiltonian describing the electronic states of the calcium ion takes the form of

$$H_{\text{atom}} = \sum_j \hbar\omega_j |j\rangle \langle j|, \quad (2.11)$$

where $\hbar\omega_j$ describes the eigenenergies and $|j\rangle$ are the corresponding eigenstates in Dirac notation. The constant \hbar is the reduced Planck constant, and ω_j is the angular frequency of the j -th energy level. For our specific case, the eigenstates can be characterized by five quantum numbers as

$$|j\rangle = |n, S, L, J, m_J\rangle.$$

The quantum numbers describe the quantum state in which the valence electron of the ion is [27, ch. 5]. The principal quantum number $n \in \mathbb{N}$ is related to how far, on average, the electron is from the nucleus. The angular momentum quantum number for spin $S = 1/2$ describes the spin of the single electron and is always $1/2$ due to there being only one valence electron. The azimuthal quantum number $L \in \{0, 1, \dots, n-1\}$ determines the electron's orbital angular momentum and specifies the shape of the orbital. The total angular momentum quantum number $J \in \{|L-S|, |L-S|+1, \dots, |L+S|\}$ combines the azimuthal and spin angular momentum and parametrizes the total angular momentum

due to the presence of spin-orbit coupling. The projection of the total angular momentum along the quantization axis $m_J \in \{-J, -J+1, \dots, J\}$ becomes relevant when a magnetic field is applied and lifts the $2J+1$ -fold degeneracy. The quantization axis is defined as the local direction of the applied magnetic field \vec{B} at the position of the ion.

These quantum numbers are typically concentrated in a single notation that describes the eigenenergies of the valence electron called term symbols [85]. The notation follows

$$n^{2S+1}L_J(m_J),$$

where for $L=0$ we replace L with S , for $L=1$ we replace L with P , and for $L=2$ we replace L with D according to spectroscopic notation [86]. Central to this work are the states with $n=3$, $S=1/2$, $L=2$, and $J=3/2$ and $J=5/2$, since coherent state manipulation between these two general states is performed using an optical frequency comb. Omitting the specification of m_J , these values lead to the notation $3^2D_{3/2}$ and $3^2D_{5/2}$.

The eigenenergies $\hbar\omega_j$ of the calcium ion Hamiltonian in equation (2.11) generate a unique energy structure, which is qualitatively depicted in figure 2.5. The figure only shows the lifted degeneracy of an applied magnetic field for the 3^2D_J states.

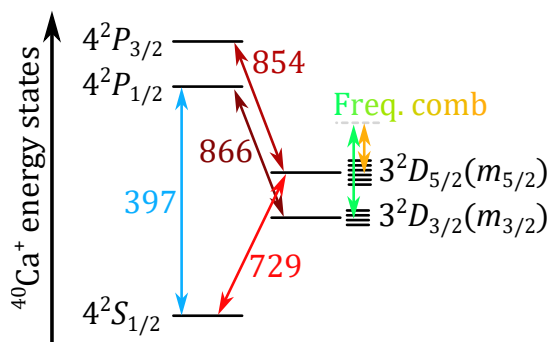


Figure 2.5: **Simplified energy structure of a calcium-40 ion.** Drawn are the lowest relevant energy levels of the ion labeled using term symbols. The wavelengths of the transitions are given in nm. The Zeeman substructure of the D -levels is also sketched, and is determined by the quantum number m_J . This image is a representation of equation (2.11).

For the purposes of this work, it is important to understand how the $2J+1$ -fold degeneracy is lifted due to the influence of an external B -field. Let $\hbar\omega_0$ be the eigenenergy of a particular degenerate state, i.e., a state that for zero B -field, and $\hbar\omega_{m_J}$ the same eigenenergy but with lifted degeneracy. The degeneracy is lifted when an external B -field is applied due to the interaction $-\vec{\mu}_J \cdot \vec{B}$, where $\vec{\mu}_J$ is the magnetic moment associated with the total angular momentum \vec{J} of the electron, leading to discrete energy shifts depending on the quantum number $\vec{\mu}_J$. This so-called Zeeman splitting then has the magnitude [87, ch. 7.4]

$$\Delta\omega_{\text{Zeeman},m_J} = \omega_{m_J} - \omega_0 = \frac{1}{\hbar} m_J g_J \mu_B B, \quad (2.12)$$

2.2 Light-atom interaction

where g_J is the Landé g -factor, the Bohr magneton is denoted as μ_B , and the magnetic field strength as $B = |\vec{B}|$. To first order, the Landé g -factor is given by [87, ch. 7.4]

$$g_J = 1 + \frac{J(J+1) + S(S+1) - L(L+1)}{2J(J+1)}. \quad (2.13)$$

In this work we need the values for the 3^2D_J states. Using equation (2.13), we can evaluate them to be $g_{3/2} = 0.8$ and $g_{5/2} = 1.2$. The accuracy of modern experiments require higher-order corrections for the here presented simple model, leading to slightly different Landé g -factors. For the experiments to be performed in this work, these first-order calculations are not sufficiently precise. An experimental value for the $3^2D_{5/2}$ was found [88, p. 81]

$$g_{5/2}^{\text{exp}} = 1.200\,333\,75(3), \quad (2.14)$$

but to our knowledge, the Landé g -factor $g_{3/2}$ of the $3^2D_{3/2}$ state has not been measured. This work experimentally measures this value.

Appropriately chosen continuous-wave lasers can be used to manipulate the quantum state of a calcium ion. To see how, we assume that the laser's frequency ω_L roughly corresponds to a frequency difference, or transition frequency, $\omega_{\text{atom}} = \omega_e - \omega_g$ of two eigenenergies associated with the eigenstates $|g\rangle = |j_1\rangle$ (ground state) and $|e\rangle = |j_2\rangle$ (excited state). We additionally assume that the wave function of the electron can be expressed in terms of a radial function and spherical harmonics, implying that the wave function has definite parity, which is important for later defining the Rabi rates. We also assume that the laser field is far-detuned from any other transition. This allows us to treat the light-atom system as an effective two-level system. The Hamiltonian of the two-level system takes the following form:

$$H_{\text{atom}}^{ge} = 0 |g\rangle \langle g| + \hbar\omega_{\text{atom}} |e\rangle \langle e|,$$

where the energy reference was set to the ground state energy $\hbar\omega_g$. A sketch of this situation is shown in figure 2.6.

We can model the electric field via

$$\vec{E}(\vec{r}, t) = \frac{1}{2} \vec{E}_0 e^{i(\vec{k}_L \cdot \vec{r} - \omega_L t + \phi_L)} + \text{c.c.}, \quad [\vec{E}_0] = \frac{\text{V}}{\text{m}}, \quad (2.15)$$

where \vec{E}_0 is complex and defines the amplitude and direction (polarization) with which the electric field is oscillating in space, the wave vector \vec{k}_L defines the propagation direction of the light, and ϕ_L defines a phase offset. The abbreviation c.c. denotes the complex conjugate of the preceding expression. When applied to only a single object, it is also denoted with the symbol *. Since we are not considering the motion of the ion, we can apply the electric dipole approximation $e^{i\vec{k}_L \cdot \vec{r}} \approx 1$, which assumes that the wavelength of the field is much larger than the spatial extension of the ion [89, ch. 5.1.2].

In an electric dipole transition, an ion absorbs or emits a photon due to the interaction between its electric dipole moment and an oscillating electric field, such as that of a laser.

The interaction Hamiltonian describing this process can be derived from the potential energy of an electric dipole in an external electric field, and is given by [52]

$$H_L(t) = -\vec{p} \cdot \vec{E}(t), \quad (2.16)$$

where \vec{p} is the electric dipole moment operator. By changing the basis of this expression using the identity $\mathbb{I} = |g\rangle\langle g| + |e\rangle\langle e|$, defining the Rabi rate

$$\Omega := |\Omega|e^{i\phi_\Omega} := \frac{1}{\hbar} \langle e | \vec{p} \cdot \vec{E}_0 | g \rangle, \quad \tilde{\Omega} := |\tilde{\Omega}|e^{i\tilde{\phi}_\Omega} := \frac{1}{\hbar} \langle e | \vec{p} \cdot \vec{E}_0^* | g \rangle,$$

and recognizing that the diagonal elements vanish, i.e., $\langle g | \vec{p} \cdot \vec{E}_0 | g \rangle = \langle e | \vec{p} \cdot \vec{E}_0 | e \rangle = 0$, due to definite parity, we can rephrase the Hamiltonian of equation (2.16) as

$$H_L(t) = -\frac{\hbar|\Omega|}{2} (|e\rangle\langle g| e^{-i(\omega_L t - \phi_L - \phi_\Omega)} + \text{h.c.}) \\ -\frac{\hbar|\tilde{\Omega}|}{2} (|e\rangle\langle g| e^{i(\omega_L t - \phi_L + \tilde{\phi}_\Omega)} + \text{h.c.}),$$

where h.c. denotes the Hermitian conjugate of the preceding expression, also denoted with the symbol \dagger if it is only applied to a single object.

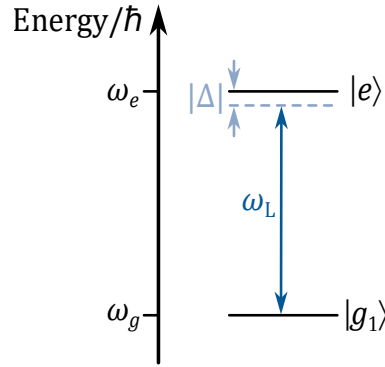


Figure 2.6: **Two-level system with one interacting field.** A continuous-wave laser field with frequency ω_L interacts with two energy levels $\hbar\omega_g$ and $\hbar\omega_e$ with an interaction strength proportional to the Rabi frequency Ω . This figure is based on equation (2.18) and is a simplification of the energy structure shown in figure 2.5.

The total Hamiltonian can now be written as $H(t) = H_{\text{atom}}^{ge} + H_L(t)$. To analyze this Hamiltonian, it is useful to introduce unitary operators U that fulfill $U^\dagger U = \mathbb{I}$, as they will allow us to bring forth experimentally relevant quantities. These operators can perform a basis transformation on a Hamiltonian while preserving the Schrödinger equation $i\hbar \frac{d}{dt} |\psi(t)\rangle = H |\psi(t)\rangle$ and the eigenenergies, meaning that the transformed Hamiltonian and its corresponding eigenstates retain the same eigenenergies as the original Hamiltonian and eigenstates. A unitary transformation on a Hamiltonian and a general state vector is defined by

$$H_U = U^\dagger H U + i\hbar \frac{dU^\dagger}{dt} U \quad \text{and} \quad |\psi_U(t)\rangle = U^\dagger |\psi(t)\rangle$$

2.2 Light-atom interaction

and fulfills the Schrödinger equation

$$i\hbar \frac{d}{dt} |\psi_U(t)\rangle = H_U |\psi_U(t)\rangle.$$

The unitary operator $U_1 = e^{-iH_{\text{atom}}^{ge}t/\hbar}$ changes the description into the so-called rotating frame of reference [90], or interaction picture, resulting in

$$\begin{aligned} H_I &= U_1^\dagger H U_1 + i\hbar \frac{dU_1^\dagger}{dt} U_1 \\ &= -\frac{\hbar|\Omega|}{2} (|e\rangle \langle g| e^{-i((\omega_L - \omega_{\text{atom}})t - \phi_L - \phi_\Omega)} + \text{h.c.}) \\ &\quad - \frac{\hbar|\tilde{\Omega}|}{2} (|e\rangle \langle g| e^{i((\omega_L + \omega_{\text{atom}})t - \phi_L + \tilde{\phi}_\Omega)} + \text{h.c.}) \\ &\stackrel{\text{RWA}}{\approx} -\frac{\hbar|\Omega|}{2} |e\rangle \langle g| e^{-i(\Delta t - \phi_L - \phi_\Omega)} + \text{h.c.}, \end{aligned} \quad (2.17)$$

where $\Delta = \omega_L - \omega_{\text{atom}}$ is the detuning between the laser frequency and the transition frequency. The change into the rotating frame cancels out H_{atom}^{ge} and reveals two different timescales, a fast $\omega_L + \omega_{\text{atom}}$ and a slow $\omega_L - \omega_{\text{atom}} = \Delta$ timescale.

The last equation applies the rotating wave approximation (RWA), which disregards fast dynamics driven by phase terms with frequencies $\omega_L + \omega_{\text{atom}} \gg \omega_L - \omega_{\text{atom}} = \Delta$ as these average out for slow timescales comparable to the detuning Δ . The RWA acts as a low-pass filter on the system's frequencies as it effectively removes high-frequency oscillations from the system's equations [91].

The remaining time dependence in the Hamiltonian can be eliminated by changing to frame of reference which rotates at the detuning frequency Δ using the unitary operator $U_2 = e^{-i(\Delta t - \phi_L - \phi_\Omega)|e\rangle \langle e|}$. This leads to a simplified light-atom interaction Hamiltonian

$$\begin{aligned} H_{\text{LA}} &= U_2^\dagger H_I U_2 + i\hbar \frac{dU_2^\dagger}{dt} U_2 \\ &= -\frac{\hbar|\Omega|}{2} (|g\rangle \langle e| + |e\rangle \langle g|) - \hbar\Delta |e\rangle \langle e|. \end{aligned} \quad (2.18)$$

Due to the properties of unitary transformations, this Hamiltonian preserves the eigenenergies of the original Hamiltonian H . Solving the Schrödinger equation by finding the roots of the characteristic polynomial $\det(H_{\text{LA}} - \lambda\mathbb{I})$ yields the eigenenergies

$$\lambda_{\pm} = \frac{\hbar}{2} (-\Delta \pm \sqrt{|\Omega|^2 + \Delta^2}), \quad (2.19)$$

where \det denotes the determinant operation. From this we can find the eigenstates of the coupled field-atom system, called dressed states, which we use to describe the evolution of a state $|\psi_{\text{LA}}(t)\rangle = e^{-iH_{\text{LA}}t/\hbar} |\psi_{\text{LA}}(t=0)\rangle$, where $|\psi_{\text{LA}}(t)\rangle = U_2^\dagger U_1^\dagger |\psi(t)\rangle$. Setting the initial state as $|\psi(t=0)\rangle = |g\rangle$, we can predict the evolution of the two-level system interacting

with the laser light by observing the probability of finding the ion in the state $|e\rangle$ defined as

$$\begin{aligned}
 p_e &= |\langle e|\psi(t)\rangle|^2 \\
 &= |\langle e|\psi_{\text{LA}}(t)\rangle|^2 |e^{-i((\omega_{\text{atom}}+\Delta)t-\phi_{\text{L}}-\phi_{\Omega})}|^2 \\
 &= \left(\frac{|\Omega|}{\Omega'}\right)^2 \sin^2\left(\frac{1}{2}\Omega't\right) \\
 &= \left(\frac{|\Omega|}{\Omega'}\right)^2 \frac{1}{2}(1 - \cos(\Omega't)) \tag{2.20}
 \end{aligned}$$

$$= \left(\frac{1}{2}|\Omega|t\right)^2 \text{sinc}^2\left(\frac{1}{2}\Omega't\right), \tag{2.21}$$

where $\Omega' = \sqrt{|\Omega|^2 + \Delta^2}$ is the generalized Rabi frequency. We can see that for large detunings $\Delta/|\Omega| \gg 1$ the population transfer to the excited state is largely suppressed. This process of coherently transferring population between quantum states is what we refer to as actively driving transitions.

The pulse length t is the time over which the laser interacts with the ion. When referring to an optical frequency comb, this quantity is more appropriately called the pulsetrain to avoid confusion with the length of a single pulse within the comb. Varying the pulse length for a given detuning (usually $\Delta = 0$) yields a population oscillation of the excited state. These are commonly known as Rabi flops, or Rabi oscillations, $p_e(t, \Delta = 0)$. On the other hand, we can also vary the detuning Δ for fixed pulse length t , which is often set to the π -time $t_\pi = \pi/|\Omega|$, and retrieve the Rabi spectrum $p_e(t = t_\pi, \Delta)$.

The forms in equations (2.20) and (2.21) are useful for fitting experimental data, as they explicitly reveal the functional dependence observed in the data and can easily be adjusted to include system imperfections. For data retrieved from varying the pulse length with a target detuning of $\Delta = 0$, the following Rabi flop model can be used to describe the behavior:

$$p_{e,\text{flop}}(t) = \frac{A}{2} \cos(\Omega(t - t_0)) e^{-t/\tau} + c, \tag{2.22}$$

with parameters A, t_0, Ω, c , and τ . The parameters, except for Ω , account for different imperfections in the quantum system and system calibrations. The offset c is, according to the derived theory, ideally equal to 0.5 but can range from 0 to 1. Together with the amplitude $A \in [0, 2\min\{c, 1 - c\}]$ and the time offset t_0 , these free parameters can incorporate various imperfections such as non-zero detuning, state preparation infidelities, and environmental noise sources such as magnetic field fluctuations. The parameter τ represents the decay time constant of the Rabi oscillations, which typically reflects the timescale over which the oscillation amplitude decays due to dissipative effects like relaxation, dephasing, or loss of coherence. Further discussion about system noise, specifically dephasing noise, is held in section 2.2.4.

For varying the frequency and measuring the Rabi spectrum, the pulse length is set to

2.2 Light-atom interaction

the π -time $t = t_\pi$. Inserting this into equation (2.21) leads to the model

$$p_{e,\text{spec}}(\Delta) = A \left(\frac{\pi}{2}\right)^2 \text{sinc}^2 \left(\frac{\pi}{2} \sqrt{1 + \left(\frac{\Delta - \Delta_0}{\Omega}\right)^2} \right) + c, \quad (2.23)$$

with parameters A, Δ_0, Ω , and c . The amplitude $A \in [-1, 1]$ and the offset $c \in [\max\{0, -A\}, \min\{1, 1 - A\}]$ have similar justifications as for the Rabi flop model. The detuning offset Δ_0 accounts for reference frames that are not centered around zero detuning.

Another important effect resulting from the interaction of a light field with an ion is the AC-Stark effect. Recalling the eigenenergies from equation (2.19), they represent a combination of the isolated atom energy, the photon energy, and the interaction energy. For small detunings $|\Delta|/|\Omega| \ll 1$, the eigenvalues cannot be associated with a particular eigenstate of the isolated atom but rather to a superposition of them. However, for large detunings $|\Omega|/|\Delta| \ll 1$, the eigenenergies, which, using a Taylor expansion, can be approximated by

$$\begin{aligned} \lambda_\pm &\approx \frac{\hbar}{2} \left(-\Delta \pm |\Delta| \left(1 + \frac{|\Omega|^2}{2\Delta^2} \right) \right) \\ &\approx \frac{\hbar}{2} (-\Delta \pm |\Delta|), \end{aligned}$$

can be linked to the original eigenstates and eigenenergies of the isolated atom, which becomes evident if we consider the case of $|\Omega| \rightarrow 0$. If $\Delta > 0$, then $\lambda_+ = 0$ and $\lambda_- = -\hbar\Delta$. By setting $\omega_L = 0$, it becomes evident that $\lambda_+ = 0$ can be associated with the ground state and $\lambda_- = \hbar\omega_{\text{atom}}$ to the excited state. The opposite is true for $\Delta < 0$.

Having identified which eigenenergy corresponds to the ground or excited state under the given conditions, we can describe how the laser's interaction affects the atom's original eigenenergies. To illustrate this, consider the following: In a more complete quantum description of the system, the ground state would be described as the tensor product $|g\rangle |n\rangle$ and the excited state as $|e\rangle |n-1\rangle$, where n describes the number of photons in the system. Let us consider the isolated atom energy together with the interaction energy but disregard the laser's photon energy. We can remove the offset in photon number by manually adding the energy of a photon $\hbar\omega_L$ to the excited state of an atom. This allows us to effectively trace out the $|n\rangle$ state and have a different point of view on how the isolated atom reacts to solely the interaction energy. Overall, this then leads to

$$\begin{aligned} E_g(\Delta, |\Omega|) &= 0 + \begin{cases} \lambda_+, & \text{if } \Delta > 0 \\ \lambda_-, & \text{if } \Delta < 0 \end{cases} = \hbar \frac{|\Omega|^2}{4\Delta}, \\ E_e(\Delta, |\Omega|) &= \hbar\omega_L + \begin{cases} \lambda_-, & \text{if } \Delta > 0 \\ \lambda_+, & \text{if } \Delta < 0 \end{cases} = \hbar\omega_{\text{atom}} - \hbar \frac{|\Omega|^2}{4\Delta}, \end{aligned}$$

where E_g and E_e are the atoms ground and excited state energy, respectively, with interaction, disregarding the laser's photon energy of the combined system. This point of

view makes it clear that the interaction with the laser field introduces shifts in the energy structure of the atom, called the AC-Stark effect or AC-Stark shift. We can define these shifts as

$$\begin{aligned} \hbar\delta_g &= E_g(\Delta, |\Omega|) - E_g(\Delta, 0) = \hbar \frac{|\Omega|^2}{4\Delta}, \\ \text{and} \quad \hbar\delta_e &= E_e(\Delta, |\Omega|) - E_e(\Delta, 0) = -\hbar \frac{|\Omega|^2}{4\Delta}. \end{aligned} \quad (2.24)$$

These results can be summarized as an effective Hamiltonian describing a two-level system with far-detuned laser light as

$$H_{\text{AC}} = \hbar \frac{|\Omega|^2}{4\Delta} (|g\rangle \langle g| - |e\rangle \langle e|). \quad (2.25)$$

Since $\Omega \propto E_0$, with E_0 being the amplitude of the electric field, the AC-Stark shift is linearly dependent on the intensity of the laser field. For detunings or Rabi frequencies where the RWA cannot be justified, i.e., when they become comparable to the laser or transition frequency, corrections have to be applied to the AC-Stark shift.

In the following, we will examine how the AC-Stark shift of a single energy level, as defined in equation (2.24), is modified by the presence of multiple energy levels in real atomic structures. A laser field can in principle interact with any energy level pair. Even though no significant transfer of population between off-resonant energy levels is possible, the coupling might still be noticeable via the AC-Stark effect. We can focus on a particular eigenstate $|g\rangle$ and analyze how the AC-Stark shift affects its eigenenergy $\hbar\omega_g$. Due to the laser field, this eigenstate couples to many other eigenstates $|e_j\rangle$ with eigenenergies $\hbar\omega_{e_j}$ with coupling strengths (or Rabi rates) $|\Omega_{g,e_j}|$. If we define the detunings as $\Delta_{g,e_j} = \omega_L - |\omega_{e_j} - \omega_g|$, then the total AC-Stark shift on the energy level $\hbar\omega_g$ due to the interaction of the atom with the laser field amounts to

$$\hbar\delta_g = \hbar \sum_j \text{sgn}(\omega_{e_j} - \omega_g) \frac{|\Omega_{g,e_j}|^2}{4\Delta_{g,e_j}}.$$

Many of these summands, or contributions to the AC-Stark shift, can be neglected due to the nature of the coupling (Rabi rate) and the magnitude of the detuning. In this work, the AC-Stark shift becomes relevant in the context of the optical frequency comb with a center wavelength of 1572 nm. For this work, the relevant energy levels that undergo shifting are the 3^2D_J states, as some of their sublevels will be used as the ground and excited states. Further discussion is held at the end of section 2.2.2.

The derivation throughout this section assumes that the light-atom interaction follows an electric dipole interaction. Other common transitions are electric quadrupole or magnetic dipole transitions. However, the only difference boils down to the definition of the Rabi rate $|\Omega|$, resulting in potentially different orders of magnitude of the Rabi rates. The remaining treatment for a two-level system is analogous, as presented here.

Another assumption was that the laser field applied to the ion was of the continuous-wave type. However, this work uses a pulsed optical frequency comb for coherently driving

2.2 Light-atom interaction

transitions. The differences in the derivation between continuous-wave and pulsed lasers boil down to their spectra. However, when the repetition rate of the pulsed laser greatly exceeds the Rabi rate and other relevant timescales such as the π -time, there are no qualitative differences in the results. Further discussion on the interaction of an optical frequency comb with an ion will be held in section 2.2.3.

2.2.2 Two-photon Raman transition

In the previous section we discussed a quantum mechanical two-level system interacting with a laser field. If we introduce a three-level system interacting with two separate laser fields, then a special type of transition called a Raman transition can emerge. Continuous-wave Raman transitions are a useful tool as they allow us to drive transitions in an energy range of up to a few GHz. The interaction emerges if we introduce two ground states, denoted as $|g_1\rangle$ and $|g_2\rangle$, with eigenenergies $\hbar\omega_{g1}$ and $\hbar\omega_{g2} > \hbar\omega_{g1}$, respectively, and a far-off-resonant excited state, $|e\rangle$, with eigenenergy $\hbar\omega_e > \hbar\omega_{g2} > \hbar\omega_{g1}$. Furthermore, the frequency difference of the two involved continuous-wave fields should approximately correspond to the frequency difference of the two ground states. The described situation, which is the special case of a Λ -configuration, is depicted in figure 2.7.

We can describe the two laser fields interacting with the three-level system analogously to equation (2.15) as

$$\vec{E}(\vec{r}, t) = \frac{1}{2}\vec{E}_1 e^{i(\vec{k}_{L1}\cdot\vec{r}-\omega_{L1}t+\phi_{L1})} + \frac{1}{2}\vec{E}_2 e^{i(\vec{k}_{L2}\cdot\vec{r}-\omega_{L2}t+\phi_{L2})} + \text{c.c.}$$

As before, the amplitudes and polarizations are encoded in \vec{E}_j , where $j \in \{1, 2\}$, the propagation directions are set by the wave vectors \vec{k}_{Lj} , the laser frequencies are denoted as ω_{Lj} , and possible phases are described by ϕ_{Lj} . We can take the same steps as in section 2.2.1: applying the electric dipole approximation $e^{i\vec{k}_{Lj}\cdot\vec{r}} \approx 1$, changing to the interaction picture, and applying the rotating wave approximation (RWA). This leads to a Hamiltonian resembling equation (2.17)

$$H = -\frac{\hbar|\Omega_1|}{2} |e\rangle \langle g_1| e^{-i(\Delta_1 t - \phi_{L1} - \phi_{\Omega 1})} - \frac{\hbar|\Omega_2|}{2} |e\rangle \langle g_2| e^{-i(\Delta_2 t - \phi_{L2} - \phi_{\Omega 2})} + \text{h.c.}, \quad (2.26)$$

where the coupling strengths $|\Omega_j|$ are between a ground state $|g_j\rangle$ and the excited state $|e\rangle$, and the detunings are defined as $\Delta_j = \omega_{Lj} - |\omega_e - \omega_{gj}|$. It is important to note that the RWA might fail for large detunings Δ_j [92]. In this case, one has to also treat the $\omega_{Lj} + |\omega_e - \omega_{gj}|$ terms alongside the $\omega_{Lj} - |\omega_e - \omega_{gj}|$ terms. Here we assume that the RWA is valid.

A generalization of the RWA can be applied to this expression. Derived by James and Jerke [91], their method demonstrates how to generate effective Hamiltonians by effectively filtering out high-frequency contributions. Taking over their assumptions, which basically assume off-resonant couplings with $|\Delta_2 - \Delta_1| \ll \Delta_j$, and then using their principal result

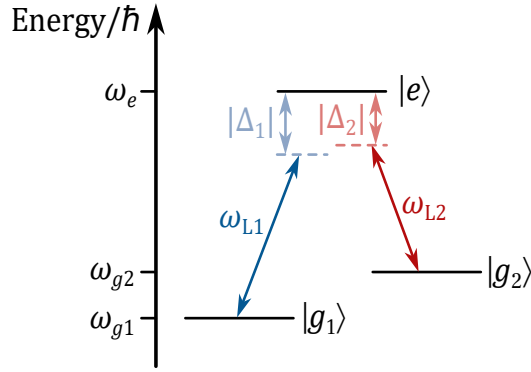


Figure 2.7: **Three-level system with two fields undergoing a Raman transition.** Shown are two fields with frequencies ω_{L1} and ω_{L2} whose difference frequency roughly equates to the difference frequency between the two ground states with energy levels $\hbar\omega_{g1}$ and $\hbar\omega_{g2}$. The intermediate excited state with energy $\hbar\omega_e$ mediates the coherent interaction between the two ground states with a strength proportional to the Raman Rabi rate Ω_R . This configuration is a special case of the Raman transition and is called the Λ -configuration. The figure is based on equation (2.29).

by adapting its terms to our problem, leads to an effective Hamiltonian of the form

$$\begin{aligned}
 H_{\text{eff}} = & \underbrace{\frac{\hbar|\Omega_1|^2}{4\Delta_1}(|g_1\rangle\langle g_1| - |e\rangle\langle e|) + \frac{\hbar|\Omega_2|^2}{4\Delta_2}(|g_2\rangle\langle g_2| - |e\rangle\langle e|)}_{=:H_{\text{AC}}} \\
 & - \frac{\hbar\Omega_R}{2} (|g_2\rangle\langle g_1| e^{-i(\Delta_{\text{eff}}t - \phi_{L,\text{eff}} - \phi_{\Omega,\text{eff}})} + \text{h.c.}), \quad (2.27)
 \end{aligned}$$

where the effective laser phase is defined as $\phi_{L,\text{eff}} = \phi_{L1} - \phi_{L2} + \pi$, the effective Rabi phase as $\phi_{\Omega,\text{eff}} = \phi_{\Omega1} - \phi_{\Omega2}$, and the effective detuning as $\Delta_{\text{eff}} = \Delta_1 - \Delta_2$. Furthermore, the effective Rabi rate, or Raman Rabi rate, is defined as

$$\Omega_R = \frac{|\Omega_1||\Omega_2|}{2\Delta_R}, \quad \text{where} \quad \frac{1}{\Delta_R} = \frac{1}{2} \left(\frac{1}{\Delta_1} + \frac{1}{\Delta_2} \right). \quad (2.28)$$

In this work the term Δ_R is referred to as Raman detuning. The first two terms of equation (2.27) are AC-Stark shifts between the ground states and the excited state since they are in the same form as equation (2.25). On the other hand, the last term has the same form as equation (2.17). We can transform H_{eff} using an appropriate unitary operator to eliminate the AC-Stark shift terms and absorb them into Δ_{eff} , bringing the whole Hamiltonian into the exact form as equation (2.17). Using the unitary operator $U = e^{-iH_{\text{AC}}t/\hbar}$, we arrive at the Raman Hamiltonian

$$\begin{aligned}
 H_R = & U^\dagger H_{\text{eff}} U + i\hbar \frac{dU^\dagger}{dt} U \\
 = & - \frac{\hbar\Omega_R}{2} (|g_2\rangle\langle g_1| e^{-i(\Delta_{\text{eff,AC}}t - \phi_{L,\text{eff}} - \phi_{\Omega,\text{eff}})} + \text{h.c.}), \quad (2.29)
 \end{aligned}$$

2.2 Light-atom interaction

where the AC-Stark shift-corrected effective detuning is defined as

$$\begin{aligned}\Delta_{\text{eff,AC}} &= \left(\Delta_1 + \frac{|\Omega_1|^2}{4\Delta_1} \right) - \left(\Delta_2 + \frac{|\Omega_2|^2}{4\Delta_2} \right) \\ &= (\omega_{L1} - \omega_{L2}) + \left(\omega_{g1} + \frac{|\Omega_1|^2}{4\Delta_1} \right) - \left(\omega_{g2} + \frac{|\Omega_2|^2}{4\Delta_2} \right).\end{aligned}$$

It is apparent now that equation (2.29) leads to a coherent population transfer with rate $\Omega'_R = \sqrt{\Omega_R^2 + \Delta_{\text{eff,AC}}^2}$ between the two ground states in terms of Rabi oscillations as described in equations (2.20) and (2.21). However, this result does not take the AC-Stark shift of laser 1 acting on $|g_2\rangle$ and $|e\rangle$ and the shift of laser 2 acting on $|g_1\rangle$ and $|e\rangle$ into account. This is due to the fact that these terms are not present in the Hamiltonian of equation (2.26).

Taking these interactions into account and also allowing for multiple excited states $|e_j\rangle$ with $\omega_{ej} > \omega_{g2} > \omega_{g1}$ (Λ -configuration) and $\omega_{ej} < \omega_{g1} < \omega_{g2}$ (V -configuration) leads to a more general and realistic expression. The AC-Stark shift-corrected effective detuning then turns into

$$\begin{aligned}\Delta_{\text{eff,AC}} &= (\omega_{L1} - \omega_{L2}) + \left(\omega_{g1} + \sum_j \text{sgn}(\omega_{ej} - \omega_{g1}) \left(\frac{|\Omega_{g1,ej}^{L1}|^2}{4\Delta_{g1,ej}^{L1}} + \frac{|\Omega_{g1,ej}^{L2}|^2}{4\Delta_{g1,ej}^{L2}} \right) \right) \\ &\quad - \left(\omega_{g2} + \sum_j \text{sgn}(\omega_{ej} - \omega_{g2}) \left(\frac{|\Omega_{g2,ej}^{L1}|^2}{4\Delta_{g2,ej}^{L1}} + \frac{|\Omega_{g2,ej}^{L2}|^2}{4\Delta_{g2,ej}^{L2}} \right) \right),\end{aligned}$$

while the Raman Rabi rate amounts to

$$\Omega_R = \left| \sum_j \begin{cases} \frac{(\Omega_{g1,ej}^{L1})(\Omega_{g2,ej}^{L2})^*}{2\Delta_{g(1,2),e(j,j)}^{L(1,2)}}, & \text{if } \omega_{ej} > \omega_{g2} \\ -\frac{(\Omega_{g1,ej}^{L2})(\Omega_{g2,ej}^{L1})^*}{2\Delta_{g(1,2),e(j,j)}^{L(2,1)}}, & \text{if } \omega_{ej} < \omega_{g1} \end{cases} \right|.$$

Analogous to section 2.2.1, the coherent population transfer in an experiment has again the rate $\Omega'_R := \sqrt{\Omega_R^2 + \Delta_{\text{eff,AC}}^2}$. The single-beam detunings, Raman detunings, and single-beam Rabi rates are respectively defined as

$$\begin{aligned}\Delta_{gk,ej}^{Ln} &= \omega_{Ln} - |\omega_{ej} - \omega_{gk}|, \\ \frac{1}{\Delta_{g(k,p),e(j,i)}^{L(n,m)}} &= \frac{1}{2} \left(\frac{1}{\Delta_{gk,ej}^{Ln}} + \frac{1}{\Delta_{gp,ei}^{Lm}} \right), \\ \text{and} \quad \hbar\Omega_{gk,ej}^{Ln} &= \begin{cases} \langle e_j | \vec{p} \cdot \vec{E}_n | g_k \rangle, & \text{if } \omega_{ej} > \omega_{g2} \\ \langle e_j | \vec{p} \cdot \vec{E}_n^* | g_k \rangle, & \text{if } \omega_{ej} < \omega_{g1} \end{cases}.\end{aligned}\tag{2.30}$$

The last equation showing the single-beam Rabi rate was assumed to come from electric dipole interactions but can be generalized to other interactions.

We can see that a criterion for resonance of the two laser fields 1 and 2 is that their frequency difference corresponds to the frequency difference of the two target levels while also accounting for all possible AC-Stark shifts. The experimentally measured Raman Rabi rate is then the result of an interference of all possible complex-valued single-beam Rabi rates. These rates emerge from the different Raman paths involving the intermediate states $|e_j\rangle$, which potentially accumulate different phases.

In practice, we would simplify the expression by eliminating so-called forbidden transitions that do not follow the selection rules of the electronic structure and those couplings with significantly large detunings. The selection rules for an electronic dipole transition include a change of the azimuthal quantum number $\Delta L = \pm 1$ and the change of the projection of the total angular momentum quantum number $\Delta m_J = 0, \pm 1$. Forbidden transitions are further characterized by significantly slower single-beam Rabi rates compared to the Rabi rates of allowed transitions.

In the experiments on the calcium-40 ion presented in this work, the higher ground level $|g_2\rangle$ is the $3^2D_{5/2}$ ($m_{5/2} = -1/2$) state, while the lower ground state $|g_1\rangle$ is either the $3^2D_{3/2}$ ($m_{3/2} = -1/2$) state or the $3^2D_{3/2}$ ($m_{3/2} = +3/2$) state. Taking the selection rules into account, we can identify that the main coupling contributions to the mentioned states arise from the states $4^2P_{1/2}$, $4^2P_{3/2}$, and all their Zeeman substructures. The sublevels of $4^2S_{1/2}$ are coupled less efficiently to the $3^2D_{3/2}$ and $3^2D_{5/2}$ states via electric quadrupole transitions.

2.2.3 Optical frequency comb Raman transition

The discussion in the previous section about a three-level system interacting with two laser fields can be generalized if we replace the two laser fields with an optical frequency comb, see figure 2.8. As established in equation (2.4), an optical frequency comb can be represented as the superposition of several continuous-wave (CW) lasers with temporal amplitudes $|\vec{E}_n|$, frequencies

$$\omega_n = \omega_{\text{CEO}} + n\omega_{\text{rep}},$$

and temporal phases

$$\varphi_n = \sum_{j=0}^{\infty} \frac{D_j}{j!} (\omega_n - \omega_c)^j,$$

where $n \in \mathbb{N}_0$. The angular frequency ω_{rep} is the repetition rate, the carrier-envelope offset frequency is denoted as ω_{CEO} , the laser's center frequency is ω_c , and D_j are the dispersion parameters discussed in sections 2.1.1 and 2.1.2. The temporal phases are equal to the spectral phases, and the collection of phases φ_n carries information about the dispersion of the laser. Based on equation (2.4), we can describe the optical frequency comb as

$$\vec{E}(\vec{r}, t) = \frac{1}{2} \sum_n \left(\vec{E}_n e^{i(\vec{k}_n \cdot \vec{r} - \omega_n t + \varphi_n)} + \text{c.c.} \right),$$

where n sums over all the comb teeth. The complex vector $\vec{E}_n = \vec{e} |\vec{E}_n|$ encodes the amplitude $|\vec{E}_n|$ of the individual CW components and the shared complex polarization

2.2 Light-atom interaction

vector $\vec{\epsilon}$, while the wave vector \vec{k}_n defines the propagation direction and wavelength of the optical frequency comb. Since each tooth is represented by a CW laser, each comb tooth pair can, in principle, drive a Raman transition. Dispersion specifies the phase relation between comb teeth. As we will see later, destructive interference due to the phases between two comb teeth can reduce the effective Raman Rabi frequency.

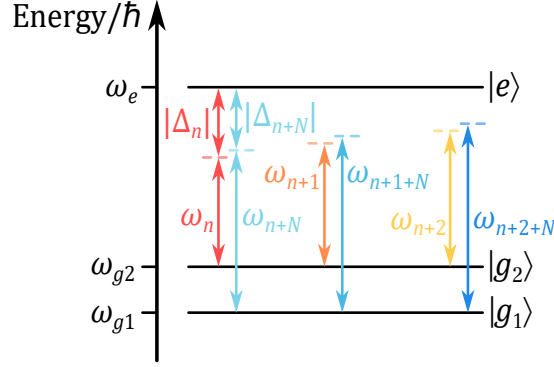


Figure 2.8: **Three-level system undergoing a Raman transition driven by an optical frequency comb.** This figure is similar to figure 2.7 with many more laser fields at regularly spaced frequencies $\omega_n = \omega_{\text{CEO}} + n\omega_{\text{rep}}$. If the energy difference between the two ground states $|g_1\rangle$ and $|g_2\rangle$ corresponds roughly to an integer multiple of the repetition rate ω_{rep} of the optical frequency comb, then a coherent Raman transition between the two ground states via the intermediate excited state $|e\rangle$ is possible with a strength proportional to the Raman Rabi rate Ω_R .

To arrive at an experimentally measurable Raman Rabi rate and AC-Stark shift compensated effective detuning, we can follow the same procedures as in sections 2.2.1 and 2.2.2. The steps include (i) applying the electric dipole approximation, (ii) defining the interaction energy between light and atom, (iii) defining the single-beam Rabi rates, (iv) expressing the total Hamiltonian, (v) treating the Hamiltonian in the interaction picture, (vi) performing the rotating wave approximation, (vii) following the procedure described by James and Jerke [91], (viii) transforming the Hamiltonian with a unitary to shift the AC-Stark shift expressions into the effective detuning, (ix) applying a final unitary transformation to eliminate the remaining time dependencies and irrelevant phases, and (x) solving the so generated effective Hamiltonian which takes the same form as equation (2.18).

We allow for intermediate states $|e_j\rangle$ with energies $\hbar\omega_{e_j} > \hbar\omega_{g_2} > \hbar\omega_{g_1}$ (Λ -configuration) and $\hbar\omega_{e_j} < \hbar\omega_{g_1} < \hbar\omega_{g_2}$ (V -configuration), where $\hbar\omega_{g_1}$ and $\hbar\omega_{g_2}$ are the two target eigenenergies of the isolated atom. Another assumption made is that there exists only a single integer multiplication factor N for which $N\omega_{\text{rep}}$ lies within the bandwidth of the optical frequency comb and fulfills $N\omega_{\text{rep}} \approx \omega_{g_2} - \omega_{g_1}$. Any bigger or smaller N is regarded as far off-resonant and is neglected in this derivation. In the case of our experiment, this detuning amounts to integer multiples of roughly 250 MHz.

The two relevant quantities emerging from this description are the AC-Stark shift-

corrected effective detuning

$$\Delta_{\text{eff,AC}} = N\omega_{\text{rep}} + \left(\omega_{g1} + \sum_{j,n} \text{sgn}(\omega_{ej} - \omega_{g1}) \frac{|\Omega_{g1,ej}^{L_n}|^2}{4\Delta_{g1,ej}^{L_n}} \right) - \left(\omega_{g2} + \sum_{j,n} \text{sgn}(\omega_{ej} - \omega_{g2}) \frac{|\Omega_{g2,ej}^{L_n}|^2}{4\Delta_{g2,ej}^{L_n}} \right), \quad (2.31)$$

and the Raman Rabi rate

$$\Omega_{\text{R}} = \left| \sum_{j,n} e^{i(\varphi_{n+N} - \varphi_n)} \begin{cases} \frac{(\Omega_{g1,ej}^{L_{n+N}})(\Omega_{g2,ej}^{L_n})^*}{2\Delta_{g(1,2),e(j,j)}^{L(n+N,n)}}, & \text{if } \omega_{ej} > \omega_{g2} \\ -\frac{(\Omega_{g1,ej}^{L_n})(\Omega_{g2,ej}^{L_{n+N}})^*}{2\Delta_{g(1,2),e(j,j)}^{L(n,n+N)}}, & \text{if } \omega_{ej} < \omega_{g1} \end{cases} \right|. \quad (2.32)$$

In an experiment, this optical frequency comb will induce coherent population transfer with a generalized Raman Rabi rate $\Omega'_{\text{R}} = \sqrt{\Omega_{\text{R}}^2 + \Delta_{\text{eff,AC}}^2}$, which, at resonance, is proportional to the intensity of the optical frequency comb. The definitions of the single-beam detunings $\Delta_{gk,ej}^{L_n}$, the Raman detunings $\Delta_{g(k,p),e(j,i)}^{L(n,m)}$, and the complex single-beam Rabi rates $\Omega_{gk,ej}^{L_n}$ are given in equation (2.30) if we substitute ω_{L_n} with ω_n .

The expression for the AC-Stark shift-corrected effective detuning of equation (2.31) shows again that this detuning is influenced by all possible AC-Stark shifts and that only pairs of comb teeth separated by $\omega_{n+N} - \omega_n = N\omega_{\text{rep}} \approx \omega_{g2} - \omega_{g1}$ contribute to driving a transition. The effectiveness of these contributions can be inferred from the Raman Rabi rate expression of equation (2.32). They are set by (i) the spectral amplitudes of the two teeth in each pair, encoded in the amplitudes of the single-beam Rabi rates, (ii) the phase differences of the Raman paths generated by the multiple intermediate states defined by the arguments of the single-beam Rabi rates, (iii) the Raman detunings, and (iv) the comb teeth pairs spectral phase differences $\varphi_{n+N} - \varphi_n$.

The spectral phase difference is set by the dispersion properties of the optical frequency comb. Possible destructive phase interferences lead to a reduction in Raman Rabi rate and thus efficiency. This motivates the need for dispersion compensation as introduced in section 2.1.2. Furthermore, having a broader spectral bandwidth of the optical frequency comb allows for driving transitions with a higher energy difference. Since the ultimate goal for our system is to drive rotational transitions in molecular ions, where such transition frequencies typically range from 10 GHz to 10 THz, it is advantageous to have as broad a bandwidth as possible since the rotational state transitions get larger with higher rotational quantum numbers. This motivates self-phase modulation-induced bandwidth broadening described in section 2.1.3.

In order to maximize the Raman Rabi rates of the transitions, it is important to understand how dispersion induced by the optical setup affects these rates. For this we can take equation (2.32) and assume that only one intermediate state is involved, eliminating the need to account for phase differences in different Raman paths and enabling us to

2.2 Light-atom interaction

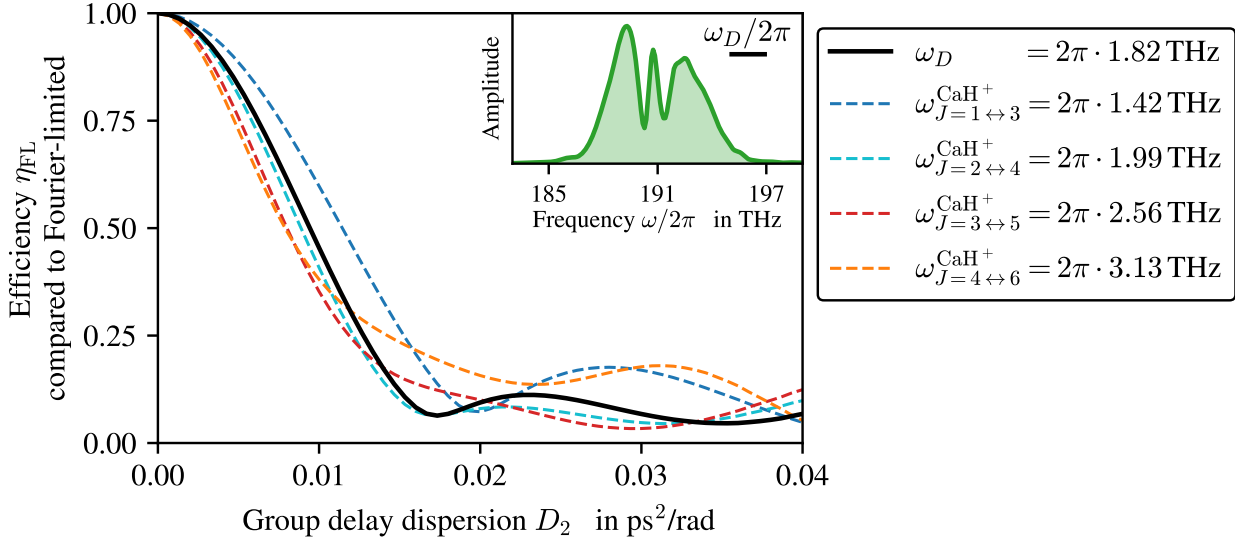


Figure 2.9: **Coupling efficiency due to group delay dispersion.** Using equation (2.33), we simulate the relative efficiency of Raman transitions η_{FL} driven by an optical frequency comb as a function of group delay dispersion D_2 , compared to a Fourier-limited field. The energy difference $\hbar\omega_D$ corresponds to the zero-field splitting between the two D -states of a calcium-40 ion, while $\hbar\omega_J^{\text{CaH}^+}$ represents rotational state differences in CaH^+ , where J is the rotational quantum number. The inset shows the Fourier-limited spectrum used for this simulation, which is based on the measured optical frequency comb (figure 3.3, final output). The relative efficiency oscillates due to the overlap of spectral peaks and phase interference caused by D_2 . The plot is symmetric around zero, unlike non-Fourier-limited pulses.

treat the single-beam Rabi rates as real valued. This simplification is justified because we are ultimately interested in ratios of Raman Rabi rates, as we will introduce efficiency quantities defined by these ratios.

Another useful approximation we can perform is to assume that neighboring Raman detunings $\Delta_{g_{(1,2),e}^{(j,j)}}^{L_{(n+N,n)}} - \Delta_{g_{(1,2),e}^{(j,j)}}^{L_{(n+N+1,n+1)}}$ have a negligible change compared to the single-beam detunings $\Delta_{g_{(1,2),e}^{(j,j)}}^{L_{(n+N,n)}}$, which is justified by the single-beam detunings being on the order of 100 THz while the neighboring Raman detunings change on the order of 100 MHz. This allows us to approximate $\Delta_{g_{(1,2),e}^{(j,j)}}^{L_{(n+N,n)}} \approx \Delta$ equal for all comb tooth pairs. With this, we can rewrite the Raman Rabi rate as

$$\Omega_{\text{R}}^{\text{sim}}(\varphi_n, N) = \left| \sum_n e^{i(\varphi_{n+N} - \varphi_n)} \frac{|\Omega_{g_{1,e}}^{L_{n+N}}| |\Omega_{g_{2,e}}^{L_n}|}{2\Delta} \right| \propto \left| \sum_n e^{i(\varphi_{n+N} - \varphi_n)} \frac{E_{n+N} E_n}{2\Delta} \right|,$$

where $E_n = |\vec{E}_n|$ are the amplitudes of the comb teeth. If we are only interested in relative efficiency changes of dispersion compared to a Fourier-limited optical frequency comb, we

can introduce the relative efficiency

$$\eta_{\text{FL}} = \frac{\Omega_{\text{R}}^{\text{sim}}(\varphi_n, N)}{\Omega_{\text{R}}^{\text{sim}}(0, N)} = \frac{|\sum_n E_{n+N} E_n e^{i(\varphi_{n+N} - \varphi_n)}|}{\sum_n E_{n+N} E_n}. \quad (2.33)$$

This equation is used to simulate the effects of dispersion for a given spectral envelope function. For example, the efficiency sensitivity of a Fourier-limited optical frequency comb with a measured spectral amplitude to added group delay dispersion is shown in figure 2.9.

Another option would be to compare the effect of the dispersion on a Raman transition caused by two far off-resonant and in-phase CW lasers with the same total power to the optical frequency comb. The total power of the optical frequency comb is $P_{\text{comb}} \propto \sum_n E_n^2$, the power of each CW laser is $P_{\text{CW}} = P_{\text{comb}}/2$, the corresponding amplitudes are $E_{\text{CW}} \propto \sqrt{P_{\text{CW}}}$, and the CW Raman Rabi rate is given by $\Omega_{\text{R}}^{\text{CW}} \propto E_{\text{CW}} E_{\text{CW}} / (2\Delta)$. This situation can be described by the relative efficiency

$$\eta_{\text{CW}} = \frac{\Omega_{\text{R}}^{\text{sim}}(\varphi_n, N)}{\Omega_{\text{R}}^{\text{CW}}} = 2 \frac{\Omega_{\text{R}}^{\text{sim}}(\varphi_n, N)}{\Omega_{\text{R}}^{\text{sim}}(0, 0)} = 2 \frac{|\sum_n E_{n+N} E_n e^{i(\varphi_{n+N} - \varphi_n)}|}{\sum_n E_n^2}. \quad (2.34)$$

Note that the single beam optical frequency comb can in principle be twice as efficient as a pair of CW lasers with the same total power. This is due to the fact that for the frequency comb, the full power can be used to drive each of the two Raman paths, while for the two CW lasers, each CW laser can only drive one path [45].

2.2.4 Ramsey interferometry and spin echo

Ramsey interferometry [93, 94] and the Hahn echo sequence [95], hereafter simply referred to as the spin echo sequence, are useful tools for extracting noise information from a quantum system and for decoupling it from certain types of noise [96]. In particular, these techniques help characterize dephasing noise, which refers to the loss of phase coherence in a quantum state due to fluctuations in the system's energy levels caused by environmental perturbations. Coherence, on the other hand, refers to the ability of a quantum system to maintain a well-defined phase relationship between its states, allowing for quantum interference. In the context of dephasing, such environmental perturbations cause individual quantum states within a set of experimental runs to accumulate different phases over time, leading to a reduction in overall coherence and thus limiting the interaction time with the ion. We will use the Ramsey and spin echo techniques to estimate the influence of low- and high-frequency dephasing noise on our ion-laser system. Extracting the dephasing timescale is important to identify possible noise sources. The noise could, for example, originate from laser fluctuations, magnetic field fluctuations, or other environmental noise. In this section, Ramsey and spin echo sequences are presented and modeled, including a dephasing noise description of a quantum system.

The typical Ramsey sequence consists of a $\pi/2$ -pulse whose length is $\pi/(2|\Omega|)$, where $|\Omega|$ is the Rabi rate. Then a free evolution time τ , followed by a second $\pi/2$ -pulse with a variable phase ϕ with respect to the first $\pi/2$ -pulse. By varying ϕ for a fixed τ and fitting

2.2 Light-atom interaction

the resulting graph, we extract the highest and lowest values, which define a quantity called the Ramsey contrast. Plotting the Ramsey contrast as a function of τ yields a decaying function from which the effects of noise on the system can be extracted.

However, in the single-beam setup used in this work, the optical frequency comb cannot perform a typical Ramsey sequence, and thus the sequence must be modified. This is because the setup involves a Raman transition where the two photons driving each $\pi/2$ -pulse cannot be individually controlled. Any phase ϕ between the first and second $\pi/2$ -pulses is canceled out, as the relevant quantity is the difference frequency between the two photons. As such, a phase shift ϕ cannot be introduced between the pulses, since any shift applied via an acousto-optic modulator affects both photons equally and thus cancels out in the two-photon process (see equation (2.27) and the definition of $\phi_{L,\text{eff}}$).

The modification of the Ramsey scheme involves detuning the optical frequency comb from the two-photon resonance and varying the waiting time τ , giving rise to decaying oscillations. However, if the detuning is too large, the Rabi oscillations lose contrast as less population is transferred. The detuning Δ_0 effectively induces a controlled time-varying phase $\Delta_0\tau$ between the first and second $\pi/2$ -pulses, as we will see later. Thus the envelope of this decaying oscillation corresponds to the mentioned Ramsey contrast. The decay constant is usually known as T_2^* time. It characterizes the typical dephasing timescale of the system, accounting for all dephasing noise sources, unlike the spin echo sequence, which mitigates certain types of noise.

Using the spin echo scheme, we can separate high-frequency (dynamic) from low-frequency (static) components of one or more noise sources by mitigating the low-frequency noise in a quantum system. This is done by modifying the Ramsey scheme again by applying a π -pulse halfway during the waiting time τ . This scheme leads to a decaying constant function with a dephasing time constant T_2 , which is typically larger than T_2^* .

The effects of the Ramsey and spin echo sequences can be modeled with the following two-level, field-free, and rotating frame Hamiltonian:

$$H = 0 |g\rangle \langle g| + \hbar\Delta(t) |e\rangle \langle e|.$$

Here $\Delta(t)$ represents a fluctuating detuning of the two-photon resonance frequency compared to the continuous-wave laser frequency. The fluctuations could, for example, be induced by laser fluctuations, magnetic field noise, or other dephasing-type noise sources. We model the fluctuating detuning with a constant average Δ_0 and a randomly fluctuating part $\sigma_\Delta(t)$ with zero mean and constant variance $\langle\sigma_\Delta^2\rangle$ as

$$\Delta(t) = \Delta_0 + \sigma_\Delta(t).$$

Applying the aforementioned sequences to a qubit prepared in the state $|e\rangle$ leads, for both the Ramsey and spin echo cases, to the following probability of detection in the excited state $|e\rangle$:

$$p_e(\tau) = \frac{1}{2} (1 + \langle \cos(\phi_{\text{tot}}(\tau)) \rangle), \quad (2.35)$$

where $\langle X \rangle$ represents the average value of a random variable X over a number of experimental runs. Further, the fluctuating phase $\phi_{\text{tot}}(\tau)$ in the Ramsey case is

$$\begin{aligned}\phi_{\text{tot}}^{\text{Ramsey}}(\tau) &= \int_0^\tau \Delta(t) dt \\ &= \Delta_0 \tau + \int_0^\tau \sigma_\Delta(t) dt \\ &=: \Delta_0 \tau + \phi_{\text{rand}}^{\text{Ramsey}}(\tau),\end{aligned}$$

while in the case of spin echo it is

$$\begin{aligned}\phi_{\text{tot}}^{\text{echo}}(\tau) &= \int_0^{\tau/2} \Delta(t) dt - \int_{\tau/2}^\tau \Delta(t) dt \\ &= \int_0^{\tau/2} \sigma_\Delta(t) dt - \int_{\tau/2}^\tau \sigma_\Delta(t) dt \\ &=: \phi_{\text{rand}}^{\text{echo}}(\tau).\end{aligned}$$

To proceed, we need to establish several assumptions. To start, it is assumed that the random variable $X = \phi_{\text{rand}}$ follows a Gaussian process, which is motivated by the Central Limit Theorem [97], as we can assume that the underlying phase fluctuations result from the accumulation of many independent and random contributions. Recalling that $\langle \cos(X) \rangle = \text{Re}\{\langle e^{-iX} \rangle\}$, and using the properties of the characteristic function from probability theory, we can then equate [98, ch. 1.2]

$$\langle e^{-iX} \rangle = e^{-\langle X^2 \rangle / 2}.$$

In both Ramsey and spin echo, inserting the above expressions into equation (2.35) leads to an expression containing a correlation function $\langle \sigma_\Delta(t_1) \sigma_\Delta(t_2) \rangle$. A second assumption we make is that this correlation function originates from stationary noise, as we do not consider noise that changes its properties over time. Consequently, the correlations depend only on the time difference between points and not on the absolute time. Another reasonable assumption is that the correlation function is even, as we do not consider noise that behaves differently under time reversal. The final assumption concerns the functional form of the correlation function, which we assume to decay exponentially, with a free parameter for the decay constant. This allows us to model limiting behaviors such as Markovian noise (or white noise) [99] and quasi-static noise [100]. Overall, this leads to the following correlation function

$$\begin{aligned}\langle \sigma_\Delta(t_1) \sigma_\Delta(t_2) \rangle &= \langle \sigma_\Delta(t_1 - t_2) \sigma_\Delta(0) \rangle && \text{(stationary noise)} \\ &= \langle \sigma_\Delta(t_2 - t_1) \sigma_\Delta(0) \rangle && \text{(even)} \\ &= \langle \sigma_\Delta^2 \rangle e^{-\gamma |t_1 - t_2|} && \text{(exponentially decaying noise)} \\ &=: C(t_1 - t_2),\end{aligned}$$

where γ is an unspecified free parameter that sets the noise correlation time scale.

2.2 Light-atom interaction

With this, we have derived a model of our noise sources to have exponentially decaying correlations. With this model, we can identify two limiting cases by adjusting the timescales. We can retrieve Markovian noise (or white noise) if we impose the condition $\gamma\tau \gg 1$, leading to a correlation function of the form $C(t) = \langle \sigma_\Delta^2 \rangle \delta(t) 2/\gamma$, where $\delta(t)$ is the Dirac delta distribution. We can also retrieve a quasi-static noise source by setting $\gamma\tau \ll 1$, then $C(t) = \langle \sigma_\Delta^2 \rangle$.

All of these assumptions lead to a common form of the excitation probability of the two-level system for both Ramsey and spin echo sequences. We retrieve

$$p_e(\tau) = \frac{1}{2} (1 + \cos(\phi_0(\tau)) e^{-\Gamma(\tau)}), \quad (2.36)$$

where the Ramsey case is specified by

$$\begin{aligned} \phi_0^{\text{Ramsey}}(\tau) &= \Delta_0 \tau \\ \Gamma^{\text{Ramsey}}(\tau) &= \frac{\langle \sigma_\Delta^2 \rangle}{\gamma^2} (e^{-\gamma\tau} + \gamma\tau - 1) \\ &\approx \begin{cases} \frac{\langle \sigma_\Delta^2 \rangle}{\gamma} \tau =: \frac{\tau}{T_2^*} & \text{for } \gamma\tau \gg 1 \text{ (Markovian/white noise)} \\ \frac{1}{2} \langle \sigma_\Delta^2 \rangle \tau^2 =: \left(\frac{\tau}{T_2^*}\right)^2 & \text{for } \gamma\tau \ll 1 \text{ (quasi-static noise)} \end{cases}, \end{aligned}$$

and the spin echo case by

$$\begin{aligned} \phi_0^{\text{echo}}(\tau) &= 0 \\ \Gamma^{\text{echo}}(\tau) &= \frac{2\langle \sigma_\Delta^2 \rangle}{\gamma^2} \left(e^{-\gamma\tau/2} + \gamma\frac{\tau}{2} - 1 \right) \\ &\approx \begin{cases} \frac{\langle \sigma_\Delta^2 \rangle}{\gamma} \tau =: \frac{\tau}{T_2} & \text{for } \gamma\tau \gg 1 \text{ (Markovian/white noise)} \\ \frac{1}{4} \langle \sigma_\Delta^2 \rangle \tau^2 =: \left(\frac{\tau}{T_2}\right)^2 & \text{for } \gamma\tau \ll 1 \text{ (quasi-static noise)} \end{cases}. \end{aligned}$$

As previously mentioned, the timescales T_2^* (Ramsey) and T_2 (spin echo) are typically used to characterize low- and high-frequency dephasing times, respectively. This can be demonstrated through an analysis using noise power spectral densities and filter functions, as shown in [96, 101–103], though this is not addressed here. Typically the relation $T_2^* < T_2$ holds due to the fact that the spin echo technique is insensitive to low-frequency noise.

The exact definitions of T_2^* and T_2 given above depend on the type of dominant noise inside the system, but always characterize a 1/e decay of the excitation probability as a function of the waiting time τ . These timescales are also called transverse relaxation times or phase coherence times [104]. For further context, there exists a timescale T_1 that quantifies the fundamental excited-to-ground-state decay time, also called the longitudinal relaxation process [104]. It is possible to identify the relation $T_2 < 2T_1$ with appropriate definitions; however, there are some special cases where this inequality does not hold [105].

In this work we quantify T_2^* and T_2 for our light-atom system involving an optical frequency comb and a calcium-40 ion. To handle the measured data, we can adapt

equation (2.36) to a more realistic model by allowing for a variable offset $c \in [0, 1]$ and a variable amplitude $A \in [0, 2 \min\{c, 1 - c\}]$ set by imperfections in the system, then

$$p_e(\tau) = \frac{A}{2} \cos(\phi_0(\tau)) e^{-\Gamma(\tau)} + c. \quad (2.37)$$

Experimental setup and optical frequency comb characterization

This chapter builds on the theoretical concepts presented in chapter 2 and demonstrates how they were applied in practice. The optical setup of the frequency comb is presented. We also characterize the optical frequency comb's parameters, such as power and group delay dispersion, at several stages. The first part of section 3.1 discusses the optical setup ranging from the generation of the optical frequency comb to its amplification, while the second part of section 3.1 presents the setup that was created in the framework of this master's thesis, ranging from post-amplification to focusing onto the location of a trapped calcium-40 ion. The latter setup broadens the spectrum of the optical frequency comb via self-phase modulation using a highly nonlinear fiber, introduces amplitude modulation of the optical frequency comb light using an acousto-optical modulator, implements dispersion compensation via a normal fiber, and describes the light delivery to the trapped ion. Section 3.2 presents the results of more in-depth optical frequency comb characterization, e.g., temporal and spectral features and the power response to control units. Note that frequencies will be represented as linear frequencies f instead of angular frequencies $\omega = 2\pi f$ from this chapter onward.

3.1 Optical setup

The main focus of this work is the optical frequency comb. It is a commercial system from Menlo Systems [106] (FC1500), and the main components are drawn in figure 3.1 under the blue box labeled comb baseplate. This system has been used in the past by another research group; see, for example, [88, 107–110]. Information about the comb generation can be found in greater detail in [110, ch. 5.1] or the Menlo manual [111].

The optical frequency comb is generated in the M-Comb module and involves a fiber ring resonator including some free-space elements, as expanded upon later. The laser is generated using passive mode locking, as introduced in section 2.1.4. The cavity is formed by the circular path of the fiber ring and a mirror mounted on a piezoelectric mount. A polarizing beam splitter (PBS) and quarter-waveplate in front of the piezoelectrically-actuated mirror serve to guide the linearly polarized light into the path that completes the ring resonator. An optical isolator prevents any significant back reflection from traveling back into the cavity.

An erbium-doped fiber (Er^{3+}) inside the fiber ring acts as the gain medium, which

amplifies the generated optical frequency comb (erbium-doped fiber amplifier or EDFA, see [112]). The energy necessary for amplification is provided by a pump diode laser that co-propagates with the generated frequency comb light.

Passive mode-locking can be achieved using the two waveplate pairs in front of each fiber coupler. When the waveplate pairs compensate for nonlinear polarization rotation in the fiber ring, minimal light is lost through the output coupler (a second PBS) at peak intensity, allowing the system to operate in a mode-locked state. In this sense the waveplates, the output PBS, and the fiber ring act as the modulation element (saturable absorber) introduced in section 2.1.4. The waveplates can also be set enable continuous-wave operation.

The remaining elements consist of the free-space optics that are used for adjusting and stabilizing the repetition rate and the carrier-envelope offset frequency. The mirror with the piezoelectric mount is used to modulate the length of the cavity and controls the repetition rate. Additionally, an electro-optical modulator is used for faster (but smaller) control of the repetition rate. The stepper motor-powered wedge is used to coarsely set the carrier-envelope offset frequency by inducing a phase shift depending on the current thickness of the wedge. Fine-tuning is achieved with adjustment of the pump diode current.

The system uses an aforementioned PBS to function as an output coupler, reflecting part of the light within the cavity to an output port. At this point the optical frequency comb has a pulse length of 74 fs, a repetition rate of about 250 MHz, a carrier-envelope offset frequency of about 20 MHz, a center wavelength around 1570 nm (or 191.0 THz), and a spectral bandwidth of 45 nm (or 5.5 THz).

Part of this light is separated by a non-polarizing beam splitter and directly measured by a fast photodiode to monitor the repetition rate. The rest of the light is fed into a 1:4 splitter. Two paths are irrelevant for this thesis as they are not used. These paths produce 1068 nm light and visible second harmonic light for external white-light continuum generation (HMP1068 and M-VIS modules, respectively). A third path goes into the M-Phase module, which is responsible for monitoring the carrier-envelope offset frequency. This module splits the comb into two branches, the second harmonic is generated in one, and the white-light continuum is generated in the other. Both branches are then recombined and generate a beat by interfering with each other. This beat is used to measure and stabilize the carrier-envelope offset according to equation 2.10. The fourth path, here called the experiment path, ultimately reaches the trapped ion.

The experiment path goes through a stage of optical intensity pre-amplification (EDFA) controlled by the AC-1550 electronic control module. The power of the comb is amplified from about 0.26 mW to 26 mW. The following description outlines a setup for chirped pulse amplification [69] capable of amplifying the light up to 2.5 W. A 70 m long stretcher fiber with a group velocity dispersion (GVD) of $53.8 \text{ fs}^2/(\text{mm rad})$ (or $-41 \text{ ps}/(\text{nm km})$) introduces a group delay dispersion (GDD) of $3.77 \text{ ps}^2/\text{rad}$ (or $-2.87 \text{ ps}/\text{nm}$), stretching the pulse in time to about 100 ps. The light then passes through an intermediate pre-amplifier (EDFA) from Keopsys (CEFA-L-PB-LP-PM), which amplifies the light to about 100 mW.

The temporal pulse then is further stretched in time by a reflective chirped fiber Bragg grating (CFBG, TeraXion TPSR-1575), introducing another $13.05 \text{ ps}^2/\text{rad}$ (or $-9.95 \text{ ps}/\text{nm}$)

3.1 Optical setup

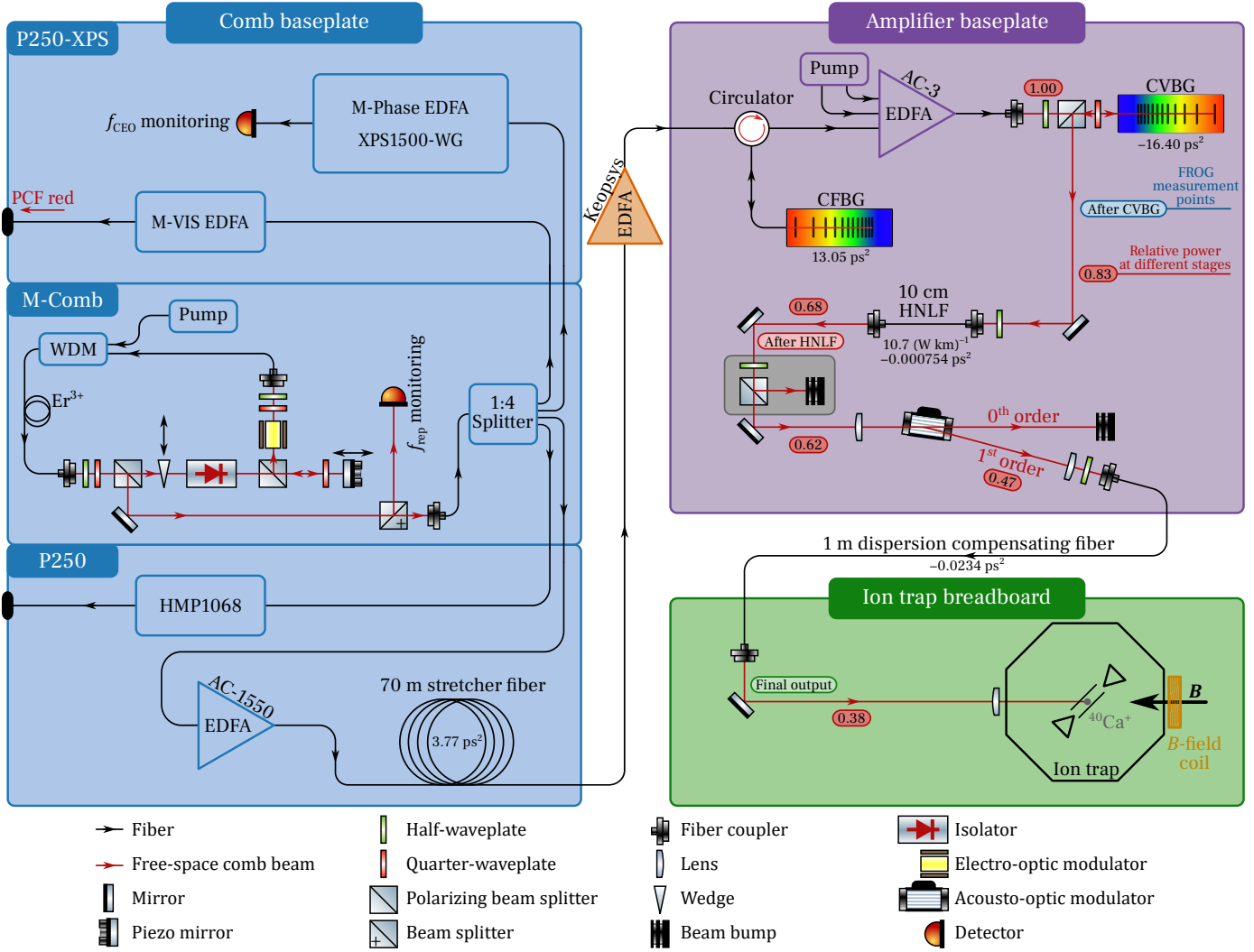


Figure 3.1: **Optical setup.** The setup is distributed between three locations: the comb baseplate, the amplifier baseplate, and the ion trap breadboard. The comb baseplate generates the passively mode-locked optical frequency comb (M-Comb module). On the amplifier baseplate, the comb is amplified up to 2.5 W using chirped pulse amplification [69], the spectrum is broadened using self-phase modulation, and dispersion is compensated. The light is delivered to the calcium-40 ion on the ion trap breadboard. The three blue, red, and green colored points described as “FROG measurement points” indicate where the data of figure 3.3 was taken. See the main text for more details.

WDM: wavelength division multiplexer, EDFA: Erbium (Er^{3+}) doped fiber amplifier, CFBG: chirped fiber Bragg grating, CVBG: chirped volume Bragg grating, HNLF: highly nonlinear fiber.

of GDD. At this point the pulse is stretched sufficiently (to about 450 ps) that its peak intensity does not damage the gain medium of the following amplification stage (EDFA) controlled by the AC-3 electronic control module. The AC-3 module also contains two

sources of pump light at a wavelength of ~ 975 nm, enabling the amplification of the optical frequency comb up to 2.5 W.

The light then enters a free-space stage including a temporal compression, which is achieved by a chirped volume Bragg grating (CVBG). The CVBG provides anomalous GDD of about -16.40 ps²/rad (or 12.5 ps/nm), which, together with the stretcher fiber, the CFBG, and remaining dispersion throughout the fibers of the system, produces a near transform-limited pulse by eliminating the accumulated GDD. The pulse now has a duration of 745 fs, a center wavelength of 1572 nm (or 191 THz), and a bandwidth of about 8 nm (or 1.0 THz). The temporal and spectral shapes are shown in the top part of figure 3.3. As the amplifiers only amplify light efficiently over a narrow gain profile, the bandwidth is reduced through each amplification stage in a phenomenon known as gain narrowing [113]. This completes the first part of the setup, from which this thesis work built on. This first part was previously used in other experiments, as cited in the beginning of this section.

The second part of the setup was built during this master’s thesis work. It aims to broaden the spectrum of the optical frequency comb, compensate the dispersion to recover a Fourier-limited pulse, and align it to a calcium-40 ion in the trap. Using this setup, we demonstrate quantum control via Raman transitions between states with energy differences that lie within the bandwidth of the light. Concretely, we achieve a bandwidth of about 5.3 THz to drive a D -level transition on a calcium-40 ion whose energy difference is about 1.8 THz.

The first stage of this new setup is the polarization-maintaining highly nonlinear fiber (HNLF, Thorlabs PMHN5), responsible for self-phase modulation (SPM) and consequential spectral broadening. The fiber has a nonlinear coefficient of $\gamma = 10.7$ (W km)⁻¹ and a mode field diameter of 4 μ m. It has a GVD of -7.54 fs²/(mm rad) (or 5.75 ps/(nm km)) and a length of 10 cm leading to a GDD of -754 fs²/rad (or 0.575 fs/nm). However, the SPM process itself also introduces dispersion of various orders. The temporal and spectral properties of the optical frequency comb at this stage can be seen in the middle row of figure 3.3. A pulse duration of 635 fs and a spectral bandwidth of 41 nm (or 5.1 THz) were measured.

After this stage, a half-waveplate and polarizing beam splitter combination was introduced (gray box in figure 3.1) to control the output power while holding the power injected into the HNLF constant, as the power defines the light’s spectral shape. However, as we noticed after the experiment, we observed that for different settings of the half-waveplate, the output spectrum changed. It turned out that this stage filtered out certain spectral components since the SPM process was effectively polarization-dependent due to the elliptical geometry of the polarization-maintaining core in the HNLF. Due to the short length of the HNLF (10 cm), it was not possible to align the polarization of the comb light to the fibers fast or slow axis since the transmitted power and polarization of the comb light were hardly affected by misalignment. As the effectiveness of SPM is different for the fast and slow axes of the fiber, the projected polarization components of the comb light onto the fast and slow axes experienced different amounts of SPM. As such, this half-waveplate and polarizing beam splitter combination stage would be better to be

3.2 Characterization of the optical frequency comb

removed as it introduces unpredictable filtering of the spectrum. The changes in the spectral shape due to different rotations of the half-waveplate are shown in appendix D.1.

The ability to regulate power using the half-waveplate and polarizing beam splitter combination can be replaced by the next element in the beam path: the acousto-optical modulator (AOM) used for remotely switching the optical frequency comb on and off. The AOM (G&H 3080-197) diffracts some of the light along a different path. This is done by feeding the AOM an 80 MHz signal at a radio frequency (RF) power of 3.5 W. Lowering this RF power also lowers the optical power sent through the first-order diffraction beam, as later shown in figure 3.2b.

If the AOM is switched on, the optical frequency comb is sent through a 1 m long normal fiber (Thorlabs P1-1550PM-FC-1), here referred to as dispersion compensating fiber, used for bringing the light close to transform-limited and also guiding it on the optical table with the ion trap. The fiber has a GVD of $-23.4 \text{ fs}^2/(\text{mm rad})$ (or $17.86 \text{ ps}/(\text{nm km})$) and thus introduces a GDD of $-23400 \text{ fs}^2/\text{rad}$ (or $17.86 \text{ ps}/\text{nm}$).

Dispersion compensation can be achieved using the earlier described CFBG. Using the software that controls the CFBG, we can further fine-tune dispersion, as it can slightly change GDD and third- and fourth-order dispersion. The tunable range of the GDD is $\pm 0.0584 \text{ ps}^2/\text{rad}$. The tunable ranges of the different dispersion orders are not independent from each other, as adjusting one setting sets different limits for the other settings. The control provided by the CFBG is crucial for achieving near-Fourier-limited pulses, as the system was observed to be particularly sensitive to the tuning range of the CFBG's fourth-order dispersion setting. Optimizing the dispersion orders using the CFBG control software leads to the final temporal and spectral shape shown at the bottom of figure 3.3. The pulse duration is shortened to 115 fs, and the final bandwidth is about 42 nm (or 5.3 THz).

The 1 m fiber terminates in a fiber coupler whose lens is set to be diverging to expand the beam size for a tighter focus. A second lens with a focal length of 125 mm collects the diverging beam and focuses it on the site of the ion in the trap, achieving a theoretical waist diameter of $40 \mu\text{m}$ on the ion. As a note, the waist could have been measured by varying the end-cap voltages of the trap such that the potential well that traps the ion changes its location. By measuring the drop in Rabi rate, an estimate of the waist can be extracted. However, this measurement was not performed.

The propagation direction of the optical frequency comb light was aligned with the direction of the magnetic field (B -field) experienced by the ion. As the light was linearly polarized, only σ^+ , σ^- , or $\sigma^+ + \sigma^-$ transitions can be driven on the Zeeman substructure of the calcium ion, leading to a restricted change in total angular momentum projection quantum number of $m_J = 0, \pm 2$.

3.2 Characterization of the optical frequency comb

The optical frequency comb setup presented in this work was characterized at various stages. The characterization includes the optical output power as a function of the RF power into the AOM and the AC-3 amplifier. Additionally, the frequency and temporal

structure of the comb are obtained via a technique called frequency resolved optical grating (FROG) [114, 115, ch. 9.4.4.].

The response of the laser power to the AC-3 control unit and power delivered to the of the amplitude modulating AOM are discussed first. A setting on the AC-3 controls how much pump light power is provided to the amplification stage. This setting can be set on a percent scale. However, the unit is prone to damage if operated beyond 50% as the fibers within the unit burn and break if too much pump light is sent through them. The catastrophic consequences of operating the unit at above 50% are documented in appendix B. The average free-space optical frequency comb power P_{FS} is measured right before the CVBG element. The nonlinear response of how the pump light increases the output power P_{FS} of the optical frequency comb as a function of the AC-3 setting as shown in figure 3.2a.

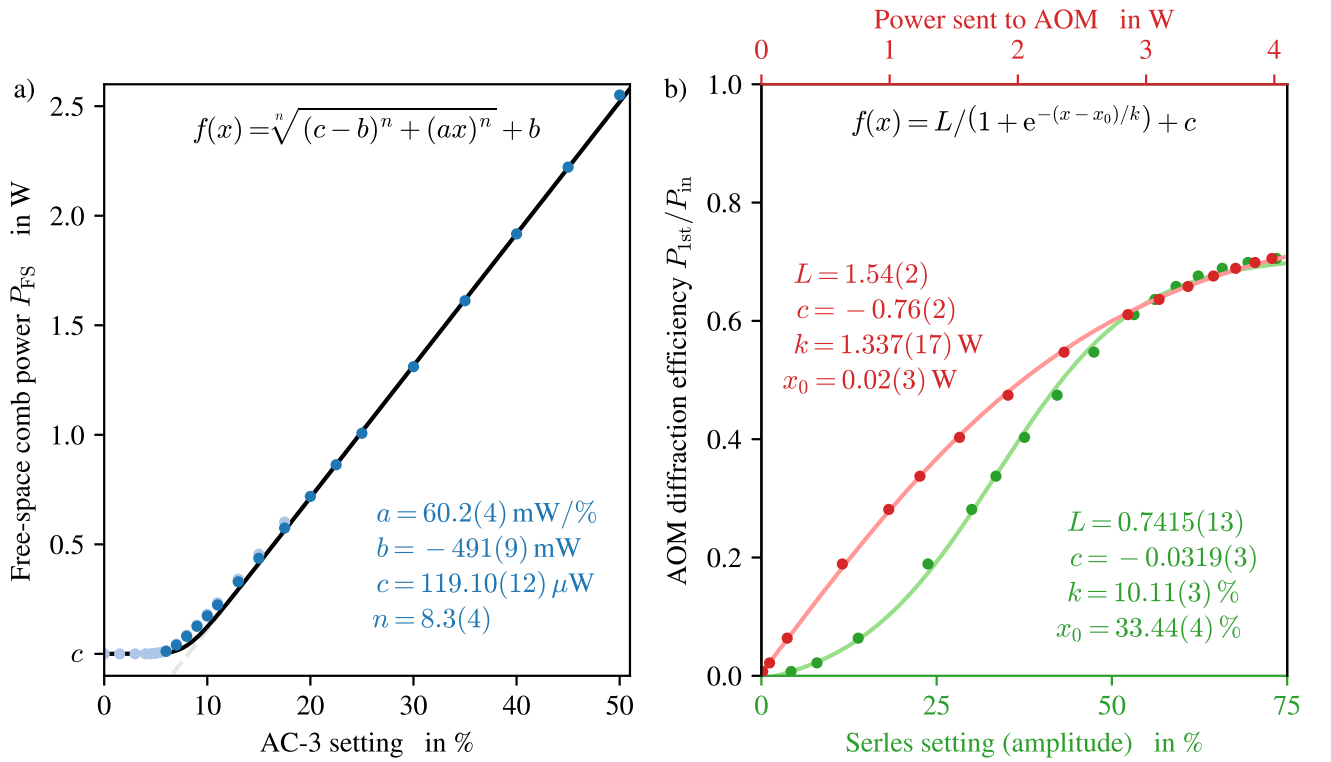


Figure 3.2: **Power characterization of the optical frequency comb.** (a) Optical frequency comb power measured after the first fiber coupler on the amplifier baseplate vs. AC-3 module setting. Light blue and dark blue data points correspond to measurements from Thorlabs S132C and S425C, respectively. An empirical fit was applied, where the parameters a and b were extracted from a linear fit of the last data points (gray dashed line), the offset c was set to the 0% value, and n was fitted using a generalized hyperbola model. (b) The same data is shown with different x -axes, representing the first-order diffraction efficiency of the comb light from the AOM vs. RF power (red) or the amplitude setting on the Serles software (green). The data was measured with the Thorlabs S132C photodiode. A logistic function was fitted to both.

3.2 Characterization of the optical frequency comb

We can also control how much RF power is provided to the amplitude modulating AOM via the control software Serles developed by AQT [116]. The resulting optical power of the first-order beam $P_{1\text{st}}$ after the AOM compared to the input optical power P_{in} into the AOM, also known as diffraction efficiency, as a function of the setting in Serles is shown in figure 3.2b. On a second horizontal scale, the Serles setting is translated into the RF power of the 80 MHz signal fed into the AOM. An optimally aligned setup would have a maximum at a diffraction efficiency of $P_{1\text{st}}/P_{\text{in}} = 0.8$, but this was not achieved during the measurement of this data. On all the plots of figure 3.2, phenomenological fit functions were used to estimate the evolution of the data.

As mentioned in the beginning of this section, the FROG technique [114, 115, ch. 9.4.4.] was used to extract temporal and spectral profile information of the optical frequency comb and subsequently broadened light. The FROG setup involves an autocorrelator, where the pulsed laser beam is split into two paths where one is directed through a variable time delay stage. The two arms are focused on a second harmonic generating crystal. The second harmonic light is then fed into a spectrometer. The variable time delay stage can be continuously modulated. By recording a spectrum at each increment of the time delay, the FROG setup measures a three-dimensional data set consisting of the second-harmonic signal as a function of time delay and frequency called a spectrogram. This data gives the full temporal and spectral information of the analyzed light [115, ch. 9.4.4.]. As a side note, this technique can also be extended by overlapping the laser pulse to be analyzed with a known reference beam and generating a sum-frequency beam. In this case the technique is known as XFROG (standing for cross-FROG).

The FROG traces were recorded using a commercial product from Mesa Photonics (FROGscan) at various stages of the setup as mentioned throughout section 3.1. The traces after the CVBG, the HNLF, and the dispersion compensating 1 m fiber are shown in figure 3.3. The data at the final output stage was recorded after optimizing the dispersion settings on the CFBG such that the optical frequency comb was close to the Fourier limit.

Compared to the initial optical frequency comb details after the CVBG, the temporal pulse shape after the HNLF did not significantly change; however, its temporal phase did, as demonstrated by the difference in instantaneous frequency of the pulses. Due to the influence of SPM, the emergence of the typical instantaneous frequency shape as described in equation (2.9) and figure 2.3 is observed. This chirping of the temporal phase caused the spectral envelope to significantly increase from 1 THz to 5.1 THz, showing the emergence of the typical oscillatory structure caused by SPM.

The increase in the bandwidth of the optical frequency comb without a corresponding decrease in pulse duration indicates that the laser is no longer Fourier-limited after passing through the HNLF. Once the laser passes through the dispersion compensating fiber (i.e., the final output), the pulse duration decreases significantly from 635 fs to 115 fs, as the dominant dispersion contributions are compensated. While the fiber does not significantly alter the spectral envelope, it modifies the spectral phase enough to compress the pulse in time. Dispersion is challenging to fully compensate, as evidenced by the curvature of the spectral phases in all data plots, which indicate the presence of dispersion.

It is important to note that the laser is sensitive to the changes in fourth-order dispersion D_4 tunable by the CFBG. Strong side lobes (pre- and post-pulses) can emerge if D_4 is

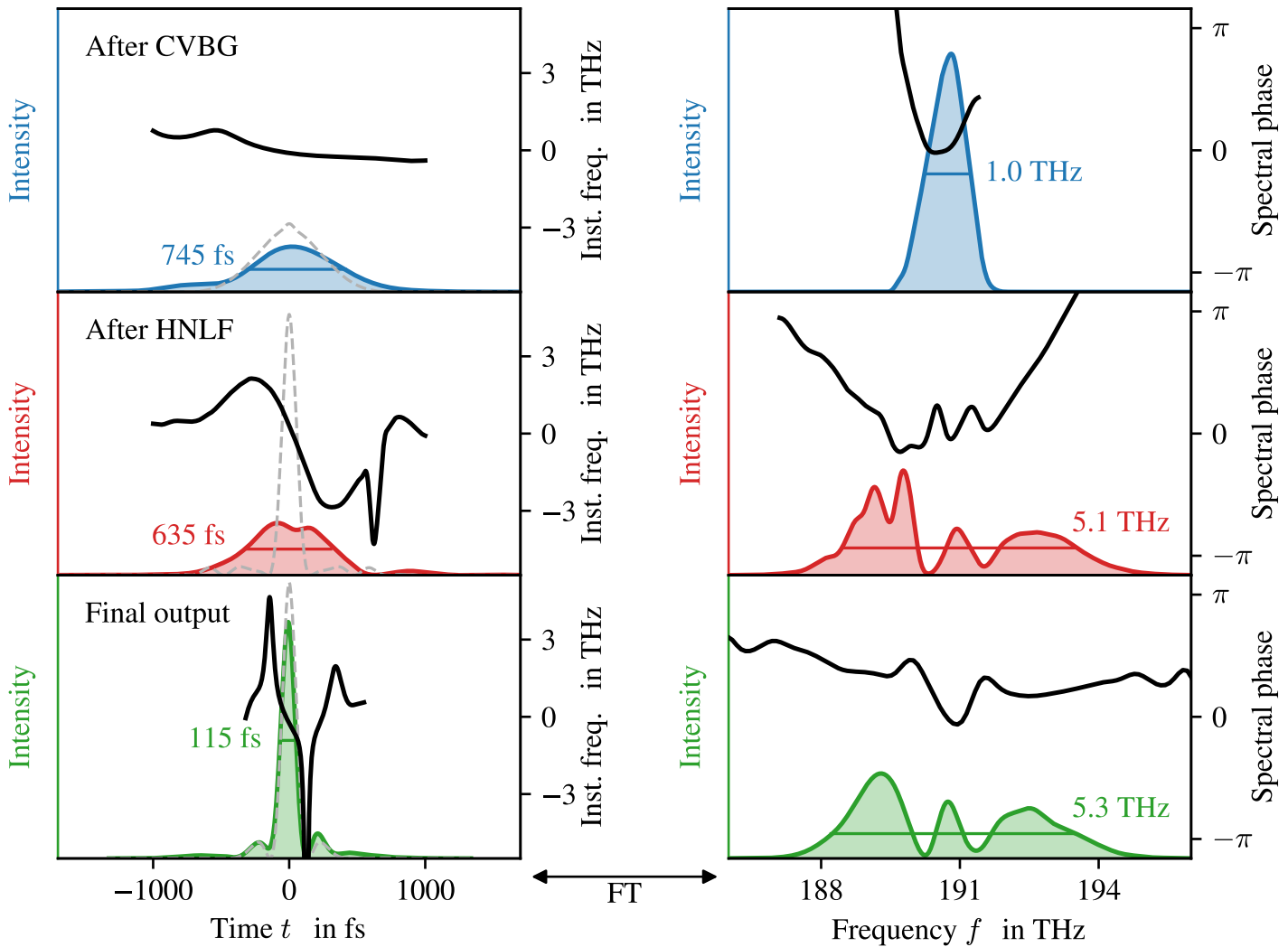


Figure 3.3: **Temporal and spectral characterization of the optical frequency comb at different stages.** Referring to figure 3.1, FROG measurements of the optical frequency comb have been performed after the chirped volume Bragg grating (CVBG, top, blue), after the highly nonlinear fiber (HNLF, center, red), and at the final output on the ion trap breadboard after dispersion compensation (bottom, green). For the time domain, the colored curves show the temporal intensities and the dashed gray lines show the Fourier-limited pulses with the same spectrum. The black curves show the instantaneous frequency (inst. freq.) of the measured data. For the frequency domain, the colored curves show the spectral intensities and black curves show the spectral phases. The shown temporal widths are at half of the maximum intensity while the spectral widths are shown for selected points. The widths are indicated by horizontal lines. A center frequency of 190.7 THz corresponds to a wavelength of 1572 nm. FT: Fourier transformation.

3.2 Characterization of the optical frequency comb

not set correctly. Furthermore, the laser is less sensitive to the changes in group delay dispersion D_2 and third-order dispersion D_3 tunable by the CFBG. This could be a result of soliton behavior, where pulses preserve their shape during propagation through a medium because of the interplay between dispersion and nonlinearity [71, ch. 5].

Furthermore, the FROG trace measured after the HNLFF was compared to a simulation that used the py-fmas package [74], see section 2.1.3, as well as the FROG trace taken before the HNLFF. This comparison is shown in figure 3.4.

General features overlap qualitatively. However, the simulated spectrum is narrower than what was measured. It seems as if the measured high-frequency lobe may be shortened in intensity when compared to the simulated data. The nonlinear phenomenon of self-steepening [71, ch. 4.3.1] causes higher frequencies to evolve differently than lower frequencies, which could explain this discrepancy. Thus, one possible explanation of the discrepancy between the simulated and measured data is that the simulation does not take self-steepening as strongly into account as it actually occurs. The reason for this could lie in the usage of wrong simulation parameters, such as slightly different dispersion parameters of the input light and wrong parameters of the Raman response function, which is used in the simulation to include the delayed Raman contributions [71, ch. 2.3.2].

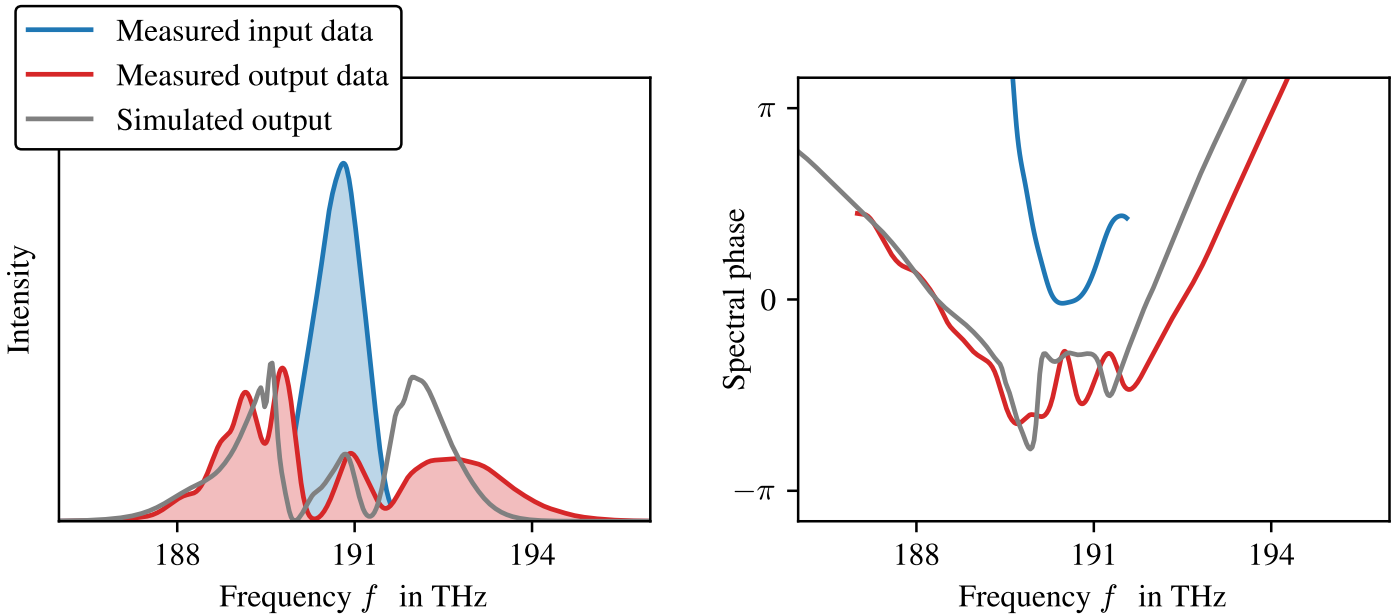


Figure 3.4: **Simulation of self-phase modulation.** Spectra of the optical frequency comb were measured before the highly nonlinear fiber (blue, input) and after (red, output). Using the input data as a starting point of the self-phase modulation simulation using py-fmas, the black line shows the simulated output data with the same relevant parameters (10 cm fiber length, 1.18 W transmitted optical power, nonlinear coefficient of $\gamma = 10.7 (\text{W km})^{-1}$, and appropriate dispersion of the fiber).

Spectroscopy results

After presenting the principles of optical frequency combs in Chapter 2 and demonstrating how the commercial optical frequency comb was adapted for Raman experiments in Chapter 3, we now turn to applying it in new experiments. In our research group's main setup [25], we are able to trap, cool, and manipulate calcium-40 ions using a Paul trap and an arrangement of appropriate lasers. This chapter presents measurements of Raman transitions induced by the optical frequency comb on a single trapped calcium-40 ion.

To execute such measurements, a general experimental **sequence** was implemented. However, section 4.1 uses a variation of this **sequence**, consisting of:

1. loading of a single calcium-40 ion into the Paul trap,
2. ground state cooling of the ion to the $4^2S_{1/2} (m_{1/2} = -1/2)$ state using Doppler and sideband cooling [52] techniques,
3. state preparation into the $3^2D_{5/2} (m_{5/2} = -1/2)$ state by population inversion using a resonant 729 nm laser,
4. driving a $3^2D_{5/2} \leftrightarrow 3^2D_{3/2}$ transition using the optical frequency comb where the used Zeeman substates used for transitions were either between $m_{5/2} = -1/2 \leftrightarrow m_{3/2} = -1/2$ or $m_{5/2} = -1/2 \leftrightarrow m_{3/2} = +3/2$, and
5. transferring the population of the $3^2D_{3/2}$ state into the $4^2S_{1/2} \leftrightarrow 4^2P_{1/2}$ cycling transition using continuous-wave resonant 866 nm and 397 nm lasers for readout.

Each sequence produced a binary outcome: a bright ion or a dark ion. The former corresponds to a successful projection of the state population from the $3^2D_{5/2}$ state into the $3^2D_{3/2}$ via the optical frequency comb, since this population is transferred into the $4^2S_{1/2} \leftrightarrow 4^2P_{1/2}$ cycling transition due to the 866 nm laser. On the other hand, a dark ion implies that the optical frequency comb either did not transfer any population or cycled back to the $3^2D_{5/2}$ state, therefore it is also not transferred into the cycling transition.

A single result for each experimental setting consists of the collection of outcomes gathered from repeating the described **sequence** $N_{\text{rep}} = 100$ times. An estimate of the actual population (or mean excitation) $p_{5/2}$ in the $3^2D_{5/2} (m_{5/2} = -1/2)$ state can be found using the number of detected dark ions n_{dark} during N_{rep} trials using

$$p_{5/2} = \frac{n_{\text{dark}}}{N_{\text{rep}}}.$$

4.1 Alignment using induced AC-Stark shift

An estimate for the uncertainty $\alpha_{p,5/2}$ in each retrieved $p_{5/2}$ value can be derived from binomial statistics and amounts to

$$\alpha_{p,5/2} = \begin{cases} \sqrt{N_{\text{rep}}}, & p_{5/2} \notin \{0, 1\} \\ 1/(N_{\text{rep}} + 2), & p_{5/2} \in \{0, 1\} \end{cases}.$$

The first case is also known as quantum projection noise [117], and the second case is derived from Laplace's Rule of Succession and avoids a diverging weight factor $\alpha_{p,5/2}^{-2}$ for $p_{5/2} = 0$ and $p_{5/2} = 1$ used in regression routines.

Section 4.1 describes the alignment process of the optical frequency comb light on the ion and reports the induced AC-Stark shift on a resonant 729 nm laser transition. Section 4.2 shows typical transitions between the $3^2D_{5/2} \leftrightarrow 3^2D_{3/2}$ states and infers the Landé g-factor of the $3^2D_{3/2}$ state from the results, and section 4.3 uses Ramsey techniques to characterize phase noise in the system. The time frame used for taking the measurements in this section (and appendix D) was from the 18th till the 28th of July 2024.

4.1 Alignment using induced AC-Stark shift

A rough alignment of the optical frequency comb beam through the ion trap is straightforward. However, such transmission through the trap does not guarantee a significant overlap of the beam with the trapped ion. To maximize the overlap, one can use a technique that involves tracking the transition frequency of a certain transition using Rabi spectra as it is modified due to the induced AC-Stark effect, see section 2.2.1. This work uses the transition between the $4^2S_{1/2} (m_{1/2} = -1/2)$ and the $3D_{5/2} (m_{5/2} = -1/2)$ state.

This technique requires being able to measure a resonant transition, whose transition frequency is denoted as f_{729} . In our case the transition is driven by a 729 nm laser. Application of the optical frequency comb light disrupts the resonant transition proportionally to the local intensity of the comb light on the ion, see equation (2.24). This disruption manifests as a shift f_{AC} with respect to the transition frequency f_{729} due to the AC-Stark effect. Maximizing the shift on the transition frequency $f_{729} + f_{\text{AC}}$ indicates an optimized overlap of the comb light with the ion.

By continuously applying the experimental **sequence** described in the beginning of chapter 4, but omitting the step of driving $3^2D_{5/2} \leftrightarrow 3^2D_{3/2}$ transitions using the optical frequency comb, the probed transition frequency can be tracked in real time. As a note, this is a usual Rabi spectroscopy method used for optical clocks [118]. Simultaneously applying an approximately aligned optical frequency comb will result in a shift $|f_{\text{AC}}| > 0$ of the probed transition frequency f_{729} . One can then update the frequency f_{729} to be resonant again by adjusting it to $f_{729} + f_{\text{AC}}$. This is done to further track changes in the new f_{729} frequency induced by fine-adjusting the alignment of the optical frequency comb. By iterating these steps, one can maximize f_{AC} and thus optimize the overlap of the optical frequency comb light on the ion. The result of this process is displayed in figure 4.1.

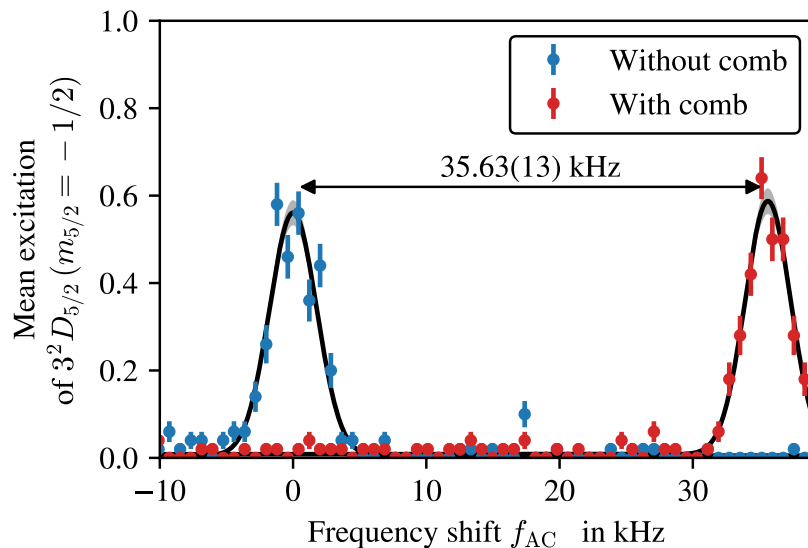


Figure 4.1: **AC-Stark shift induced by the optical frequency comb on a 729 nm transition.** Two data sets have been measured by varying a resonant 729 nm transition frequency on the calcium ion; one while having the optical frequency comb turned off (blue) and one while having it on simultaneously with the 729 nm light (red). The shift in transition frequency is the AC-Stark shift induced by the optical frequency comb.

4.2 Measurements of Raman transitions and calcium-40 $3^2D_{3/2}$ Landé g -factor

Using the aligned optical frequency comb and the general experimental [sequence](#) laid out in the beginning of [chapter 4](#), we measured Rabi oscillations and Rabi spectra as explained in [sections 2.2.1 and 2.2.3](#). This section presents the principal results of this work, presenting the characterization of typical Rabi frequencies, linewidths, optical frequency comb-induced AC-Stark shifts, and ultimately the extraction of the Landé g -factor of the $3^2D_{3/2}$ state.

The first hurdle is to find the Raman resonance frequency by tuning the comb's repetition rate. We can estimate the required repetition rate using the previously measured frequency separation between the two field-free D -level energies in the calcium-40 ion (Solaro *et al.* [44]). There, the zero-field linear frequency difference was found to be $f_{\text{Solaro}} = 1.819'599'021'534(8)$ THz. Since their value is corrected to eliminate the Zeeman contribution, we can adjust it to match our setup by introducing the Zeeman shifts $\Delta f_{\text{Zeeman}, m_J}$, introduced in [equation \(2.12\)](#).

One important quantity of the Zeeman shift is the magnetic field strength B , which was measured to be $B \approx 3.08 \text{ G} = 0.308 \text{ mT}$ using a Ramsey spectroscopy technique [119, ch. 4.8.1]. The magnetic field strength was measured with the same ions that were used to measure all the Rabi spectra. Furthermore, we need the two D -level values for the Landé g -factors ($g_{5/2} = 1.2$ and $g_{3/2} = 0.8$). With these values we can estimate the frequency

4.2 Measurements of Raman transitions and calcium-40 $D_{3/2}$ Landé g -factor

difference between the two target states using $f_{\text{Sol,Zee}} = f_{\text{Solaro}} + \Delta f_{\text{Zeeman},m_{5/2}} - \Delta f_{\text{Zeeman},m_{3/2}}$. In the experiment we used only the $3^2D_{5/2}(m_{5/2} = -1/2)$ state as the initial state due to technical limitations (state preparation in other Zeeman sublevels was not yet automated). The lower energy state was either $3^2D_{3/2}(m_{3/2} = -1/2)$ or $3^2D_{3/2}(m_{3/2} = +3/2)$.

The design repetition rate of the optical frequency comb is around $f_{\text{rep},0} = 250$ MHz. We have the ability to tune this value by changing the setpoint of the PID-controlled repetition rate stabilization and subsequently re-locking the system. The range at which the setpoint can be changed is at least on the order of 10 kHz. We can also shift the setpoint by smaller values, on the order of 100 Hz, without having to re-lock the system, which is later useful for varying the repetition rate. Any value set for the repetition rate is stabilized to the mHz level. Thus, we adjust the repetition rate $f_{\text{rep},0}$ to f_{rep} such that f_{rep} is approximately an integer multiple of $f_{\text{Sol,Zee}}$ fulfilling the condition for driving transitions with an optical frequency comb (see section 2.2.3). We can estimate the repetition rate f_{rep} required to drive the intended transition by determining how many times the base repetition rate $f_{\text{rep},0}$ fits into $f_{\text{Sol,Zee}}$. This can be done using $N = \lfloor f_{\text{Sol,Zee}}/f_{\text{rep},0} \rfloor$ or $N = \lceil f_{\text{Sol,Zee}}/f_{\text{rep},0} \rceil$ and then $f_{\text{rep}} = f_{\text{Sol,Zee}}/N$. The integer N was always found to be $N = 7278$ if the floor function was used ($\lfloor \cdot \rfloor$) and $N = 7279$ if the ceiling function was used ($\lceil \cdot \rceil$). This integer N represents the difference in comb tooth indices of two teeth that can drive the target transition, which is only possible if their difference in frequency is approximately $f_{\text{Sol,Zee}}$. The integer N is later be verified experimentally.

Having estimated the repetition rate f_{rep} that could drive a Raman transition between the two target states, the next hurdle is to find the right order of magnitude for the repetition rate at which such a transition shows detectable dynamics. Assuming a transform-limited transition linewidth with a pulsetrain length of $t_{\text{pulse}} = 1$ ms, we can estimate the order of magnitude to be $1/(N t_{\text{pulse}}) \approx 0.14$ Hz.

Using this estimated value for determining the range over which we vary the repetition rate, the estimated ideal repetition rate and a long pulsetrain length of about 1 ms, we were able to find a resonance. Typical measurements obtained by varying the repetition rate, resulting in Rabi spectra, and varying the optical frequency comb pulsetrain length, resulting in Rabi oscillations, can be found in figure 4.2. In this figure, the retrieved fit parameters using the model in equation (2.22) for the Rabi oscillations (left, blue) are $A = 0.988(11)$, $t_0 = -3.7(16)$ μs , $\Omega = 2\pi \cdot 2.5635(17)$ kHz, $c = 0.487(4)$, and $\tau = 7.1(3)$ ms. The Rabi spectrum (right, red) was fitted using the model in equation (2.23), the resulting fit parameters are $A = -0.937(14)$, $f_0 = -861.83(5)$ kHz, $\Omega = 2\pi \cdot 2.82(4)$ kHz, and $c = 0.980(3)$. A two-dimensional sweep of pulsetrain length and transition frequency was also performed. The results can be found in appendix D.2.

In the context of equation (2.34), the Raman Rabi rate in figure 4.2 serves as a measure of interaction efficiency in the presence of dispersion. Raman Rabi rate measurements were performed for different group delay dispersion settings on the chirped fiber Bragg grating and compared to predictions using measured FROG spectra. The results are presented in appendix D.3.

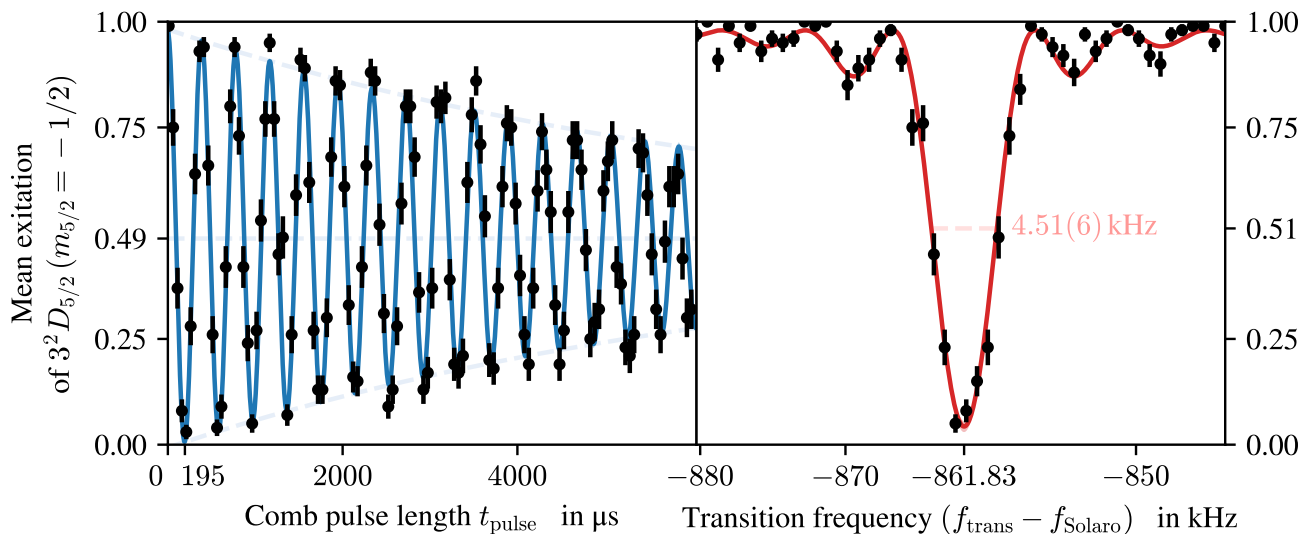


Figure 4.2: **Typical coherent Raman Rabi oscillation and spectrum of the selected D -level transition.** The targeted calcium-40 ion transition was $3^2D_{5/2} (m_{5/2} = -1/2) \leftrightarrow 3^2D_{3/2} (m_{3/2} = -1/2)$. The horizontal scale on the right plot was converted from repetition rate to actual transition frequency by multiplying the repetition rate with $N = 7278$ and shifted by f_{Solaro} to have an experimentally verified target value at zero.

As expected, the transition frequency shown in figure 4.2 is $-861.83(5) \text{ kHz} + f_{\text{Solaro}}$, far off the reference frequency. This is due to frequency shift corrections that still need to be applied to retrieve a zero-field transition frequency. The two major corrections we can apply are the Zeeman shift correction and the AC-Stark shift correction.

Typical Zeeman shift corrections are done by measuring the transition frequencies $m_{5/2} = -1/2 \leftrightarrow m_{3/2} = -1/2$ and $m_{5/2} = +1/2 \leftrightarrow m_{3/2} = +1/2$ [44, 120, 121]. According to equation (2.12), if we take the mean of both transition frequencies, the result gives the Zeeman-corrected frequency. This eliminates the need to precisely measure the Landé g -factors and B -field magnitude. Also, the choice of these two particular transitions makes the result less sensitive to magnetic field fluctuations.

This approach was not chosen in our setup since a preparation in the $3^2D_{5/2} (m_{5/2} = +1/2)$ was not yet automated, rather only the preparation in the $3^2D_{5/2} (m_{5/2} = -1/2)$ state. Thus, for the correction it was necessary to know the values of the two Landé g -factors of the states: $g_{5/2}$ (of the state $3^2D_{5/2}$) and $g_{3/2}$ (of the state $3^2D_{3/2}$).

An experimentally measured value of $g_{5/2}$ was found ([88, p. 81], see equation (2.14)), however none was available for $g_{3/2}$. An experiment was thus performed to measure the value of $g_{3/2}$. For this, the value of $g_{3/2}$ was introduced in the data analysis of this work as a variable. A probability distribution function for this variable was assumed and updated with the data. The optimal value of $g_{3/2}$ was found using the updated distribution (posterior).

4.2 Measurements of Raman transitions and calcium-40 D3/2 Landé g-factor

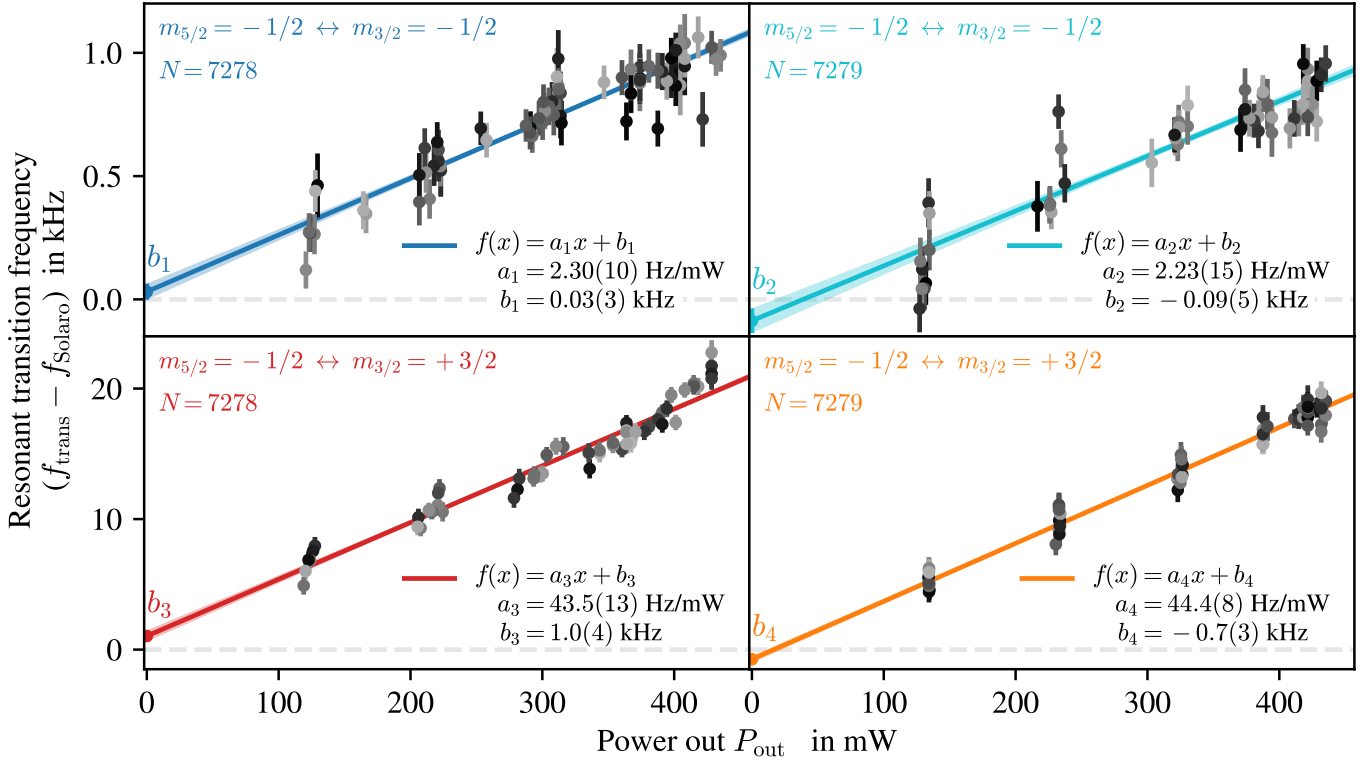


Figure 4.3: **Measurements of self-induced AC-Stark shift.** To find the zero-field transition frequency of the $3^2D_{5/2} \leftrightarrow 3^2D_{3/2}$ transition, various measurements analogous to the right plot in figure 4.2 at different randomly chosen powers of the optical frequency comb P_{out} at different transitions were performed. Plotted are the evaluated center frequencies Δ_0 (or f_0) from equation (2.23) of each measurement for the indicated transitions and comb teeth difference numbers N . The y -intercepts are the estimated Stark shift-free transition frequencies. The presented data was colored randomly in different shades of gray to make them distinguishable. This data was Zeeman shift-corrected using the evaluated optimal Landé $g_{3/2} = 0.79945$. However, in the data analysis, $g_{3/2}$ was a variable. Changing the value of $g_{3/2}$ shifts the displayed data points vertically, with each displacement depending on the B -field magnitude at the time of recording of each data point. The measured optical power P_{out} is recorded from part of the comb light that was transmitted through the ion trap.

We also simultaneously corrected for the AC-Stark shift in this optimization process. We estimated the transition frequency as a function of the laser power. According to equation (2.31), the effective detuning depends linearly on the magnitudes of the squared single-beam Rabi rates, which in turn are proportional to the laser intensities or powers. Lowering the power of the optical frequency comb lowers the contributions of all the comb teeth at the same rate. Thus, the transition frequency depends linearly on power.

In the experiment, the power of the optical frequency comb was changed by varying

the radio frequency power delivered to the acousto-optical modulator (AOM) found in the combs optical path. Data was collected by randomly choosing from a set of AOM radio frequency powers, measuring the optical power P_{out} from a portion of the light transmitted through the vacuum chamber, and measuring the resonance frequency of the chosen transition. The Zeeman shift was corrected for each measured data point using the known $g_{5/2}$ value, the variable $g_{3/2}$ value, and the estimated average B -field magnitude at the time of measurement. The average B -field magnitude refers to the value and error of a linear fit through data that shows the B -field magnitude as a function of time. This procedure captures the time average of the measured B -field while also allowing for a linear drift over time. Alternative ways of estimating the average B -field at the time of each measurement are shown in appendix C.

The resulting data of the described data analysis is shown in figure 4.3. The data was collected for the transitions $m_{5/2} = -1/2 \leftrightarrow m_{3/2} = -1/2$ and $m_{5/2} = -1/2 \leftrightarrow m_{3/2} = +3/2$, in combination with comb tooth difference indices $N = 7278$ and $N = 7279$. The four data sets are described by a linear function due to the scaling behavior of the eigenenergies of equation (2.19), as they depend on the detuning, which is set to zero, and the Raman Rabi rate, which is proportional to the intensity of the light. By applying linear fits, we can extract the transition frequency value at $P_{\text{out}} = 0$ mW, retrieving the AC-Stark shift corrected transition frequency. Up to this point, we have treated the Landé g -factor $g_{3/2}$ as a variable. However, it should be noted that these plots use the measured optimal value for $g_{3/2}$, which will soon be presented in equation (4.2).

To estimate the experimental value of the Landé g -factor $g_{3/2}$, the analysis described above was repeated for various $g_{3/2}$ values. The $g_{3/2}$ value was sampled from a grid of equally spaced values close to the theoretical value of 0.8. For each grid point, the four y -axis intercepts of the linear fits (corresponding to $P_{\text{out}} = 0$ mW) were extracted. An example of these intercepts for a single $g_{3/2}$ grid point is shown in figure 4.3. We label these intercepts, or zero-field transition frequencies, b_j , where $j \in \{1, 2, 3, 4\}$, and their corresponding uncertainties $\alpha_{b,j}$. These four frequencies enter a constructed likelihood function, whose underlying probability density function was assumed to be the Student's t -distribution [122, ch. 8.8]. This distribution has larger tails compared to the Gaussian distribution and is useful for a small sample size, such as our case, as we only have four samples.

This likelihood function has the form

$$\mathcal{L}(g_{3/2}) = \prod_{j=1}^4 t_{\nu} \left(\frac{b_j(g_{3/2}) - 0}{\alpha_{b,j}(g_{3/2})} \right) \frac{1}{\alpha_{b,j}(g_{3/2})}, \quad (4.1)$$

where $t_{\nu}(x)$ is the Student's t probability density function and $\nu = 3$ is the number of degrees of freedom in the problem. The degrees of freedom are the number of data points (4, b_j) minus the number of free parameters (1, $g_{3/2}$). The value 0 is normally replaced by a model function, but here our model function is Solaro's reference value for the D -level transition. Since we normalized our data to f_{Solaro} , the model function value becomes 0.

The optimal value of $g_{3/2}$ was chosen to be where the cumulative distribution function of $\mathcal{L}(g_{3/2})$ equals 0.5, as this represents the median of the distribution. On the other hand,

4.2 Measurements of Raman transitions and calcium-40 $D_{3/2}$ Landé g -factor

the uncertainty margins of the optimal $g_{3/2}$ value are chosen to be $0.5 \pm \sigma/2$, where the value $\sigma = \text{erf}(1/\sqrt{2}) \approx 0.68$ is based on a Gaussian distribution, and erf is the Gauss error function. The resulting optimal Landé g -factor of the calcium-40 ions $3^2D_{3/2}$ state was thus found to be

$$g_{3/2}^{\text{exp}} = 0.79945(2) \quad (4.2)$$

This result is 0.069% smaller than the theoretical value of 0.8 and has a relative uncertainty of $2.5 \cdot 10^{-5}$. This deviation from the theoretical value is comparable to the one reported in reference [88, p. 81]. There, the experimental value of $g_{5/2}$ was found to be 0.028% higher than the theoretical prediction (see equation (2.14)). To extract a more correct version of $g_{3/2}^{\text{exp}}$, we could include further corrections in the error budget [123, 124], e.g., second-order Doppler shift [125], blackbody radiation shift [126], second-order Zeeman shift [127, 128], quadratic DC-Stark shift [129], and potentially other interacting lasers inducing AC-Stark shifts. However, this was not done in this work, as their shifts and uncertainties are likely small in comparison to the more dominant uncertainties such as B -field fluctuations and 729 nm fiber noise.

Instead of using equation (4.1) to extract $g_{3/2}^{\text{exp}}$, here referred to as the all-at-once method, an alternative approach is to calculate the optimal individual Landé g -factor $g_{3/2,j}$ and its uncertainty $\alpha_{g,j}$ for each zero-field transition frequency b_j and its uncertainty $\alpha_{b,j}$, and then combine these values to obtain the final result. This alternative approach, referred to as the individual evaluation method, yielded an estimated Landé g -factor of 0.799451(12), which agrees with the all-at-once method. Ultimately, the all-at-once method combined the data under a single statistical distribution, making it the more appropriate choice, as it extracts information from all measurements simultaneously, while also accounting for correlations and shared systematics that the individual evaluation method may neglect. Nevertheless, the individual evaluation method is further compared to the all-at-once method in appendix C, along with different interpolation methods for the B -field.

Using the extracted Landé factor $g_{3/2}^{\text{exp}}$, we can correct the measured data for Zeeman and AC-Stark shifts, as already shown in figure 4.3. The resulting four corrected zero-field transition frequencies $b_j(g_{3/2}^{\text{exp}})$ can be compared to their combined value, calculated analogously to equation (C.1). By construction, this combined value overlaps with the value found by Solaro *et al.* [44], as their value was used as the reference for the measured data, which was optimized to converge toward it based on equation (4.1). These values are shown in figure 4.4. This plot can give us insights about the magnitude of the uncertainties in our system by looking at the magnitude of the uncertainties of the shown data.

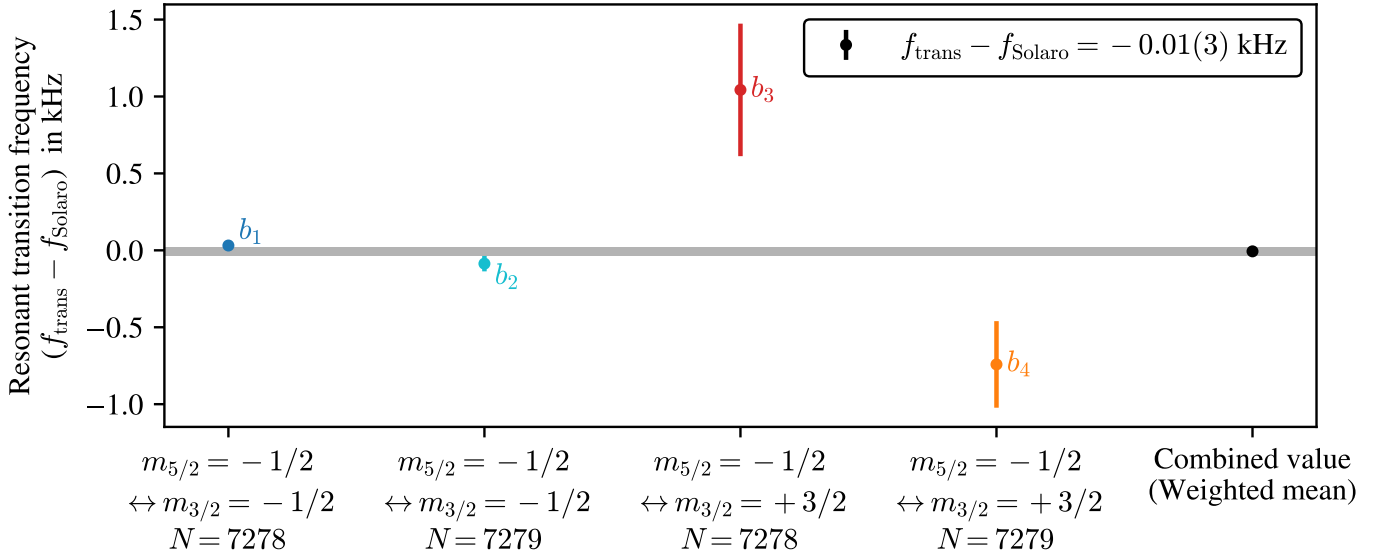


Figure 4.4: **Zero-field transition frequencies for four experimental settings.** The colored data points are the b_j values from figure 4.3. The x -axis indicates the targeted transition and the comb teeth difference number N . Varying the Landé $g_{3/2}$ in such a way that these four data points combine to overlap with Solrao's *et al.* measurement f_{Solaro} [44] leads to the retrieval of the optimal $g_{3/2} = 0.79945$, used in this plot. The optimization is done using the likelihood function in equation (4.1). The shaded area represents the uncertainty of the combined value representing the standard error of the weighted mean.

As an additional and final result in this section, we show that the index difference between the comb teeth pairs driving the transition was indeed $N = 7278$ and $N = 7279$. This was verified by taking the b_j values from the data in figure 4.3 and transforming them into repetition rate values $f_{\text{rep},j}$. Our only assumption is that the difference in comb teeth is 1 between b_1 and b_2 (corresponding to the $m_{5/2} = -1/2 \leftrightarrow m_{3/2} = -1/2$ transition at frequency $f_{-1/2}$) and between b_3 and b_4 (corresponding to the $m_{5/2} = -1/2 \leftrightarrow m_{3/2} = +3/2$ transition at frequency $f_{+3/2}$). This is justified because we know both the repetition rate and the approximate transition frequency with sufficient precision. Using this assumption, we can set up the equations

$$\begin{aligned} f_{-1/2} &= f_{\text{CEO}} + N_{-1/2} f_{\text{rep},1}, & f_{-1/2} &= f_{\text{CEO}} + (N_{-1/2} + 1) f_{\text{rep},2}, \\ f_{+3/2} &= f_{\text{CEO}} + N_{+3/2} f_{\text{rep},3}, & f_{+3/2} &= f_{\text{CEO}} + (N_{+3/2} + 1) f_{\text{rep},4}. \end{aligned}$$

Substituting the measured repetition rates and solving for N yields:

$$\begin{aligned} N_{-1/2} &= \left(\frac{f_{\text{rep},1}}{f_{\text{rep},2}} - 1 \right)^{-1} = 7278.005(2) \\ N_{+3/2} &= \left(\frac{f_{\text{rep},3}}{f_{\text{rep},4}} - 1 \right)^{-1} = 7278.014(11). \end{aligned}$$

4.3 Ramsey interferometry

The closest integer of both retrieved values is 7278, as assumed in the beginning. To obtain an integer value of 7277 instead of 7278 from the same calculations, the repetition rates $f_{\text{rep},1}$ and $f_{\text{rep},3}$ would need to be approximately 4.75 Hz higher, which would result in a transition frequency shift of about 35 kHz. This possibility can be safely discarded, as the range of frequencies used to obtain the Rabi spectra was one order of magnitude smaller than this shift.

As a final note, the original plan for this work was not to measure the Landé g -factor $g_{3/2}$, but rather the zero-field transition frequency of the transition $3^2D_{5/2} \leftrightarrow 3^2D_{3/2}$. However, due to technical limitations and the lack of knowledge of an experimental value of $g_{3/2}$, this was not possible. Thus, we used the transition frequency measured by Solaro *et al.* and took it as a reference to back out the value of $g_{3/2}^{\text{exp}}$.

4.3 Ramsey interferometry

Another aspect of the ion and optical frequency comb interaction which can be readily studied is quantum coherence. Quantifying phase noise in the system can be achieved via Ramsey interferometry, both with and without spin echo. For both methods, one can use the general experimental **sequence** explained in chapter 4 and adapt it to include the Ramsey and spin echo sequences explained in section 2.2.4 using the optical frequency comb. The transition probed in this section is $3^2D_{5/2} (m_{5/2} = -1/2) \leftrightarrow 3^2D_{3/2} (m_{3/2} = -1/2)$.

Due to the nature of a two-photon Raman process transition where both photons originate from the same beam, it is not possible to implement the usual Ramsey measurement which involves the Ramsey contrast quantity. Instead of varying the phase of the second π -pulse for a set of waiting times τ , we vary directly the waiting time with a fixed detuning, giving rise to decaying fringes [130] as shown on the left side of figure 4.5. The decay constant is the same as retrieved with the Ramsey contrast method; however, it is less precise as it involves less measured data, increasing the statistical error.

The best fitting function for the decaying envelope resembled more closely a Gaussian decay than an exponential decay (judging by chi-squared statistics, where typical reduced chi-square values were $\chi_{\nu,\text{Gauss}}^2 = 1.22$ and $\chi_{\nu,\text{exp}}^2 = 1.82$), indicating that the decay is closer to being quasi-static [100] in nature rather than white noise [99]. Typical extracted decay constants, which correspond to an amplitude reduction to $1/e$, range from 0.376(18) ms to 0.41(3) ms, indicating the dephasing timescale of the dominant low-frequency noise in our system. The origin of this noise is likely magnetic field fluctuations at the location of the ion. The quantization B -field is generated by a single coil, which also introduces a significant nonlinear gradient, amplifying fluctuations in both the magnitude and direction of the B -field. Other less significant noise sources include fluctuating ion position, laser intensity, phase, repetition rate, and beam pointing [131].

Regarding the example data shown on the left side of figure 4.5, the detuning of the Ramsey measurement without spin echo was manually set to $7278 \cdot 0.6 \text{ Hz} = 4.367 \text{ kHz}$. Fitting this data resulted in the optimal parameters $A = 0.73(3)$, $c = 0.576(5)$, $\Delta_0 = 2\pi \cdot 3.38(3) \text{ kHz}$ ($\neq 2\pi \cdot 4.367 \text{ kHz}$), and $T_2^* = 0.376(18) \text{ ms}$.

Having looked Ramsey interferometry without spin echo, we can analyze the high-

frequency noise within the system by introducing spin echo. Typical results of the Ramsey interferometry with spin echo are shown on the right side of figure 4.5. In contrast to the results from the Ramsey interferometry without spin echo, the spin echo technique does not require a detuning and it introduces a π -pulse in the middle of the waiting time τ .

Similarly, this data was best described by a Gaussian function ($\chi^2_{\nu, \text{Gauss}} = 1.58$ vs. $\chi^2_{\nu, \text{exp}} = 2.78$), indicating again that high-frequency noise is quasi-static in nature. The extracted 1/e decay constants range from 1.35(14) ms to 1.73(18) ms. Specifically for the data shown on the right side of figure 4.5, the fit parameters of the spin echo measurement were determined to be $A = 0.93(4)$, $c = 0.456(13)$, and $T_2 = 1.50(10)$ ms.

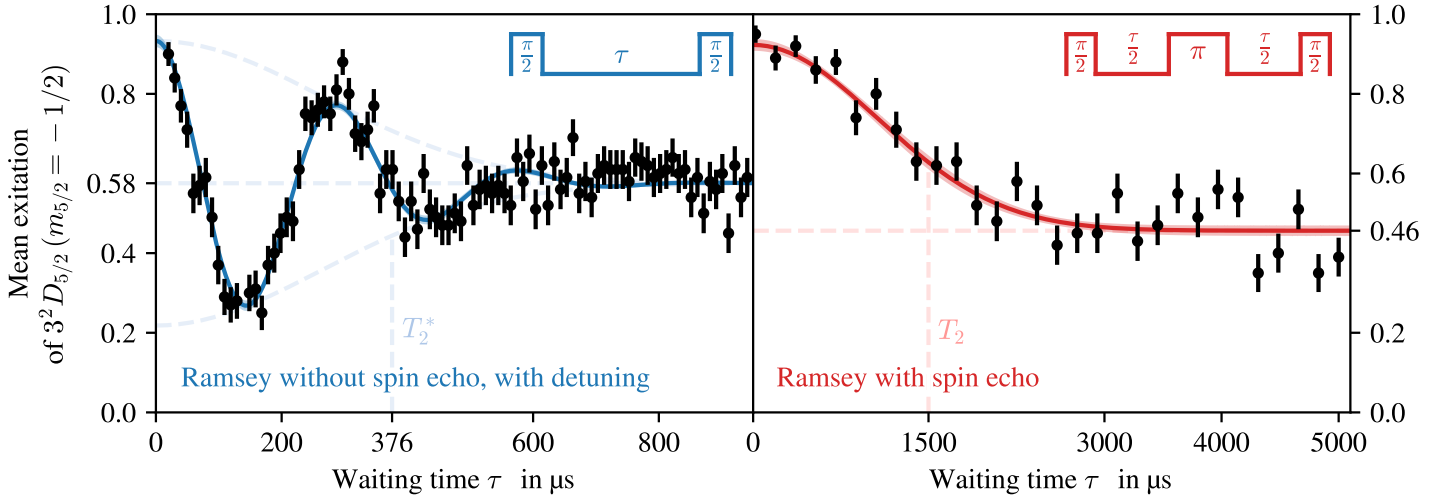


Figure 4.5: **Ramsey interferometry and spin echo measurements.** The calcium-40 ion transition used for this measurement was the $3^2D_{5/2} (m_{5/2} = -1/2) \leftrightarrow 3^2D_{3/2} (m_{3/2} = -1/2)$ transition. The pulse sequences used for each measurement are shown on the top right of each plot. The fit functions follow equation (2.37) with a Gaussian envelope.

Discussion and outlook

This thesis presented basic concepts of optical frequency combs, such as dispersion and self-phase modulation, and described how they can be used to manipulate the state of trapped ions via Raman transitions and the AC-Stark effect. These concepts have been implemented experimentally by increasing the bandwidth of a commercial optical frequency comb to about 5 THz via self-phase modulation in a highly nonlinear fiber, compressing the pulse duration close to the Fourier limit to about 110 fs using dispersion compensation, and demonstrating coherent Raman transitions with a calcium-40 ion between the $3^2D_{5/2}$ and $3^2D_{3/2}$ Zeeman fine structure states separated by 1.8 THz. For these transitions, if properly compensated for dispersion, all individual comb teeth can coherently contribute to driving the transitions.

These interactions resulted in high-contrast Rabi oscillations with rates of up to 2.8 kHz, linewidths of about 4.5 kHz, and decay time constant of up to 7 ms. In [44], a similar experiment achieved a Rabi rate of about 4.1 kHz. To properly compare this value to our setup, we have to adjust for the differences in detuning (our system: 155 THz vs. [44]: 29 THz), power (450 mW vs. 90 mW), and laser beam radius ($\sim 40 \mu\text{m}$ vs. $34 \mu\text{m}$) based on equation (2.28). The performance of both of our systems is similar if we assume a laser beam radius of $42 \mu\text{m}$ in our system.

Dephasing was characterized by executing an adapted Ramsey sequence and a spin-echo sequence, which resulted in dephasing times of 0.38 ms and 1.5 ms, respectively. The dephasing limitations of our quantum system most likely stem from magnetic field instabilities, including environmental B -field noise. Our current configuration for generating a magnetic field at the trapped ion's location relies on a single coil. Implementing a Helmholtz configuration would significantly reduce the nonlinear B -field gradient, which amplifies B -field noise. Additionally, incorporating a stabilization unit and a magnetic shield would further improve field stability.

In addition, the optical frequency comb was used to spectroscopically measure the Landé g -factor of the $3^2D_{3/2}$ state to a precision of $3 \cdot 10^{-5}$, resulting in a value of 0.79945(2).

The current state of the optical system cannot drive Zeeman transitions with a change of projection quantum number $\Delta m = \pm 1$ as the comb can only provide superpositions of σ^+ and σ^- polarized photons but no π -polarized photons due to the comb being aligned with its propagation axis along the direction of the magnetic field, see figure 5.1b. The setup is also limited by which transition energies it can drive. The upper limit is set by the bandwidth (5 THz) and the lower limit by the repetition rate (250 MHz). Furthermore, the comb relies on adjusting the repetition rate for fine-tuning a resonant transition frequency.

This is a rather slow process, especially in cases where the lock-point of the repetition rate needs to be changed.

We would benefit from a setup with two separate branches of the optical frequency comb. In this so-called two-beam comb setup, each path's frequencies are individually shifted using acousto-optical modulators (AOMs) (see figure 5.1c). Instead of adjusting the repetition rate, the offset from a transition frequency is set by the AOM drive frequency, enabling faster and broader tuning, as the lower limit for possible transition frequencies is set by the linewidth of the radio-frequency signal sent to the AOMs. This technique achieves sub-kHz lower limits. Additionally, splitting the comb allows control over π -polarization: one branch can deliver π -polarized photons while the other provides σ -polarized photons, enabling $\Delta m = \pm 1$ Zeeman transitions and access to all Zeeman sublevels. However, a disadvantage comes from the fact that each branch is identified with a particular contribution to the two-photon Raman process, as opposed to each comb tooth driving both upward and downward contributions simultaneously as in the single-beam case. Since the comb's power is split into two, and each branch only contributes to one Raman path, the maximal possible efficiency is halved compared to the single-beam comb setup, and it becomes comparable to a two-beam CW (continuous-wave) Raman setup [33]. The two-beam CW Raman setup is shown in figure 5.1a.

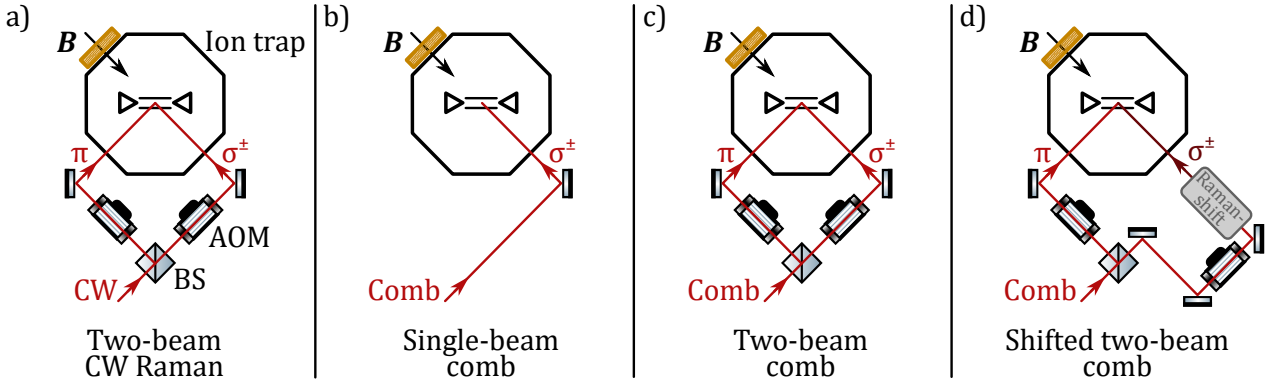


Figure 5.1: **Variations of this works setup.** CW: continuous-wave, Comb: optical frequency comb, AOM: acousto-optical modulator, BS: beam splitter, Raman-shift: Raman-induced self-frequency shift, π : π -polarized light, σ^\pm : σ^+ - or σ^- -polarized light, B: magnetic field.

We can extend the idea of the two-beam comb setup such that the upper limit of possible transition frequencies is no longer limited by its bandwidth. By harvesting the effect of the Raman-induced self-frequency shift [132–134] (Raman-shift), we can continuously redshift the comb's central wavelength and its spectrum due to intrapulse Raman scattering [71, p. 4.3.3]. This effect arises from the interaction between the comb and a nonlinear medium's vibrational modes. By engineering the creation of Raman solitons, e.g., pulses that maintain their shape during propagation through a medium due to a balance between dispersion and nonlinearity [71, ch. 5], the evolution of the system becomes predictable, and the central frequency of the optical frequency comb can be adjusted to the needs of the experiment. An experimental demonstration can be found in [135].

The two-beam comb setup could then be expanded into the shifted two-beam comb setup by taking one branch of the two-beam comb and making it undergo a controlled Raman-shift, possibly also utilizing difference frequency generation with the original comb, see figure 5.1d. This expands the upper limit of accessible transition frequencies, as the limit is now set by the difference in frequency of the center frequencies of the spectra plus their combined bandwidths. As shown in [136], a Raman-shifted optical frequency comb can even reach mid-infrared wavelengths. The target frequency of the Raman-shifted comb can be adjusted by controlling the power sent through the nonlinear setup. The lower limit of accessible transition frequencies is set by the difference in the center frequency difference between the original comb and the Raman-shifted comb minus their combined bandwidths. Additional drawbacks of this setup include the additional complexity of the system due heavy reliance on nonlinear optics and the significant power (and thus efficiency) losses due to the frequency conversion processes.

Note that no published setup was found that matches this description, but it is known that NIST [137] is working on such a dual-branch frequency comb Raman to perform vibrational transitions in CaH^+ . This idea might have potential for coherent control of molecular rotational and vibrational states. The repetition rate remains constant as the timing of each pulse is set by the source and is not influenced by nonlinear optics. The change of the carrier-envelope offset frequency during the Raman-shifting is not relevant for driving Raman transitions, as this frequency cancels out. A comparison of the discussed setup options is shown in table 5.1.

Setup	Two-beam CW Raman [33]	Single-beam comb [44]	Two-beam comb [45, 138]	Shifted two-beam comb
$f_{\text{trans}}^{\text{min}}$	sub-kHz	~ 100 MHz	sub-kHz	spectra separation
$f_{\text{trans}}^{\text{max}}$	~ 1 GHz	~ 10 THz	~ 10 THz	~ 100 THz
Δm	0, ± 1 , ± 2	0, ± 2	0, ± 1 , ± 2	0, ± 1 , ± 2
$\eta_{\text{CW}}^{\text{max}}$	1	2	1	1
η_{CW} loss	none	dispersion	dispersion	dispersion and shift

Table 5.1: **Comparison between different optical Raman systems.** The performance indicators indicate the minimal and maximal accessible transition frequency ($f_{\text{trans}}^{\text{min}}$ and $f_{\text{trans}}^{\text{max}}$), the possible change in projection quantum numbers of the two involved states (Δm), the maximal achievable efficiency compared to the two-beam CW Raman setup ($\eta_{\text{CW}}^{\text{max}}$, analogous to equation (2.34)), and the reasons for efficiency losses (η_{CW} loss).

Methods for further increasing the bandwidth of the optical frequency comb will still be investigated within our research group, such as increasing the length of the highly nonlinear fiber. Our group’s next step is to implement the two-beam comb setup and demonstrate control over rotational energy levels in molecules such as CaOH^+ , CaH^+ or CaD^+ similar to [45]. Moreover, the setup will also be used for exploring molecular quantum error correction against noise such as black body radiation [26].

APPENDIX **A**

Fourier transform of a pulsed laser

This appendix expands on the derivation presented in section 2.1. A general pulsetrain in the time domain can be modeled using an envelope function, $E_{\text{single}}(t)$, which repeats with period T , together with an oscillating function with unit amplitude, $\cos(\phi(t))$. This model for the electric field is given by

$$E(t) = \cos(\phi(t)) \sum_{n=-\infty}^{\infty} E_{\text{single}}(t - nT).$$

We simplify the analysis by setting $\phi(t) = \omega_c t - \phi_0$. To understand the Fourier transformation it is helpful to introduce the Dirac comb $\text{III}_T(t)$ and convolution $(A * B)(t)$, where

$$\text{III}_T(t) := \sum_{n=-\infty}^{\infty} \delta(t - nT) \quad \text{and} \quad A(t) * B(t) := \int_{-\infty}^{\infty} A(\tau)B(t - \tau) d\tau.$$

The distribution $\delta(t)$ is called the Dirac delta function and has the properties

$$\int_{-\infty}^{\infty} A(t)\delta(t - a) dt = A(a) \quad \text{and} \quad \delta(at) = \frac{1}{|a|}\delta(t).$$

With these we can rewrite the model for the electric field as

$$\begin{aligned} E(t) &= \cos(\omega_c t - \phi_0) \sum_{n=-\infty}^{\infty} E_{\text{single}}(t - nT) \\ &= \cos(\omega_c t - \phi_0) \sum_{n=-\infty}^{\infty} \int_{-\infty}^{\infty} E_{\text{single}}(\tau) \delta(\tau - (t - nT)) d\tau \\ &= \cos(\omega_c t - \phi_0) \sum_{n=-\infty}^{\infty} \int_{-\infty}^{\infty} E_{\text{single}}(\tau) \delta((t - \tau) - nT) d\tau \\ &= \cos(\omega_c t - \phi_0) \int_{-\infty}^{\infty} E_{\text{single}}(\tau) \text{III}_T(t - \tau) d\tau \\ &= \cos(\omega_c t - \phi_0) E_{\text{single}}(t) * \text{III}_T(t). \end{aligned}$$

In this form the analysis and interpretation using the Fourier transform

$$\mathcal{F}\{A(t)\}(\omega) = \frac{1}{\sqrt{2\pi}} \int_{-\infty}^{\infty} A(t)e^{-i\omega t} dt \tag{A.1}$$

is simpler. Using the convolution theorem

$$\begin{aligned}\mathcal{F}\{A(t) * B(t)\}(\omega) &= \mathcal{F}\{A(t)\}(\omega) \mathcal{F}\{B(t)\}(\omega), \\ \mathcal{F}\{A(t)B(t)\}(\omega) &= \mathcal{F}\{A(t)\}(\omega) * \mathcal{F}\{B(t)\}(\omega)\end{aligned}$$

we derive

$$\begin{aligned}\tilde{E}(\omega) &= \mathcal{F}\{E(t)\}(\omega) \\ &= \mathcal{F}\{\cos(\omega_c t - \phi_0)\}(\omega) * (\mathcal{F}\{E_{\text{single}}(t)\}(\omega) \mathcal{F}\{\text{III}_T(t)\}(\omega)).\end{aligned}$$

The Fourier transform of the cosine term is known and amounts to

$$\mathcal{F}\{\cos(\omega_c t - \phi_0)\}(\omega) = \sqrt{\frac{\pi}{2}} (e^{-i\phi_0} \delta(\omega - \omega_c) + e^{i\phi_0} \delta(\omega + \omega_c)).$$

On the other hand, the Fourier transform of a Dirac comb is a rescaled version of a Dirac comb

$$\mathcal{F}\{\text{III}_T(t)\}(\omega) = \text{III}_{2\pi/T}(\omega).$$

For the derivation of this relation, we use the Poisson summation formula. One can qualitatively understand this relation by concluding $\mathcal{F}\{\delta(t - nT)\}(\omega) = e^{-i\omega nT} / \sqrt{2\pi}$ and realizing that an infinite sum over n of such exponential functions would destructively interfere everywhere except at points where ωT is an integer multiple of 2π .

Ignoring negative frequencies, the frequency domain representation of the electric field model is

$$\begin{aligned}\tilde{E}(\omega) &= \sqrt{\frac{\pi}{2}} e^{-i\phi_0} \delta(\omega - \omega_c) * (\mathcal{F}\{E_{\text{single}}(t)\}(\omega) \text{III}_{2\pi/T}(\omega)) \\ &= \sqrt{\frac{\pi}{2}} e^{-i\phi_0} \mathcal{F}\{E_{\text{single}}(t)\}(\omega - \omega_c) \text{III}_{2\pi/T}(\omega - \omega_c).\end{aligned}$$

APPENDIX B

AC-3 unit repair

The AC-3 control unit, which provides the 975 nm pump light for the high-power amplification of the optical frequency comb, experienced a critical failure on 08.02.2024. The AC-3 unit was operated above its 50% setting, which caused the fibers inside the unit to burn and break due to the too-high intensities of the pump light. The resulting damage can be seen in figure B.1. The cause for the failure might arise from back reflections and energy density accumulations in certain spots. These might have been caused by non-ideal fiber splices and tight curvatures of the fiber. The unit was repaired by splicing the surviving fiber ends together using the Vytran FFS2000PM fiber splicer. A tutorial on fiber splicing was consequently written. Opening the AC-3 to access its circuitry or optics should now be done with caution, as two short and unprotected optical fibers lie directly underneath the cover.

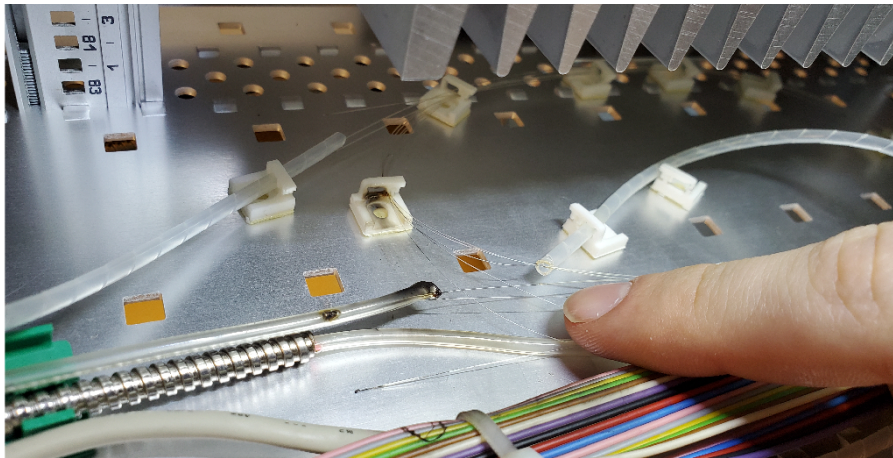


Figure B.1: **AC-3 unit failure.** The optical fibers leading the pump light to the amplification system burned due to high-power operation. This unit provides the pump light which amplifies the optical frequency comb up to 2.5 W.

Comparison of Landé g -factor extraction methods

Section 4.2 extracts a value for the Landé g -factor $g_{3/2}$ of the $3^2D_{3/2}$ state from measured spectroscopic data. There were several approaches to extracting this value, each with a slightly different result. This appendix covers the key differences.

During the analysis, the AC-Stark shift-corrected transition frequencies $b_j(g_{3/2})$ with uncertainties $\alpha_{b,j}(g_{3/2})$ were extracted as a function of a variable $g_{3/2}$, where $j \in \{1, 2, 3, 4\}$. The method used in section 4.2 combined these values in a single likelihood function \mathcal{L} (see equation (4.1)), and extracts from that the most likely $g_{3/2}$ value with its associated uncertainty $\alpha_{g,3/2}$. This method is referred to as the all-at-once method (AAOM).

A different approach to this procedure is referred to as the individual evaluation method (IEM). Here, a Gaussian likelihood function is constructed from each $b_j(g_{3/2})$, $\alpha_{b,j}(g_{3/2})$ pair according to

$$\mathcal{L}_j^{\text{IEM}}(g_{3/2}) = \frac{1}{\sqrt{2\pi} \alpha_{b,j}(g_{3/2})} \exp\left(-\frac{1}{2} \left(\frac{b_j(g_{3/2}) - 0}{\alpha_{b,j}(g_{3/2})}\right)^2\right).$$

For each $\mathcal{L}_j^{\text{IEM}}(g_{3/2})$, the optimal $g_{3/2,j}$ with error $\alpha_{g,j}$ was then calculated. The combined value (weighted mean) and its uncertainty

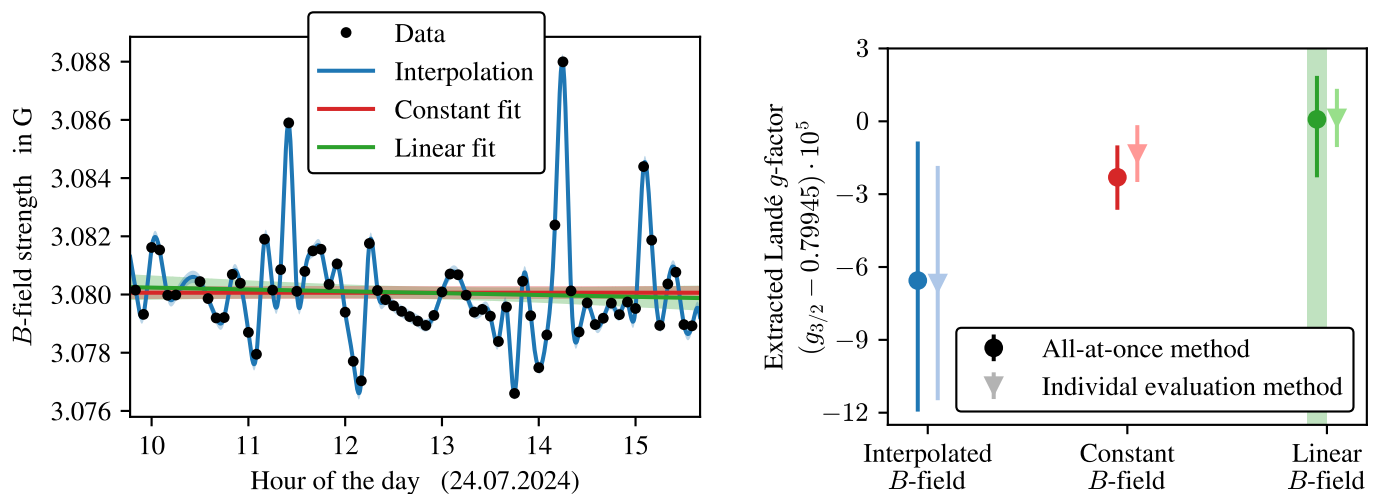
$$g_{3/2}^{\text{IEM}} = \frac{\sum_{j=1}^4 g_{3/2,j} \alpha_{g,j}^{-2}}{\sum_{j=1}^4 \alpha_{g,j}^{-2}}, \quad \frac{1}{\alpha_{g,3/2}^{\text{IEM}}} = \sqrt{\sum_{j=1}^4 \alpha_{g,j}^{-2}} \quad (\text{C.1})$$

were then extracted, returning an estimate for Landé g -factor of the $3^2D_{3/2}$ state. Ultimately, the AAOM was preferred over the IEM because it treats all data points as part of a unified statistical distribution. The AAOM not only maximizes the use of available information by analyzing all measurements collectively but also incorporates correlations and shared systematic effects that the IEM might overlook.

At a different point in the analysis, the extraction of the instantaneous magnetic B -field value during the time of data taking is relevant. Here, three further approaches were pursued. Given a data set of B -field strengths at the location of the ion as a function of absolute time, it is natural to interpolate values in between recorded data. However, interpolation results in an increase in the spread of the data points, artificially lowering the precision of the data. This can be explained by the fact that the method for measuring

the local B -field value (a Ramsey spectroscopy adapted from [119, ch. 4.8.1]) involved a 729 nm laser with no fiber noise cancellation, increasing the apparent random fluctuations in the B -field data points. To average over these fluctuations, two further approaches were investigated: a constant and a linear fit through the B -field data points. These fits were restricted to data sets containing time periods of no more than one day. All three approaches for B -field extraction are compared on a sample data set in figure C.1a. Ultimately, the linear fit approach was chosen over the constant fit as some data sets showed significant drifts.

In total, six different values of the Landé g -factor were extracted due to the 2·3 different approach combinations. All six final values are shown side by side in figure C.1b.



(a) Sample B -field data measured by Ramsey spectroscopy on a calcium-40 ion. (b) Comparison of Landé g -factor values using different methods.

Figure C.1: **Approaches for extracting the Landé g -factor $g_{3/2}$.** Figure C.1a shows a sample of B -field strength data as a function of absolute time. The three methods for extracting values in-between recorded data are shown. Figure C.1b shows six values for the Landé g -factor $g_{3/2}$ from the different method combinations. The value highlighted in green is the one chosen for section 4.2.

APPENDIX D

Additional data

This appendix provides supplementary data to chapter 4. The experimental [sequence](#) described there is used for sections [D.2](#) and [D.3](#). Section [D.1](#), on the other hand, shows different spectral properties depending on the polarization of the light exiting the highly nonlinear fiber. Section [D.2](#) provides a 2-dimensional scan of the Rabi landscape using the Raman-interacting optical frequency comb. Section [D.3](#) shows data of Raman Rabi rates as a function of the chirped fiber Bragg gratings settings.

D.1 Polarization-dependent spectra

The optical setup used in this work included a half-waveplate (HWP) and polarizing beam splitter combination located after the highly nonlinear fiber (HNLF). See the gray box in [figure 3.1](#). This setup only transmitted horizontal polarization. At the time it was not known that nonlinear effects act differently on different components of the polarization, especially since our HNLF was polarization-maintaining. As a result, the spectral shape and the temporal shape of the optical frequency comb changed when turning the HWP. The frequency-resolved optical gating (FROG) data measured after the 1 m dispersion compensating fiber for different HWP settings is shown in [figure D.1](#).

Additionally, it was observed that in order to achieve a Fourier-limited pulse, it was necessary to adjust the fourth-order dispersion setting on the chirped fiber Bragg grating. The differences between a non-fourth-order-compensated pulse and a compensated one are similar to the changes shown in [figure D.1](#). Specifically, both show the emergence of pre- and post-pulses in the form of side lobes in the FROG trace.

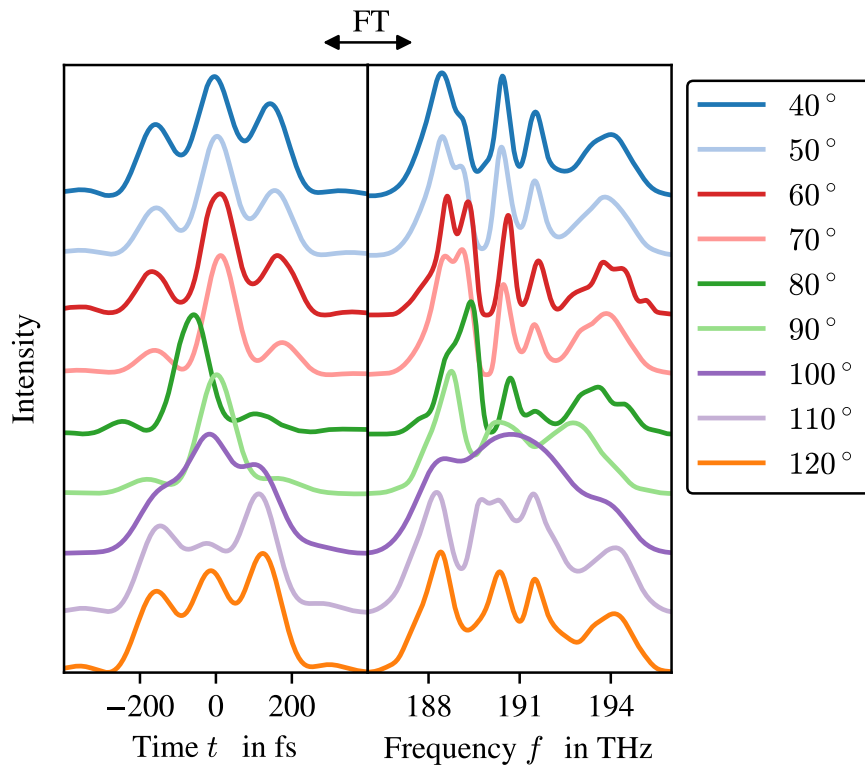


Figure D.1: **Temporal and spectral intensities for different half-waveplate angles.** The differences in the properties of the optical frequency comb are likely caused by self-phase modulation acting differently on the comb's polarization components. The data was measured at the end of the optical setup for different half-waveplate angles of the one found in the gray box of figure 3.1. Both temporal and spectral phase information are not shown. The range between 70° and 90° is considered near-Fourier-limited and was used for the experiments of chapter 4.

D.2 2D Rabi spectroscopy scan

Multiple measurements have been performed on the transition between the $3^2D_{5/2}$ ($m_{5/2} = -1/2$) and $3^2D_{3/2}$ ($m_{3/2} = -1/2$) states using the optical frequency comb and a comb-teeth number separation of $N = 7278$. One of them involved a 2-dimensional (2D) scan of the pulsetrain length t_{pulse} of the optical frequency comb and its repetition rate f_{rep} , in a similar fashion as shown in figure 4.2. This 2D map is shown in figure D.2 alongside two slices, showing a Rabi oscillation and a Rabi spectrum. The model for the map is given by 2.20. The measurement was performed to reproduce and compare to the result in [119, ch. 4.4.].

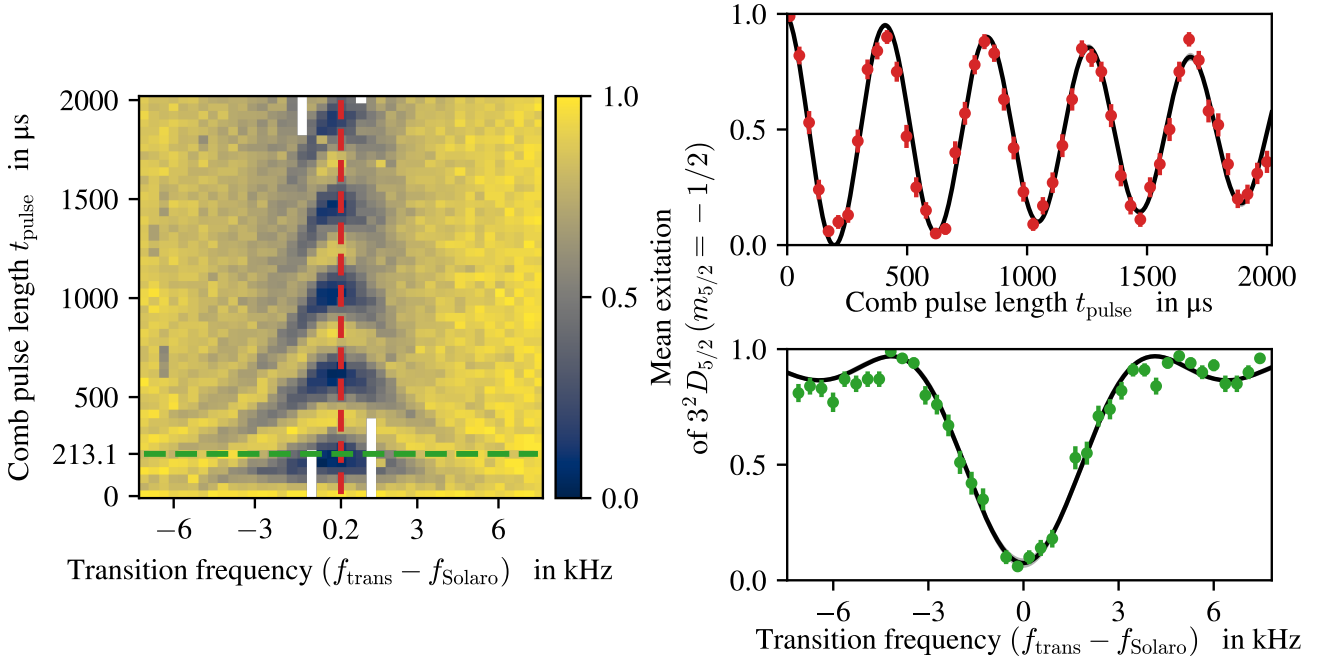


Figure D.2: **2D Rabi Raman map.** The 2D map was taken with a resolution of $40.61 \mu\text{s}$ in pulsetrain length and 0.05 Hz in repetition rate (translating to $7278 \cdot 0.05 \text{ Hz} = 0.3639 \text{ kHz}$ in transition frequency). The slices shown were taken at $t_{\text{pulse}} = 213.06 \mu\text{s}$ (green) and $f_{\text{trans}} = 0.18 \text{ kHz} + f_{\text{Solaro}}$ ($f_{\text{rep}} = 250.013'487'03 \text{ MHz}$, red). The data plotted here is AC-Stark shift and Zeeman shift-corrected using the measured $g_{3/2}$ value (equation (4.2)). The time taken for the measurement was on the order of eight hours.

D.3 Dispersion measurements

Dispersion is an important property in systems involving ultrafast lasers such as the optical frequency comb. As discussed in section 2.2.3, any dispersion can lead to a loss in efficiency in driving Raman transitions. To experimentally verify this effect, we used the chirped fiber Bragg grating (CFBG), used to stretch single pulse length in time before amplification, to change the dispersion parameters of the optical frequency comb. This is done by adjusting the CFBG set points thermally. For a set of group delay dispersion settings of the CFBG, we measured the Raman Rabi rate. The results are shown in red in figure D.3.

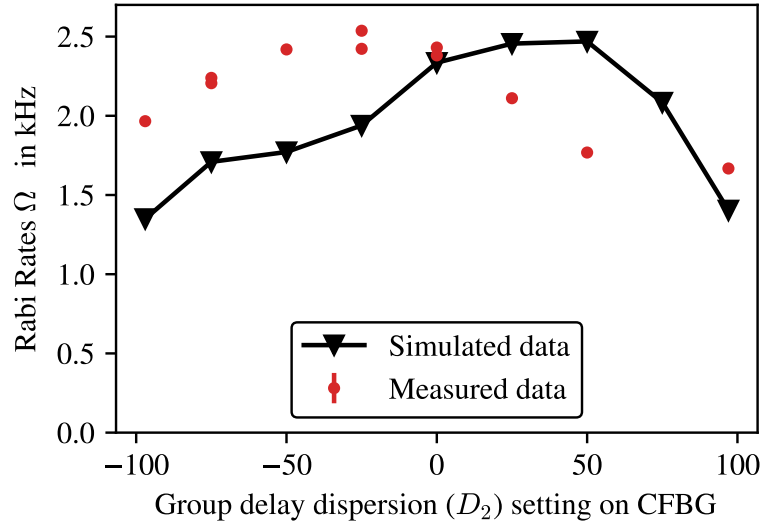


Figure D.3: **Efficiency drops due to dispersion.** The red data shows the measured Raman Rabi rates for different settings on the chirped fiber Bragg grating (CFBG). The black points take the full spectral information of the comb for each setting and use equation (2.4) to simulate an efficiency, where this result was scaled arbitrarily to units of Rabi rate. The discrepancy could arise from thermal drifts in the dispersion settings of the CFBG and the fact that the data for the red and black points were taken five months apart. The tunable range of the CFBG is $13.05 \pm 0.0584 \text{ ps}^2/\text{rad}$ (or $-9.95 \mp 0.0445 \text{ ps}/\text{nm}$), where the values on the x -axis translate to $-100 \hat{=} 12.9916 \text{ ps}^2/\text{rad}$ and $100 \hat{=} 13.1084 \text{ ps}^2/\text{rad}$. However, this transformation was not done on the x -axis, as it is misleading. Due to the HNLFF, these group delay dispersion values are not necessarily simply translated into the final spectrum.

There were multiple attempts to explain the data. The first attempt consisted of taking the efficiency η_{CW} (see equation (2.34)) for a given reference spectra (measured at the end of the optical path) and varying the group delay dispersion induced by the CFBG numerically according to equation (2.5). However, this procedure predicts incorrect results as the nonlinear effects of the highly nonlinear fiber (HNLFF) depend nontrivially on the input dispersion. As such, the dispersion after the HNLFF is not trivially related to the

D.3 Dispersion measurements

changes in the CFBG (in the sense of equation (2.5)).

The second attempt consisted of measuring the full spectral information of the optical frequency comb (after the optical setup) for each originally used CFBG setting. This data is then used for simulating the resulting efficiency η_{CW} . The comparison between the measured data and the simulated efficiencies can be seen in figure D.3. Note that the efficiencies have been scaled to the units of the Raman Rabi rate to match the maximum value of the data.

While the second approach takes the nonlinear effects in the HNLF into account, the two measurements (Raman Rabi rates and the full spectral information) were taken months apart. The dispersion coefficients of the CFBG are influenced by thermal drifts, especially when not directly controlled via software. Due to these drifts, the original settings used to measure the Raman Rabi rates were not reproducible when measuring the full spectral data for each CFBG software setting. These drifts influence all dispersion parameters: group delay dispersion, third-order dispersion, and fourth-order dispersion. To be able to explain the Raman Rabi rate data, we would have had to have measured the full spectral information of the comb directly after each Raman Rabi rate measurement.

Bibliography

- [1] N. S. H. Singh, and A. U. N. “An extensive review on quantum computers”. *Advances in Engineering Software* 174 (2022), p. 103337. ISSN: 0965-9978. DOI: [10.1016/j.advengsoft.2022.103337](https://doi.org/10.1016/j.advengsoft.2022.103337).
- [2] E. Chae, J. Choi, and J. Kim. “An elementary review on basic principles and developments of qubits for quantum computing”. *Nano Convergence* 11.1 (2024), p. 11. DOI: [10.1186/s40580-024-00418-5](https://doi.org/10.1186/s40580-024-00418-5).
- [3] M. Fellous-Asiani et al. “Limitations in Quantum Computing from Resource Constraints”. *PRX Quantum* 2 (4 Nov. 2021), p. 040335. DOI: [10.1103/PRXQuantum.2.040335](https://doi.org/10.1103/PRXQuantum.2.040335).
- [4] D. P. DiVincenzo. “The Physical Implementation of Quantum Computation”. *Fortschritte der Physik* 48.9-11 (2000), pp. 771–783. DOI: [10.1002/1521-3978\(200009\)48:9/11<771::AID-PROP771>3.0.CO;2-E](https://doi.org/10.1002/1521-3978(200009)48:9/11<771::AID-PROP771>3.0.CO;2-E).
- [5] P. Shor. “Algorithms for quantum computation: discrete logarithms and factoring”. *Proceedings 35th Annual Symposium on Foundations of Computer Science*. 1994, pp. 124–134. DOI: [10.1109/SFCS.1994.365700](https://doi.org/10.1109/SFCS.1994.365700).
- [6] P. W. Shor. “Polynomial-Time Algorithms for Prime Factorization and Discrete Logarithms on a Quantum Computer”. *SIAM Journal on Computing* 26.5 (1997), pp. 1484–1509. DOI: [10.1137/S0097539795293172](https://doi.org/10.1137/S0097539795293172).
- [7] L. K. Grover. “A fast quantum mechanical algorithm for database search”. *Proceedings of the Twenty-Eighth Annual ACM Symposium on Theory of Computing*. STOC '96. Philadelphia, Pennsylvania, USA: Association for Computing Machinery, 1996, pp. 212–219. ISBN: 0897917855. DOI: [10.1145/237814.237866](https://doi.org/10.1145/237814.237866).
- [8] M. A. Nielsen and I. L. Chuang. *Quantum computation and quantum information*. 10th Anniversary Edition. Cambridge university press, 2010.
- [9] C. D. Bruzewicz et al. “Trapped-ion quantum computing: Progress and challenges”. *Applied Physics Reviews* 6.2 (May 2019), p. 021314. ISSN: 1931-9401. DOI: [10.1063/1.5088164](https://doi.org/10.1063/1.5088164).
- [10] H.-L. Huang et al. “Superconducting quantum computing: a review”. *Science China Information Sciences* 63 (2020), pp. 1–32. DOI: [10.1007/s11432-020-2881-9](https://doi.org/10.1007/s11432-020-2881-9).
- [11] S. Pezzagna and J. Meijer. “Quantum computer based on color centers in diamond”. *Applied Physics Reviews* 8.1 (Feb. 2021), p. 011308. ISSN: 1931-9401. DOI: [10.1063/5.0007444](https://doi.org/10.1063/5.0007444).
- [12] S. Harvey. “Quantum dots/spin qubits”. *Oxford University Press* (2022). DOI: [10.1093/acrefore/9780190871994.013.83](https://doi.org/10.1093/acrefore/9780190871994.013.83).

Bibliography

- [13] S. Slussarenko and G. J. Pryde. “Photonic quantum information processing: A concise review”. *Applied Physics Reviews* 6.4 (Oct. 2019), p. 041303. ISSN: 1931-9401. DOI: [10.1063/1.5115814](https://doi.org/10.1063/1.5115814).
- [14] *AG Quantum Optics and Spectroscopy*. URL: <https://www.quantumoptics.at/en/>. (accessed on 14. February 2025).
- [15] I. Pogorelov et al. “Experimental fault-tolerant code switching”. *Nature Physics* (2025), pp. 1–6. DOI: [10.1038/s41567-024-02727-2](https://doi.org/10.1038/s41567-024-02727-2).
- [16] M. Ringbauer et al. “Verifiable measurement-based quantum random sampling with trapped ions”. *Nature Communications* 16.1 (2025), p. 106. DOI: [10.1038/s41467-024-55342-3](https://doi.org/10.1038/s41467-024-55342-3).
- [17] D. Kiesenhofer et al. “Controlling Two-Dimensional Coulomb Crystals of More Than 100 Ions in a Monolithic Radio-Frequency Trap”. *PRX Quantum* 4 (2 Apr. 2023), p. 020317. DOI: [10.1103/PRXQuantum.4.020317](https://doi.org/10.1103/PRXQuantum.4.020317).
- [18] V. Krutyanskiy et al. “Entanglement of Trapped-Ion Qubits Separated by 230 Meters”. *Phys. Rev. Lett.* 130 (5 Feb. 2023), p. 050803. DOI: [10.1103/PhysRevLett.130.050803](https://doi.org/10.1103/PhysRevLett.130.050803).
- [19] L. Nützel et al. “Solving an industrially relevant quantum chemistry problem on quantum hardware”. *Quantum Science and Technology* 10.1 (Jan. 2025), p. 015066. DOI: [10.1088/2058-9565/ad9ed3](https://doi.org/10.1088/2058-9565/ad9ed3).
- [20] M. K. Joshi et al. “Quantum Information Scrambling in a Trapped-Ion Quantum Simulator with Tunable Range Interactions”. *Phys. Rev. Lett.* 124 (24 June 2020), p. 240505. DOI: [10.1103/PhysRevLett.124.240505](https://doi.org/10.1103/PhysRevLett.124.240505).
- [21] M. K. Joshi et al. “Characterization of ion-trap-induced ac magnetic fields”. *Phys. Rev. A* 110 (6 Dec. 2024), p. 063101. DOI: [10.1103/PhysRevA.110.063101](https://doi.org/10.1103/PhysRevA.110.063101).
- [22] Y. Weiser et al. “Backaction suppression for levitated dipolar scatterers”. *Phys. Rev. A* 111 (1 Jan. 2025), p. 013503. DOI: [10.1103/PhysRevA.111.013503](https://doi.org/10.1103/PhysRevA.111.013503).
- [23] *QCosmo*. URL: <https://www.quantum-molecules.eu/>. (accessed on 14. February 2025).
- [24] P. Schindler. “Ultrafast infrared spectroscopy with single molecular ions”. *New Journal of Physics* 21.8 (Aug. 2019), p. 083025. DOI: [10.1088/1367-2630/ab3549](https://doi.org/10.1088/1367-2630/ab3549).
- [25] Z. Wu et al. “Photodissociation spectra of single trapped CaOH⁺ molecular ions”. *The Journal of Chemical Physics* 161.4 (July 2024), p. 044304. DOI: [10.1063/5.0217685](https://doi.org/10.1063/5.0217685).
- [26] B. J. Furey et al. “Strategies for implementing quantum error correction in molecular rotation”. *Quantum* 8 (2024), p. 1578. DOI: [10.22331/q-2024-12-27-1578](https://doi.org/10.22331/q-2024-12-27-1578).
- [27] W. Demtröder. *Atoms, molecules and photons*. First Edition. Springer, 2006.
- [28] M. Sinhal and S. Willitsch. “Molecular-Ion Quantum Technologies”. *Photonic Quantum Technologies*. John Wiley & Sons, Ltd, 2023. Chap. 13, pp. 305–332. ISBN: 9783527837427. DOI: <https://doi.org/10.1002/9783527837427.ch13>.

- [29] S. Burchesky et al. “Rotational Coherence Times of Polar Molecules in Optical Tweezers”. *Phys. Rev. Lett.* 127 (12 Sept. 2021), p. 123202. DOI: [10.1103/PhysRevLett.127.123202](https://doi.org/10.1103/PhysRevLett.127.123202).
- [30] J. W. Park et al. “Second-scale nuclear spin coherence time of ultracold ^{23}Na molecules”. *Science* 357.6349 (2017), pp. 372–375. DOI: [10.1126/science.aal5066](https://doi.org/10.1126/science.aal5066).
- [31] P. O. Schmidt et al. “Spectroscopy using quantum logic”. *Science* 309.5735 (2005), pp. 749–752. DOI: [10.1126/science.1114375](https://doi.org/10.1126/science.1114375).
- [32] P. O. Schmidt et al. “Spectroscopy of atomic and molecular ions using quantum logic”. *AIP Conference Proceedings* 862.1 (Oct. 2006), pp. 305–312. ISSN: 0094-243X. DOI: [10.1063/1.2387937](https://doi.org/10.1063/1.2387937).
- [33] C.-w. Chou et al. “Preparation and coherent manipulation of pure quantum states of a single molecular ion”. *Nature* 545.7653 (2017), pp. 203–207. DOI: [10.1038/nature22338](https://doi.org/10.1038/nature22338).
- [34] Y. Lin et al. “Quantum entanglement between an atom and a molecule”. *Nature* 581.7808 (2020), pp. 273–277. DOI: [10.1038/s41586-020-2257-1](https://doi.org/10.1038/s41586-020-2257-1).
- [35] C. M. Holland, Y. Lu, and L. W. Cheuk. “On-demand entanglement of molecules in a reconfigurable optical tweezer array”. *Science* 382.6675 (2023), pp. 1143–1147. DOI: [10.1126/science.adf4272](https://doi.org/10.1126/science.adf4272).
- [36] Y. Bao et al. “Dipolar spin-exchange and entanglement between molecules in an optical tweezer array”. *Science* 382.6675 (2023), pp. 1138–1143. DOI: [10.1126/science.adf8999](https://doi.org/10.1126/science.adf8999).
- [37] Y. Liu et al. “Quantum state tracking and control of a single molecular ion in a thermal environment”. *Science* 385.6710 (2024), pp. 790–795. DOI: [10.1126/science.ado1001](https://doi.org/10.1126/science.ado1001).
- [38] V. V. Albert, J. P. Covey, and J. Preskill. “Robust Encoding of a Qubit in a Molecule”. *Phys. Rev. X* 10 (3 Sept. 2020), p. 031050. DOI: [10.1103/PhysRevX.10.031050](https://doi.org/10.1103/PhysRevX.10.031050).
- [39] S. P. Jain et al. “Absorption-Emission Codes for Atomic and Molecular Quantum Information Platforms”. *Phys. Rev. Lett.* 133 (26 Dec. 2024), p. 260601. DOI: [10.1103/PhysRevLett.133.260601](https://doi.org/10.1103/PhysRevLett.133.260601). URL: <https://link.aps.org/doi/10.1103/PhysRevLett.133.260601>.
- [40] NIST. *Computational Chemistry Comparison and Benchmark Database, NIST Standard Reference Database Number 101, Release 22*. Ed. by R. D. J. III. accessed on 14. February 2025. May 2022. DOI: [10.18434/T47C7Z](https://doi.org/10.18434/T47C7Z). URL: <http://cccbdb.nist.gov/>.
- [41] C. H. Townes and A. L. Schawlow. *Microwave spectroscopy*. Courier Corporation, 2013.
- [42] S. Eibenberger, J. Doyle, and D. Patterson. “Enantiomer-Specific State Transfer of Chiral Molecules”. *Phys. Rev. Lett.* 118 (12 Mar. 2017), p. 123002. DOI: [10.1103/PhysRevLett.118.123002](https://doi.org/10.1103/PhysRevLett.118.123002).

Bibliography

- [43] I. D. Moore et al. “Photon scattering errors during stimulated Raman transitions in trapped-ion qubits”. *Phys. Rev. A* 107 (3 Mar. 2023), p. 032413. DOI: [10.1103/PhysRevA.107.032413](https://doi.org/10.1103/PhysRevA.107.032413).
- [44] C. Solaro et al. “Direct frequency-comb-driven Raman transitions in the terahertz range”. *Physical Review Letters* 120.25 (2018), p. 253601. DOI: [10.1103/PhysRevLett.120.253601](https://doi.org/10.1103/PhysRevLett.120.253601).
- [45] C.-w. Chou et al. “Frequency-comb spectroscopy on pure quantum states of a single molecular ion”. *Science* 367.6485 (2020), pp. 1458–1461. DOI: [10.1126/science.aba3628](https://doi.org/10.1126/science.aba3628).
- [46] *AQT: Pine Trap*. URL: <https://www.aqt.eu/products/pine-trap/>. (accessed on 07. February 2025).
- [47] M. Kajita. *Ion Traps: A gentle introduction*. IOP Publishing, 2022.
- [48] H. Shao et al. “Laser ablation and two-step photo-ionization for the generation of 40Ca^+ ”. *Journal of Physics Communications* 2.9 (Sept. 2018), p. 095019. DOI: [10.1088/2399-6528/aad16e](https://doi.org/10.1088/2399-6528/aad16e).
- [49] R. Lechner. “Photoionisation of 40Ca with a frequency-doubled 422 nm laser and a 377 nm laser diode”. Master’s Thesis. University of Innsbruck, 2010.
- [50] H. Sawamura, K. Toyoda, and S. Urabe. “Optimization of Doppler Cooling of a Single 40Ca^+ Ion”. *Japanese Journal of Applied Physics* 46.4R (Apr. 2007), p. 1713. DOI: [10.1143/JJAP.46.1713](https://doi.org/10.1143/JJAP.46.1713).
- [51] D. J. Wineland and W. M. Itano. “Laser cooling of atoms”. *Phys. Rev. A* 20 (4 Oct. 1979), pp. 1521–1540. DOI: [10.1103/PhysRevA.20.1521](https://doi.org/10.1103/PhysRevA.20.1521).
- [52] D. Leibfried et al. “Quantum dynamics of single trapped ions”. *Reviews of Modern Physics* 75.1 (2003), p. 281. DOI: [10.1103/RevModPhys.75.281](https://doi.org/10.1103/RevModPhys.75.281).
- [53] C. Roos et al. “Quantum State Engineering on an Optical Transition and Decoherence in a Paul Trap”. *Phys. Rev. Lett.* 83 (23 Dec. 1999), pp. 4713–4716. DOI: [10.1103/PhysRevLett.83.4713](https://doi.org/10.1103/PhysRevLett.83.4713).
- [54] R. Blatt and D. Wineland. “Entangled states of trapped atomic ions”. *Nature* 453.7198 (2008), pp. 1008–1015. DOI: [10.1038/nature07125](https://doi.org/10.1038/nature07125).
- [55] T. Fortier and E. Baumann. “20 years of developments in optical frequency comb technology and applications”. *Communications Physics* 2.1 (2019), p. 153. DOI: [10.1038/s42005-019-0249-y](https://doi.org/10.1038/s42005-019-0249-y).
- [56] S. T. Cundiff and J. Ye. “Colloquium: Femtosecond optical frequency combs”. *Reviews of Modern Physics* 75.1 (2003), p. 325. DOI: [10.1103/RevModPhys.75.325](https://doi.org/10.1103/RevModPhys.75.325).
- [57] J. Ye, H. Schnatz, and L. Hollberg. “Optical frequency combs: from frequency metrology to optical phase control”. *IEEE Journal of Selected Topics in Quantum Electronics* 9.4 (2003), pp. 1041–1058. DOI: [10.1109/JSTQE.2003.819109](https://doi.org/10.1109/JSTQE.2003.819109).
- [58] W. McGrew et al. “Atomic clock performance enabling geodesy below the centimetre level”. *Nature* 564.7734 (2018), pp. 87–90. DOI: [10.1038/s41586-018-0738-2](https://doi.org/10.1038/s41586-018-0738-2).

- [59] W. F. McGrew et al. “Towards the optical second: verifying optical clocks at the SI limit”. *Optica* 6.4 (2019), pp. 448–454. DOI: [10.1364/OPTICA.6.000448](https://doi.org/10.1364/OPTICA.6.000448).
- [60] P. Lazaridis, G. Debarge, and P. Gallion. “Time-bandwidth product of chirped sech 2 pulses: Application to phase-amplitude-coupling factor measurement”. *Optics letters* 20.10 (1995), pp. 1160–1162. DOI: [10.1364/OL.20.001160](https://doi.org/10.1364/OL.20.001160).
- [61] A. M. Weiner. *Ultrafast optics*. John Wiley & Sons, 2009.
- [62] B. E. Saleh and M. C. Teich. *Fundamentals of photonics*. John Wiley & Sons, 2019.
- [63] T. G. Mackay and A. Lakhtakia. *The transfer-matrix method in electromagnetics and optics*. First Edition. Springer Nature, 2020.
- [64] L. Grüner-Nielsen et al. “Dispersion Compensating Fibers”. *Optical Fiber Technology* 6.2 (2000), pp. 164–180. ISSN: 1068-5200. DOI: [10.1006/ofte.1999.0324](https://doi.org/10.1006/ofte.1999.0324).
- [65] D. Tosi. “Review of chirped fiber Bragg grating (CFBG) fiber-optic sensors and their applications”. *Sensors* 18.7 (2018), p. 2147. DOI: [10.3390/s18072147](https://doi.org/10.3390/s18072147).
- [66] L. B. Glebov et al. “Volume-chirped Bragg gratings: monolithic components for stretching and compression of ultrashort laser pulses”. *Optical Engineering* 53.5 (Feb. 6, 2014), pp. 051514–051514. DOI: [10.1117/1.oe.53.5.051514](https://doi.org/10.1117/1.oe.53.5.051514).
- [67] *PI USA: Optical Delay Line Stages: How Do They Work?* URL: <https://www.pi-usa.us/en/tech-blog/optical-delay-line-stages-how-do-they-work>. (accessed on 06. February 2025).
- [68] O. Schubert et al. “Rapid-scan acousto-optical delay line with 34 kHz scan rate and 15 as precision”. *Opt. Lett.* 38.15 (Aug. 2013), pp. 2907–2910. DOI: [10.1364/OL.38.002907](https://doi.org/10.1364/OL.38.002907).
- [69] D. Strickland and G. Mourou. “Compression of amplified chirped optical pulses”. *Optics communications* 55.6 (1985), pp. 447–449. DOI: [10.1016/0030-4018\(85\)90120-8](https://doi.org/10.1016/0030-4018(85)90120-8).
- [70] R. H. Stolen and C. Lin. “Self-phase-modulation in silica optical fibers”. *Physical Review A* 17.4 (1978), p. 1448. DOI: [10.1103/PhysRevA.17.1448](https://doi.org/10.1103/PhysRevA.17.1448).
- [71] G. P. Agrawal. *Nonlinear Fiber Optics*. Third Edition. Academic Press, 2001.
- [72] A. Demircan et al. “Supercontinuum generation by multiple scatterings at a group velocity horizon”. *Optics Express* 22.4 (2014), pp. 3866–3879. DOI: [10.1364/OE.22.003866](https://doi.org/10.1364/OE.22.003866).
- [73] J. O. Smith. *Mathematics of the Discrete Fourier Transform (DFT): With Audio Applications*. Second. W3K Publishing. BookSurge, 2008. ISBN: 9780974560748. URL: <https://ccrma.stanford.edu/~jos/mdft/>.
- [74] O. Melchert and A. Demircan. “py-fmas: A python package for ultrashort optical pulse propagation in terms of forward models for the analytic signal”. *Computer Physics Communications* 273 (2022), p. 108257. DOI: [10.1016/j.cpc.2021.108257](https://doi.org/10.1016/j.cpc.2021.108257).

Bibliography

- [75] C. Finot, F. Chaussard, and S. Boscolo. “Simple guidelines to predict self-phase modulation patterns”. *JOSA B* 35.12 (2018), pp. 3143–3152. DOI: [10.1364/JOSAB.35.003143](https://doi.org/10.1364/JOSAB.35.003143).
- [76] J. K. Ranka, R. S. Windeler, and A. J. Stentz. “Visible continuum generation in air–silica microstructure optical fibers with anomalous dispersion at 800 nm”. *Optics letters* 25.1 (2000), pp. 25–27. DOI: [10.1364/OL.25.000025](https://doi.org/10.1364/OL.25.000025).
- [77] G.-C. Hsieh and J. Hung. “Phase-locked loop techniques. A survey”. *IEEE Transactions on Industrial Electronics* 43.6 (1996), pp. 609–615. DOI: [10.1109/41.544547](https://doi.org/10.1109/41.544547).
- [78] D. J. Jones et al. “Carrier-envelope phase control of femtosecond mode-locked lasers and direct optical frequency synthesis”. *Science* 288.5466 (2000), pp. 635–639. DOI: [10.1126/science.288.5466.635](https://doi.org/10.1126/science.288.5466.635).
- [79] R. Holzwarth et al. “Optical frequency synthesizer for precision spectroscopy”. *Physical review letters* 85.11 (2000), p. 2264. DOI: [10.1103/PhysRevLett.85.2264](https://doi.org/10.1103/PhysRevLett.85.2264).
- [80] T. Udem, R. Holzwarth, and T. W. Hänsch. “Optical frequency metrology”. *Nature* 416.6877 (2002), pp. 233–237. DOI: [10.1038/416233a](https://doi.org/10.1038/416233a).
- [81] M. Niering et al. “Measurement of the hydrogen 1 s-2 s transition frequency by phase coherent comparison with a microwave cesium fountain clock”. *Physical Review Letters* 84.24 (2000), p. 5496. DOI: [10.1103/PhysRevLett.84.5496](https://doi.org/10.1103/PhysRevLett.84.5496).
- [82] I. Coddington, N. Newbury, and W. Swann. “Dual-comb spectroscopy”. *Optica* 3.4 (2016), pp. 414–426. DOI: [10.1364/OPTICA.3.000414](https://doi.org/10.1364/OPTICA.3.000414).
- [83] N. Picqué and T. W. Hänsch. “Frequency comb spectroscopy”. *Nature Photonics* 13.3 (2019), pp. 146–157. DOI: [10.1038/s41566-018-0347-5](https://doi.org/10.1038/s41566-018-0347-5).
- [84] P. Staantum. “Quantum Optics with Trapped Calcium Ions”. Doctoral Dissertation. University of Aarhus, 2004.
- [85] *HyperPhysics: Term Symbols*. URL: <http://hyperphysics.phy-astr.gsu.edu/hbase/Atomic/Term.html#c1>. (accessed on 07. February 2025).
- [86] *HyperPhysics: Spectroscopic Notation*. URL: <http://hyperphysics.phy-astr.gsu.edu/hbase/quantum/hydcol.html#c3>. (accessed on 07. February 2025).
- [87] D. J. Griffiths and D. F. Schroeter. *Introduction to quantum mechanics*. Third Edition. Cambridge university press, 2018.
- [88] M. Guevara Bertsch. “Optical clocks with trapped ions”. Doctoral Dissertation. University of Innsbruck, 2023.
- [89] M. O. Scully and M. S. Zubairy. *Quantum optics*. First Edition. Cambridge university press, 1997.
- [90] D. Zeuch et al. “Exact rotating wave approximation”. *Annals of Physics* 423 (2020), p. 168327. ISSN: 0003-4916. DOI: <https://doi.org/10.1016/j.aop.2020.168327>.

- [91] D. James and J. Jerke. “Effective Hamiltonian theory and its applications in quantum information”. *Canadian Journal of Physics* 85.6 (2007), pp. 625–632. DOI: [10.1139/P07-060](https://doi.org/10.1139/P07-060).
- [92] J. Kořata et al. “Fixing the rotating-wave approximation for strongly detuned quantum oscillators”. *Phys. Rev. Res.* 4 (3 Sept. 2022), p. 033177. DOI: [10.1103/PhysRevResearch.4.033177](https://doi.org/10.1103/PhysRevResearch.4.033177).
- [93] N. F. Ramsey. “A Molecular Beam Resonance Method with Separated Oscillating Fields”. *Phys. Rev.* 78 (6 June 1950), pp. 695–699. DOI: [10.1103/PhysRev.78.695](https://doi.org/10.1103/PhysRev.78.695).
- [94] D. Hu et al. “Ramsey interferometry with trapped motional quantum states”. *Communications Physics* 1.1 (2018), p. 29. DOI: [10.1038/s42005-018-0030-7](https://doi.org/10.1038/s42005-018-0030-7).
- [95] E. L. Hahn. “Spin Echoes”. *Phys. Rev.* 80 (4 Nov. 1950), pp. 580–594. DOI: [10.1103/PhysRev.80.580](https://doi.org/10.1103/PhysRev.80.580).
- [96] M. J. Biercuk, A. C. Doherty, and H. Uys. “Dynamical decoupling sequence construction as a filter-design problem”. *Journal of Physics B: Atomic, Molecular and Optical Physics* 44.15 (July 2011), p. 154002. DOI: [10.1088/0953-4075/44/15/154002](https://doi.org/10.1088/0953-4075/44/15/154002).
- [97] S. Kwak and J. Kim. “Central limit theorem: The cornerstone of modern statistics”. *Korean Journal of Anesthesiology* 70 (Apr. 2017), p. 144. DOI: [10.4097/kjae.2017.70.2.144](https://doi.org/10.4097/kjae.2017.70.2.144).
- [98] T. M. Bisgaard and Z. Sasvári. *Characteristic functions and moment sequences: positive definiteness in probability*. Nova Publishers, 2000.
- [99] D. Brand, I. Sinayskiy, and F. Petruccione. “Markovian noise modelling and parameter extraction framework for quantum devices”. *Scientific Reports* 14.1 (2024), p. 4769. DOI: [10.1038/s41598-024-54598-5](https://doi.org/10.1038/s41598-024-54598-5).
- [100] T. Nakajima et al. “Coherence of a Driven Electron Spin Qubit Actively Decoupled from Quasistatic Noise”. *Phys. Rev. X* 10 (1 Mar. 2020), p. 011060. DOI: [10.1103/PhysRevX.10.011060](https://doi.org/10.1103/PhysRevX.10.011060).
- [101] G. A. Paz-Silva and L. Viola. “General Transfer-Function Approach to Noise Filtering in Open-Loop Quantum Control”. *Phys. Rev. Lett.* 113 (25 Dec. 2014), p. 250501. DOI: [10.1103/PhysRevLett.113.250501](https://doi.org/10.1103/PhysRevLett.113.250501).
- [102] A. Vezvae et al. “Fourier transform noise spectroscopy”. *npj Quantum Information* 10.1 (2024), p. 52. DOI: [10.1038/s41534-024-00841-w](https://doi.org/10.1038/s41534-024-00841-w).
- [103] N. Sadzak et al. “A Hahn-Ramsey scheme for dynamical decoupling of single solid-state qubits”. *Frontiers in Photonics* 3 (2022). ISSN: 2673-6853. DOI: [10.3389/fphot.2022.932944](https://doi.org/10.3389/fphot.2022.932944).
- [104] J. S. W. Campbell and G. Bruce Pike. “Diffusion Magnetic Resonance Imaging”. *Encyclopedia of Biomedical Engineering*. Ed. by R. Narayan. Oxford: Elsevier, 2019, pp. 505–518. ISBN: 978-0-12-805144-3. DOI: [10.1016/B978-0-12-801238-3.64102-8](https://doi.org/10.1016/B978-0-12-801238-3.64102-8).

Bibliography

- [105] H. M. Sevian and J. L. Skinner. “T2 can be greater than 2T1”. *The Journal of Chemical Physics* 91.3 (Aug. 1989), pp. 1775–1782. ISSN: 0021-9606. DOI: [10.1063/1.457648](https://doi.org/10.1063/1.457648).
- [106] *Menlo Systems GmbH*. URL: <https://www.menlosystems.com/>. (accessed on 14. December 2024).
- [107] D. Heinrich et al. “Ultrafast coherent excitation of a $^{40}\text{Ca}^+$ ion”. *New Journal of Physics* 21.7 (July 2019), p. 073017. DOI: [10.1088/1367-2630/ab2a7e](https://doi.org/10.1088/1367-2630/ab2a7e).
- [108] M. Guggemos et al. “Frequency measurement of the $^1\text{S}_0, F = 5/2 \leftrightarrow ^3\text{P}_1, F = 7/2$ transition of $^{27}\text{Al}^+$ via quantum logic spectroscopy with $^{40}\text{Ca}^+$ ”. *New Journal of Physics* 21.10 (Oct. 2019), p. 103003. DOI: [10.1088/1367-2630/ab447a](https://doi.org/10.1088/1367-2630/ab447a).
- [109] M. Hussain et al. “Ultraviolet Laser Pulses with Multigigahertz Repetition Rate and Multiwatt Average Power for Fast Trapped-Ion Entanglement Operations”. *Phys. Rev. Appl.* 15 (2 Feb. 2021), p. 024054. DOI: [10.1103/PhysRevApplied.15.024054](https://doi.org/10.1103/PhysRevApplied.15.024054).
- [110] D. Heinrich. “Ultra fast coherent excitation of a $^{40}\text{Ca}^+$ ion”. Doctoral Dissertation. University of Innsbruck, 2019.
- [111] *FC1500 Optical Frequency Synthesizer: User Manual (AU00707)*. Version 1.6.3. Menlo Systems GmbH. Munich, Oct. 2010.
- [112] A. Naji et al. “Review of Erbium-doped fiber amplifier”. *International Journal of the Physical Sciences* 6.20 (2011), pp. 4674–4689.
- [113] G. W. Faris, M. J. Dyer, and W. K. Bischel. “Laser linewidth narrowing induced by amplifier gain saturation”. *Opt. Lett.* 19.19 (Oct. 1994), pp. 1529–1531. DOI: [10.1364/OL.19.001529](https://doi.org/10.1364/OL.19.001529).
- [114] D. J. Kane and R. Trebino. “Single-shot measurement of the intensity and phase of an arbitrary ultrashort pulse by using frequency-resolved optical gating”. *Optics letters* 18.10 (1993), pp. 823–825. DOI: [10.1364/OL.18.000823](https://doi.org/10.1364/OL.18.000823).
- [115] J.-C. Diels and W. Rudolph. *Ultrashort laser pulse phenomena*. Second Edition. Elsevier, 2006.
- [116] *AQT*. URL: <https://www.aqt.eu/>. (accessed on 14. December 2024).
- [117] W. M. Itano et al. “Quantum projection noise: Population fluctuations in two-level systems”. *Phys. Rev. A* 47 (5 May 1993), pp. 3554–3570. DOI: [10.1103/PhysRevA.47.3554](https://doi.org/10.1103/PhysRevA.47.3554).
- [118] H. Katori. “Optical lattice clocks and quantum metrology”. *Nature Photonics* 5.4 (2011), pp. 203–210. DOI: [10.1038/nphoton.2011.45](https://doi.org/10.1038/nphoton.2011.45).
- [119] C. Hempel. “Digital quantum simulation, Schrödinger cat state spectroscopy and setting up a linear ion trap”. Doctoral Dissertation. University of Innsbruck, 2014.
- [120] K. Matsubara et al. “Absolute frequency measurement of the $^{40}\text{Ca}^+$ clock transition using a LD-based clock laser and UTC(NICT)”. *2009 IEEE International Frequency Control Symposium Joint with the 22nd European Frequency and Time forum*. 2009, pp. 751–755. DOI: [10.1109/FREQ.2009.5168285](https://doi.org/10.1109/FREQ.2009.5168285).

- [121] M. Chwalla et al. “Precision spectroscopy with two correlated atoms”. *Applied Physics B* 89 (2007), pp. 483–488. DOI: [10.1007/s00340-007-2867-4](https://doi.org/10.1007/s00340-007-2867-4).
- [122] I. Hughes and T. Hase. *Measurements and their uncertainties: a practical guide to modern error analysis*. OUP Oxford, 2010.
- [123] N. Huntemann et al. “Single-Ion Atomic Clock with 3×10^{-18} Systematic Uncertainty”. *Phys. Rev. Lett.* 116 (6 Feb. 2016), p. 063001. DOI: [10.1103/PhysRevLett.116.063001](https://doi.org/10.1103/PhysRevLett.116.063001).
- [124] M. Chwalla et al. “Absolute Frequency Measurement of the $^{40}\text{Ca}^+ 4s \ ^2S_{1/2} - 3d \ ^2D_{5/2}$ Clock Transition”. *Phys. Rev. Lett.* 102 (2 Jan. 2009), p. 023002. DOI: [10.1103/PhysRevLett.102.023002](https://doi.org/10.1103/PhysRevLett.102.023002).
- [125] S. N. Miao et al. “Second-order Doppler frequency shifts of trapped ions in a linear Paul trap”. *Phys. Rev. A* 106 (3 Sept. 2022), p. 033121. DOI: [10.1103/PhysRevA.106.033121](https://doi.org/10.1103/PhysRevA.106.033121).
- [126] M. S. Safronova, M. G. Kozlov, and C. W. Clark. “Blackbody radiation shifts in optical atomic clocks”. *IEEE Transactions on Ultrasonics, Ferroelectrics, and Frequency Control* 59.3 (2012), pp. 439–447. DOI: [10.1109/TUFFC.2012.2213](https://doi.org/10.1109/TUFFC.2012.2213).
- [127] H. Cheng et al. “Uncertainty evaluation of the second-order Zeeman shift of a transportable 87Rb atomic fountain clock”. *Chinese Optics Letters* 19.11 (Dec. 2021), p. 120201. DOI: [10.3788/COL202119.120201](https://doi.org/10.3788/COL202119.120201).
- [128] X. Wang et al. “The study of second-order Zeeman shift of the cesium fountain clock NTSC-F1”. *2016 IEEE International Frequency Control Symposium (IFCS)*. 2016, pp. 1–3. DOI: [10.1109/FCS.2016.7546817](https://doi.org/10.1109/FCS.2016.7546817).
- [129] N. B. Delone and V. P. Krainov. “AC Stark shift of atomic energy levels”. *Physics-Uspekhi* 42.7 (1999), p. 669. DOI: [10.1070/PU1999v042n07ABEH000557](https://doi.org/10.1070/PU1999v042n07ABEH000557).
- [130] D. Vion et al. “Manipulating the Quantum State of an Electrical Circuit”. *Science* 296.5569 (2002), pp. 886–889. DOI: [10.1126/science.1069372](https://doi.org/10.1126/science.1069372).
- [131] D. Wineland et al. “Experimental Issues in Coherent Quantum-State Manipulation of Trapped Atomic Ions”. *Journal of Research of the National Institute of Standards and Technology* 103 (Nov. 1997). DOI: [10.6028/jres.103.019](https://doi.org/10.6028/jres.103.019).
- [132] J. Santhanam and G. P. Agrawal. “Raman-induced spectral shifts in optical fibers: general theory based on the moment method”. *Optics Communications* 222.1-6 (2003), pp. 413–420. DOI: [10.1016/S0030-4018\(03\)01561-X](https://doi.org/10.1016/S0030-4018(03)01561-X).
- [133] J. H. Lee et al. “Soliton self-frequency shift: experimental demonstrations and applications”. *IEEE Journal of Selected Topics in Quantum Electronics* 14.3 (2008), pp. 713–723. DOI: [10.1109/JSTQE.2008.915526](https://doi.org/10.1109/JSTQE.2008.915526).
- [134] W. R. Rowe, D. V. Skryabin, and A. V. Gorbach. “Raman solitons in waveguides with simultaneous quadratic and Kerr nonlinearities”. *Physical Review A* 102.2 (2020), p. 023523. DOI: [10.1103/PhysRevA.102.023523](https://doi.org/10.1103/PhysRevA.102.023523).
- [135] M. Karpov et al. “Raman self-frequency shift of dissipative Kerr solitons in an optical microresonator”. *Physical review letters* 116.10 (2016), p. 103902. DOI: [10.1103/PhysRevLett.116.103902](https://doi.org/10.1103/PhysRevLett.116.103902).

Bibliography

- [136] T. A. Johnson and S. A. Diddams. “Mid-IR frequency comb upconversion spectroscopy”. *Conference on Lasers and Electro-Optics 2010*. Optica Publishing Group, 2010, CPDB11. DOI: [10.1364/CLEO.2010.CPDB11](https://doi.org/10.1364/CLEO.2010.CPDB11).
- [137] *NIST: Ion Storage Group*. URL: <https://www.nist.gov/pml/time-and-frequency-division/ion-storage>. (accessed on 07. February 2025).
- [138] D. Hayes et al. “Entanglement of atomic qubits using an optical frequency comb”. *Physical review letters* 104.14 (2010), p. 140501. DOI: [10.1103/PhysRevLett.104.140501](https://doi.org/10.1103/PhysRevLett.104.140501).